André Filipe Simões Ferreira

INSIGHTS INTO GOLD NANOPARTICLES FUNCTIONALIZED WITH CYSTEINE-TERMINATED CECROPIN MELITTIN AND CATHELICIDIN-DERIVED ANTIMICROBIAL PEPTIDES - A COMPUTATIONAL APPROACH

UNIVERSIDADE DE COIMBRA

UNIVERSIDADE DE
COIMBRA

André Filipe Simões Ferreira

INSIGHTS INTO GOLD NANOPARTICLES FUNCTIONALIZED WITH CYSTEINE-TERMINATED CECROPIN MELITTIN AND CATHELICIDIN-DERIVED ANTIMICROBIAL PEPTIDES - A COMPUTATIONAL APPROACH

Tese no âmbito do Doutoramento em Engenharia Química orientada pelo Professor Doutor Pedro Nuno das Neves Lopes Simões e apresentada à Faculdade de Ciências e Tecnologia.

Agosto de 2018

Faculdade de Ciências e Tecnologia

Insights into gold nanoparticles functionalized with cysteine-terminated cecropin melittin and cathelicidin-derived antimicrobial peptides - a computational approach

André Filipe Simões Ferreira

Tese no âmbito do Doutoramento em Engenharia Química orientada pelo Professor
Doutor Pedro Nuno das Neves Lopes Simões e apresentada à Universidade de Coimbra.

Agosto de 2018

Acknowledgements

Ao meu orientador científico, Professor Doutor Pedro Nuno Simões, por ter embarcado comigo neste desafio. Obrigado pela disponibilidade inabalável, pela confiança, pelo espírito crítico que sempre me incutiu e por todo o conhecimento que me transmitiu. Esta colaboração foi preponderante para meu desenvolvimento pessoal, não apenas pela vertente científica.

Aos colegas do CNC/Biocant, Doutor Lino Ferreira, Doutor Akhilesh Rai e Doutora Michela Comune. Obrigado pelo desafio que nos lançaram, pelo conhecimento científico partilhado e pela disponibilidade para o esclarecimento de dúvidas.

Ao grupo de Computação, Estatística e Materiais (CEM) do Departamento de Engenharia Química de Coimbra. Obrigado por me ter providenciado todas as, excelentes, condições para execução deste plano doutoral.

Ao Professor Doutor Nuno Oliveira e Doutor Adamo Caetano. Obrigado por toda disponibilidade demonstrada durante a configuração e manutenção dos *clusters* de cálculo.

Aos meus amigos. Obrigado pela incansável boa disposição e força que me deram nos momentos mais difíceis.

À minha família. Obrigado a todos pelos momentos que proporcionaram, pelo convívio, por todo o apoio e por me terem ajudado a tornar naquilo que sou hoje.

Aos meus pais. Obrigado por sempre me terem dado as ferramentas necessárias para seguir o meu caminho e por sempre me terem ajudado. Todos os meus sucessos têm o vosso cunho!

À Inês. Obrigado pela companhia, suporte, alegria, energia e força que me deste durante toda esta caminhada. Apesar de todos desafios que enfrentámos, tive sempre o teu apoio incondicional. Não teria aqui chegado sem a tua ajuda. Obrigado!

Abstract

Despite the remarkable development of antimicrobial drugs during the past decades, infectious diseases remain the second-leading cause of death worldwide. Antimicrobial peptides (AMPs) are a class of antimicrobials that are known to hinder the antimicrobial resistance and are very effective against several strains of bacteria, fungi and viruses. However, these materials lack bloodstream stability and targeting capabilities, which has motivated the search for nanomaterials to be used as carriers. The immobilization of gold nanoparticles (AuNPs) with AMPs appeared as a new and promising way to enhance both activity and targeting capabilities of AMPs. Nonetheless, the investigation of these systems on how they function at the nanoscale is scarcely reported. In this context, Molecular modelling and simulation tools are crucial to address issues which are extremely difficult, or even impossible, to be addressed experimentally.

This work aimed at gaining new insights into gold nanoparticles functionalized with two types of cysteine-terminated antimicrobial peptides – a cecropin melittin hybrid and a cathelicidin-derived peptide – from a computational approach. In line with this objective a molecular dynamics based study was carried out to probe the targeted systems at nanoscale in three vectors: i) adsorption capability of the AMPs onto gold surfaces; ii) free-energy characterization of the AMP/AuNP conjugate interaction using an advanced sampling method; iii) assessment of the interaction of a AMP/AuNP conjugate with a biomembrane mimetic model.

The obtained results show that the way the peptides approach the surface dictates the final conformation and the time required to achieve it. The AMP diffusion process is affected by the attraction field projected by the gold surface into the solvent, resembling a exponential decay. It was possible to identify a high affinity between the AMPs and the gold surface, characterized by the direct contact between the α-carbon protons and the surface. Furthermore, it is demonstrated that cysteine (CYS) promotes a faster conformational stabilization during the lockdown regime of the CYS-terminated AMPs, noticeably affecting this by acting as a preferential anchoring point.

The structural analysis combined with the free energy surface (FES) characterization allowed to assess the role of CYS residue during the formation of the conjugate, and, more significantly, has helped to understand how the AuNP contributes to improve the antimicrobial activity of the peptide. It was found that CYS promotes a lower conformational entropy (before and after adsorption onto the AuNP) and a faster adsorption process when compared to the AMP without CYS. The presence of the AuNP fosters the elongation of the peptides along with the adsorption, which translates into the increase of the solvent accessible surface area. This elongation, combined with the greater availability of positively charged residues upon adsorption, provide a rationale for the enhancement of the activity of AMP/AuNP conjugates.

The simulation of the interaction between the cathelicidin-derived peptide conjugate and the lipid bilayer model allowed to unveil the effect of each component on the bilayer characteristics. The bare AuNP causes a severe deformation in the bilayer leaflets, motivated by the displacement of the lipid molecules. The fact that the lipids are adsorbing to the AuNP by displacing the water on its surface suggests an adsorption mechanism similar to that for AMPs. Oppositely, the conjugate tends to migrate to the bilayer surface without penetrating in it, thus causing minor disturbances in the bilayer properties. The AuNP corona formed by the AMP shields the AuNP from lipids, precluding its permeation in the bilayer. Similarly to the conjugate, the free AMPs consistently migrate to the bilayer surface. The AMP residues with hydrophobic side-chains eventually orient themselves to the bilayer center, hampering its release to the solvent.

It is believed that the wealth of data provided by this work contributes to a better understanding of the conjugate formation of cecropin melittin and cathelicidin-derived AMPs with AuNPs, and constitutes a solid starting point for more in-depth studies on the mechanisms that govern the interactions of these conjugates with cell membranes.

Resumo

Apesar do extraordinário desenvolvimento dos medicamentos antimicrobianos, as doenças infecciosas continuam a ser a segunda maior causa de mortalidade a nível mundial. Os péptidos antimicrobianos (PAM) são uma classe de agentes antimicrobianos aptos a fazer face à resistência antimicrobiana, com actividade contra diferentes estirpes de bactérias, fungos e vírus. Contudo, possuem baixa estabilidade na corrente sanguínea e fraca capacidade de visar o agente patógeno pretendido. Estas limitações levaram à pesquisa e desenvolvimento de materiais nanoestruturados para serem utilizados como suporte, e, neste âmbito, a conjugação de nanopartículas de ouro (AuNP) com PAM emergiu como uma estratégia promissora no sentido de melhorar a actividade e o efeito dirigido sobre os patógenos. A investigação experimental deste tipo de sistemas à nanoescala é escassa, difícil, ou mesmo inexequível, pelo que o recurso a ferramentas de modelação e simulação computacional revela-se determinante no estudo fundamental de fenómenos cujo acesso por via exclusivamente empírica é uma impossibilidade.

Este trabalho teve por finalidade resolver, mediante uma abordagem computacional, pormenores fundamentais sobre sistemas baseados em nanopartículas funcionalizadas com péptidos antimicrobianos (híbrido de cecropina e melitina e um derivado da catelicidina). Para o efeito, recorreu-se a ferramentas de dinâmica molecular para explorar os sistemas objecto de estudo em três vertentes: i) capacidade de adsorção dos PAM em superfícies de ouro; ii) caracterização da superfície de energia livre da formação do conjugado PAM/AuNP recorrendo a métodos de dinâmica molecular convencionais e avançados; iii) avaliação da interação do conjugado do derivado da catelicidina com um modelo de biomembrana.

Os resultados obtidos indicam que a orientação do péptido na sua aproximação à superfície dita a sua conformação final, bem como o tempo necessário para a atingir. O processo de difusão dos PAM é afectado pelo campo de atracção projectado pela AuNP no solvente, resultando em um perfil semelhante a um decaimento exponencial. Os PAM e a superfície revelam grande afinidade, caracterizada pelo contacto directo entre os protões dos carbonos-α e a superfície. Adicionalmente, foi demonstrado que a presença da cisteína (CYS) acelera a estabilização do PAM durante o regime de ajuste à superfície, sendo que este resíduo actua como um ponto ancoragem no ouro.

A análise estrutural e a caracterização da superfície de energia livre permitiram, por um lado, avaliar o efeito da cisteína durante o processo de formação do conjugado, e, por outro, não menos importante, ajudar a perceber como é que a AuNP afecta a actividade dos PAM. Verifica-se que a CYS promove uma entropia conformacional inferior (antes e depois da adsorção) e parece catalisar o processo de adsorção. A presença da AuNP no sistema leva a que os PAM se apresentem preferencialmente alongados após a adsorção, o que se traduz numa aŕea de acesso de solvente superior. Este elongamento e o facto de os PAM terem os resíduos com carga positiva mais disponíveis ajudam a explicar o aumento de actividade dos conjugados.

A simulação da interacção do conjugado do derivado da catelicidina com o modelo de biomembrana permitiu avaliar o efeito de cada componente nas características dessa bicamada lipídica. Os resultados mostram que a AuNP sem PAM provoca severas deformações na superfície da biomembrana, promovida por uma forte interacção com os lípidos constituintes. O facto de os lípidos aderirem à superfície da AuNP por deslocalização das moléculas de água na sua uperfície sugere que o mecanismo de adsorção é similar ao dos PAM na AuNP. Contrariamente, e apesar de migrar para a superfície, o conjugado não provoca deformações na biomembrana. De facto, o revestimento de PAM do conjugado actua como um agente protector da AuNP, não permitindo a sua permeação. De forma semelhante, os PAM livres migram consistentemente para a superfície da biomembrana, tendendo a manter-se nessa condição. Esta comportamento com a biomembrana é motivado pela orientação dos resíduos hidrofóbicos para o interior da membrana, actuando como uma âncora.

Em suma, confia-se que o conjunto de dados originais reunidos neste trabalho é uma contribuição importante para melhor compreender, de um ponto de vista fundamental, a formação e as características essenciais de conjugados de cecropia e do derivado de catelicidina com AuNP, e constitui um ponto de partida relevante na avaliação detalhada dos mecanismos prevalecentes na sua interacção com membranas celulares.

List of Publications

- **Computational modelling contribution on experimental comprehensiveness studies**

– A. Rai, S. Pinto, T. R. Velho, A. F. Ferreira, C. Moita, U. Trivedi, M. Evangelista, M. Comune, K. P. Rumbaugh, P. N. Simões, L. Moita, and L. Ferreira, "One-step synthesis of high-density peptide-conjugated gold nanoparticles with antimicrobial efficacy in a systemic infection model," *Biomaterials*, vol. 85, pp. 99–110, apr 2016

– M. Comune, A. Rai, K. K. Chereddy, S. Pinto, S. Aday, A. F. Ferreira, A. Zonari, J. Blersch, R. Cunha, R. Rodrigues, J. Lerma, P. N. Simões, V. Préat, and L. Ferreira, "Antimicrobial peptide-gold nanoscale therapeutic formulation with high skin regenerative potential," *J. Control. Release*, vol. 262, pp. 58–71, sep 2017

- **Molecular modelling and simulation based studies**

– A. F. Ferreira, A. Rai, L. Ferreira, and P. N. Simões, "Findings on the interaction of the antimicrobial peptide cecropin-melittin with a gold surface from molecular dynamics studies," *Eur. Biophys. J.*, vol. 46, pp. 247–256, apr 2017

– A. F. Ferreira, M. Comune, A. Rai, L. Ferreira, and P. N. Simões, "Atomistic-Level Investigation of a LL37 Conjugated Gold Nanoparticle by Well-Tempered Metadynamics," *J. Phys. Chem. B*, p. acs.jpcb.8b05717, aug 2018

– A. F. Ferreira, M. Comune, A. Rai, L. Ferreira, and P. N. Simões, "Computational study of the interaction of a LL37 Conjugated Gold Nanoparticle with a keratinocyte analogous bilayer". In preparation.

Contents

List of Tables

List of Figures

Abbreviations

AgNP	Silver nanoparticle
AuNP	Gold nanoparticle
AIMD	*Ab initio* molecular dynamics
AMP	Antimicrobial peptide
ATB	Automated topology builder
AuNP	Gold nanoparticle
CEM	Computação, Estatística e Materiais
CIEPQPF	Centro de Investigação em Engenharia dos Processos Químicos e dos Produtos da Floresta
CM	Cecropin-Melittin
CM-SH	Cecropin-Melittin Cysteine terminated
CPU	Central processing unit
CQC	Computational quantum chemistry
CV	Collective variable
DDS	Drug delivery systems
DFT	Density functional theory
DMPC	1,2-dimyristoyl-*sn*-glycero-3-phosphocholine
FE	Free energy
FES	Free energy surface
fcc	Face-centered cubic
FF	Force field
GPGPU	General purpose graphics processing unit
GPU	Graphics processing unit
GVB	Generalized valence bond
HF	Hartree-Fock
HIV	Human immunodeficiency virus
HPC	High-performance computing
LL37	Cathelicidin-Derived
LL37-SH	Cathelicidin-Derived Cysteine terminated
MCSCF	Multi-configurational self-consistent field
MD	Molecular dynamics
MM	Molecular mechanics
MO	Molecular orbitals
MP2	Møller-Plesset second-order perturbation theory

MPI	Message passing interface
NMNP	Noble metal nanoparticle
NP	Nanoparticle
PAM	Peptídeos anti-microbianos
PBC	Periodic Boundary Conditions
PEG	Polyethylene glycol
PME	Particle Mesh Ewald
R&D	Research and Development
SCF	Self-consistent field
WHO	World Health Organization
WL	Water Layer

1. Introduction

1.1 Framework, motivation, and scope

The development of antimicrobial drugs during the past decades is remarkable. The evolution from the penicillin *Penicillium* in the late 1920s to the recent antibiotics, such as fidaxomicin and bedaquiline, is a paradigmatic case of a such development.[5] The noticeable success of antimicrobial drugs in the late 1960s and early 1970s resulted in the misconception that infectious diseases had been conquered. However, fifty years later, the World Health Organization (WHO) estimates that infectious diseases remain as the second leading cause of death worldwide.[6] This is a consequence of the extensive use of antibiotics over the years, and the concomitant emergence of multidrug resistance in common pathogens (Fig. 1.1), as well as the rapid appearance of new infections.[7] Thus, along with the research and development (R&D) of new ones, the continuous optimization of existing drugs is mandatory. By improving the targeting capabilities and stability of existing antimicrobial drugs, it will be possible to reduce the administrated amount. This, in combination with a rational use of antimicrobial drugs, will hopefully prevent the emergence of multidrug resistance pathogens.

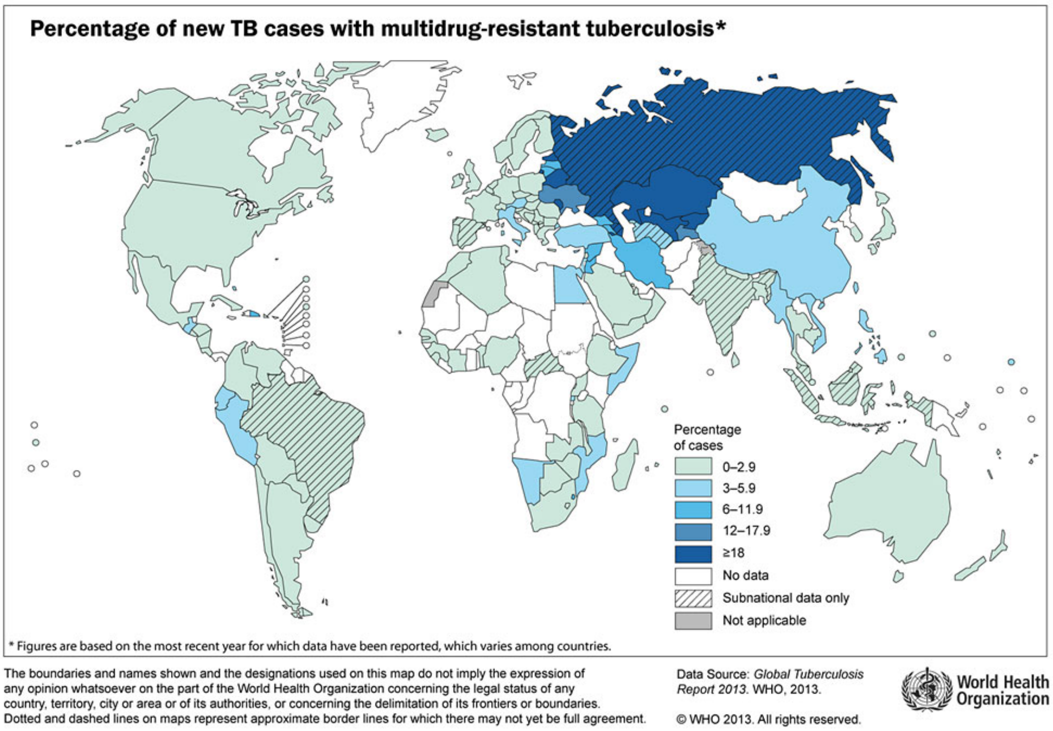

* Figures are based on the most recent year for which data have been reported, which varies among countries.

The boundaries and names shown and the designations used on this map do not imply the expression of any opinion whatsoever on the part of the World Health Organization concerning the legal status of any country, territory, city or area or of its authorities, or concerning the delimitation of its frontiers or boundaries. Dotted and dashed lines on maps represent approximate border lines for which there may not yet be full agreement.

Data Source: *Global Tuberculosis Report 2013*. WHO, 2013.

© WHO 2013. All rights reserved.

Figure 1.1: Percentage of new cases of tubercolosis that presented multidrug resistance according to the WHO. Reprinted with permission from[8] - Published by The World Health Organization.

More recently, WHO was requested by member states to develop a global priority pathogens list of antibiotic-resistant bacteria to help in prioritizing the R&D of new and effective antibiotic treatments.[9] In this list WHO focused only on bacteria (viruses and parasites will be addressed in future) ranking their priority based on criteria such as: all-cause mortality, healthcare and community burden, prevalence of resistance, 10-year trend of resistance, transmissibility, preventability in hospital and community settings, treatability and current pipeline. A group of 70 experts with different backgrounds and geographical origin were involved in the criteria weighting process. The WHO was able to identify a total of 12 bacteria, organized in three prioritizing tiers (medium, high and critical), which should be prioritized in terms of R&D.

With nearly 3000 Antimicrobial peptides (AMPs) registered in the antimicrobial peptide database,[10] their potential is tremendous.[11] AMPs are a class of antimicrobials abundantly existing in nature (more than 800 sequences), which are very effective against a broad range of micro-organisms, including Gram-negative and Gram-positive bacteria, fungi, and viruses. More, alongside these antimicrobial characteristics, AMPs can also control host physiological functions such as inflammation, angiogenesis, and wound healing.[1,12,13] AMPs are constantly available in multicellular organisms and serve as a first-line defense of the immune system, and, in case of inflammation and injury, its concentration increases.[11,14] With the enhanced resistance of pathogens to conventional antibiotics, the interest in the pharmacological application of AMPs has increased significantly.

As mentioned, the new trends demand creative improvements in the effectiveness and targeting capabilities of these antimicrobial drugs. Nanotechnology is one of the most promising ways to achieve such a goal. Worldwide, products incorporating nanotechnology present a multibillion-dollar revenue industry expected to increase to three-trillion-dollar by 2020.[15] Recent developments have prompted new and improved materials for biomedical applications, with particular emphasis in therapy and diagnostics, or their combination in the same nano-platform (theranostics). Nanoparticles (NPs) present a huge potential for biomedical applications. Due to their small size, they are able to interact with biomolecules both at surface and inside cells, yielding faster and better targeting specificity for therapeutic treatments.[16] Noble metal nanoparticles (NMNPs) are particularly suitable for nanomedicine. They present a great versatility, with applications ranging from highly sensitive diagnostic assays[17,18], radiotherapy enhancement[19,20], to drug and gene delivery[21–23]. In fact, the use of gold nanoparticles (AuNPs) to immobilize AMPs is not new. The end conjugate (AMP/AuNP) tend to retain the peptide activity, while benefiting of AuNPs targeting, thermal and bioimaging characteristics. During the past decade several studies emerged reporting the synthesis, characterization and activity of these materials.[1,2,24–26] In most of these studies the authors demonstrated an improvement of the AMP characteristics while immobilized in the AuNP.

Currently, there are several reported works describing the synthesis and characterization of AMP/NMNP conjugates[1,2,27–29]. A survey of the most significant results will be presented in Sec. 1.2. For now it is of interest to convene for this point a set of unanswered questions raised by a deep analysis of the existing investigations, namely: "how does the diffusion process prior to the adsorption of the AMP to the NMNP affects the final structure?"; "how selective is the adsorption process?"; "how long does it takes to achieve a sable conjugate?"; "how stable is the final conjugate?".[30–34] These questions have a common frame, i.e., they are referred to events occurring at nanoscale (or below) and in time scales ranging from femtoseconds (fs) to several hundreds of nanoseconds (ns). Despite the notable advances in experimental oriented techniques/equipment, the real difficulties in assessing the nanoscale in real time explains the lacking or even the nonexistence of actual results with such a detail. Recent multi-scale modelling and simulation techniques, supported by advanced and high-performance computing (HPC) resources, pave the way for the atomistic investigation of these materials and their interactions.[35]

Molecular modelling and simulation techniques emerged over the last years as a decisive practice in modern Chemical Engineering as a whole, and in Product Engineering in particular, allowing for a deep understanding of material structures, properties and interactions, starting at and below nanoscale. The theoretical (computational) study of crystalline and amorphous solids, nanostructures, supramolecular systems, liquids and solutions is now possible with acceptable simulation times thanks to the dramatic advances in HPC architectures and molecular modelling codes thereof. Indeed, with the proper articulation of several computational methods, it is possible to target a wide range of length (Å to nm) and time (fs to ns) scales.[36–38] Techniques such as computational quantum chemistry (CQC), static, dynamic, and classical molecular dynamics (MD) are good examples of methods which can be successfully used to investigate AMPs and AMP/NMNP interactions. Classical MD in particular has been a valuable tool in studying the adsorption process of some AMPs in to metal surfaces.[30–32]

MD can capture the behavior of biological macromolecules in full atomic detail. This technique enables the replication, computationally, of key biochemical processes such as protein folding, drug binding, membrane transport, and other conformational changes critical to protein function.[35] In fact, one can find several studies addressing adsorption process of peptides onto gold surfaces.[3,4,30,32,34,39] However, the topology of the surface is, most of the times, flat and the AMP dimension is small (less than 20 residues). Plus, these systems are characterized by multiple local minima which are separated by high-energy barriers, represented by a coarse energy landscape.[40–44] In order to properly address the conformation variability inherent to proteins/peptides, the production of multiple MD runs or the use of state-of-art sampling methods is recommended.

Given this framing, this PhD thesis looks towards contributing to understand how

AMPs interact with AuNPs, and how these conjugates (AMP/AuNP) affect cell membranes. Two AMP/AuNP systems were selected on the basis of their applicability, demonstrated in recent studies[1,2]. The objective of the study will be accomplished using a computational approach to tackle three interconnected specific objectives described as follows.

i) Study of the adsorption process *per se*. To investigate the overall adsorption capabilities of the selected AMPs to a gold surface. To assess the dynamic behavior of AMPs by investigating the regimes inherent to the adsorption process (electrostatic interactions, dispersion forces, structural rearrangements). To determine the AMP three-dimensional orientation of the atoms, their primary and secondary structures, and respective dynamic behavior while approaching and interacting with the gold surface.

ii) Free energy investigation by an advanced sampling method. To model and simulate the dynamic behavior of the AMPs chain interaction with gold surfaces through conventional MD supported by an advanced sampling method, viz. well-tempered metadynamics. To address the possibility of formation of metastable conformations, due to the strong interaction between gold and peptides. To thoroughly characterize the free-energy landscape by generating new data with statistical significance, capable of probiding a reliable picture of the AMP/AuNP interaction.

iii) Interaction of AMP/AuNP conjugates with a biomembrane model. To elucidate how the AMP/AuNP conjugates affect a biomembrane by investigating the mechanisms of interaction between them both. To search for the interplay between AMP, AuNP and AMP/AuNP with the bilayer and to provide information on the effect of a specific amino acid, or even a functional group, from AMP over the bilayer properties. To assess the capability of the conjugate, and its components, to permeate the bilayer and the underlying mechanisms.

Thesis outline

The thesis is organized in five chapters. The current chapter frames the theme, describes the motivation for the proposed work (Sec. 1.1), provides a overview of the state of the art (Sec. 1.2) of matters addressed in the work, viz. topics as AMPs, NMNPs, AMP/NMMP conjugates, their interaction with biomembrane, and how molecular simulation allows to shed light about the specificities of these materials.

Chapter **2** is referred to the computational approach used in the work (Sec. 2.1). It provides an overview on the software packages used and on the related mathematical the related models (Sec. 2.1.1). The chapter ends with a comprehensive explanation of system preparation and simulation protocol established to generate the results presented and discussed in the subsequent chapters.

Chapters **3** and **4** gather the core of the results achieved in this study, dedicated, respectively, to the cecropin-melittin (CM) peptides and to the cathelicidin-derived (LL37) based peptides. In both cases, the select approach and the underlying rationale is described, after which results are systematically presented and discussed. Apart from the interaction of the peptides with a gold surface (slab and AuNP for CM and AuNP for LL37), a study of the interplay of a LL37-SH/AuNP conjugate with a biomembrane model is also tackled.

Finally, Chapter **5** gives an overview of the achievements of this PhD project.

The content of the main body of the document is complemented by other relevant information compiled as **Appendix**. Additionally, several footnotes are used throughout the document to aid the reader in some technical terms less commonly used within the scope of Chemical Engineering.

1.2 State of the art

Medicine has been exploiting extensively the unique properties of nanomaterials. Widely referred as nanomedicine, it is nothing more than nanotechnology enabled medicine. The European Technology Platform on Nanomedicine defines nanomedicine "as the application of nanotechnology to Health. It exploits the improved and often novel physical, chemical, and biological properties of materials at the nanoscale. It has potential impact on the prevention, early and reliable diagnosis and treatment of diseases".[45] Although the first developments in nanomedicine are reported in the late 1960s during the ETH (Swiss Federal Institute of Technology) in Zürich, the major technological developments occurred throughout the past two decades. During this period, besides the technological advances, governments and scientific foundations took actions in order to establish regulations and create platforms to establish new investigation trends and strategies.[46] Nowadays, several countries have regulatory frameworks that address basic safety rules concerning nanomedicine.

When considering the use of nanomaterials for therapeutic purposes, drug delivery systems (DDS) are claimed as the most promising and used technique. DDS enhance the therapeutic effectiveness of the used drug through a controlled release and by improving its targeting capabilities. This is achieved by means of drug carriers, which include several types of materials, such as liposomes, polymers and metals.[47] Liposomes are biocompatible but find some drawbacks in terms of stability while in the bloodstream. On the other hand, polymers overcome the stability issues but may have biocompatibility problems. Currently, it is possible to find some works combining liposomes and polymers in order to obtain stimuli-responsive complexes.[48,49] However, if the active substances are proteins or peptides, the use of metallic based carriers is preferable. It is known that peptide-metal binding can be very strong leading to stable conjugates.[32] The particular case of NMNPs claim great potential. As already mentioned, NMNPs can be used simultaneous for diagnostic and therapy, i.e. besides the desirable therapeutic effect they can be tracked within the body, allowing a more efficient therapy with a reduced risk when compared to conventional therapies. Other important feature of some NMNPs, such as gold NP (AuNP), is that they are said to be non-toxic.[16]

1.2.1 Antimicrobial peptides

AMPs are a class of biomolecules which are very effective against several strains of bacteria, fungi and viruses.[11] Because they kill quickly and target the membrane nonspecifically, they are less prone to develop resistant bacteria than traditional antibiotics.[12] At the current stage, there are several databases of AMPs ranging from 2408 to 6756 sequences[50–52]. A literature survey allows us to categorize AMPs in several ways, as indicated in the listing below (see also Fig. 1.2):

1. Origin:[11]
    - Insects
    - Other animals
    - Engineered organisms
    - Synthesized
2. Function:[11]
    - Anti-bacteria
    - Anti-fungi
    - Anti-parasites
    - Anti-virus
    - Anti-cancer
3. Three-Dimensional Structure:[53]
    - α-Helical
    - Cysteine rich
    - β-Sheet
    - Regular amino acids rich
    - Modified with rare amino acids

Since our particular focus includes AMPs to be used for therapeutic effects, the categorization by function will be used throughout this project. As the name suggests, the categorization by function reports the type of pathogen that the peptide targets. The combination of AMPs to take advantage of their distinct characteristics is a well-know practice. In fact, aside from combining sections from APMs into a single one, Yu et al.[54] investigated the potential synergies from mixing multiple AMPs in a single pot. The authors investigated six different AMPs from different organisms to test their individual and combined effects *in vitro*. In order to do so, the pharmacodynamics was evaluated by combining two and three AMPs. A synergetic behavior was found in most cases, with the combination of three AMPs being higher. The authors have proposed the synergism as a common phenomenon in AMPs, stating that they displayed a sharp increase in killing within a narrow dose range (contrasting with antibiotics).

The first reported application of AMPs[55], in the early 1980s, was directed to bacteria. Since then known as anti-bacterial AMPs, this class represents more than 50% of the reported AMPs. Anti-bacterial AMPs can be subdivided into anti-Gram-positive, anti-Gram-negative or simultaneously anti-Gram-positive and negative. Bacteria can be Gram-positive or Gram-negative, and, despite being usually differentiated by the capability of

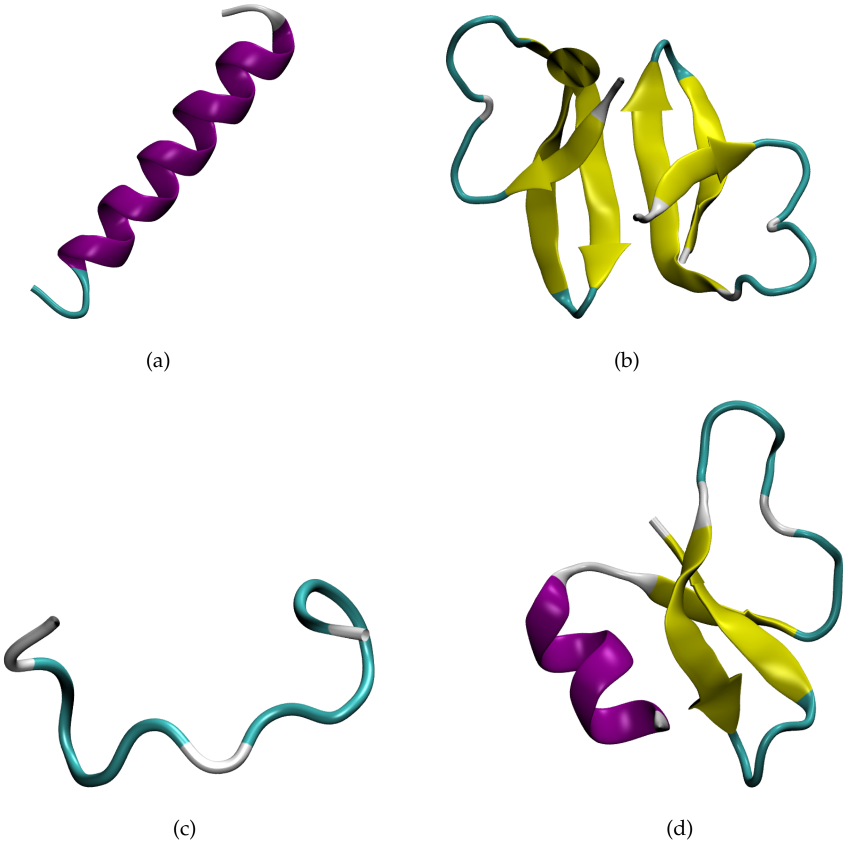

Figure 1.2: Possible 3D structures for AMPs and its ID name. (a) α-Helical (2MAG); (b) β-Sheet (3GNY); (c) Extended (1QXQ); (d) Mixed (2NLS).

retaining or not the violet stain, they present an essentially different outer cell wall, thus affecting the AMP effectiveness. Due to the increase of resistant bacteria, most research has been focused on the design and engineering of peptides. Field et al.[56] and Torcato et al.[57] have developed modified AMPs that target Gram-positive and Gram-negative bacteria. Field et al.[56] reported the first derivatives of nisin, with a serine to glycine change at position 29, with enhanced antimicrobial activity against both Gram-positive and Gram-negative bacteria. Torcato et al.[57] developed two newly designed BP100 analogues which, apart from being active against Gram-negative bacteria, showed activity against Gram-positive bacteria. This was made possible by the inclusion of arginine, which, together with the presence of a tryptophan residue, allows a deeper insert into the membrane environment of Gram-negative bacteria. Recent developments on anti-Gram-negative bacteria were reported by Jiang et al.[58,59]. The authors described a peptide D16 developed from the peptide D1 (V13). By optimizing the number and location of positively charged residues on the polar face and the number, location, and type of hydrophobic residues on the non-polar face, improvements in antimicrobial activity and dramatic reductions in hemolytic activity were achieved.[58] Three years later the same group published a study in which piscidin-1 and dermaseptin S4 were modified by substituting lysine at different positions. Apart from maintaining, and in some cases improving, the antimicrobial activity against Gram-negative pathogens, the hemolytic activity of human red blood cells was also dramatically decreased.[59] Falciani et al.[60] synthesized a M33 peptide isomer consisting of D-amino acids (M33-D). In this way, a higher activity against Gram-positive bacteria was achieved when compared to the original peptide, which was synthesized with L-amino acids (M33-L). According to the reported *in vivo* tests, M33-D showed 100% effectiveness against mice infected with *Staphylococcus aureus*[a], against 0% effectiveness of the M33-L.

There are also several recent examples of anti-fungi and anti-parasite peptides. Gupta et al.[61] reported the effect of the LR14 AMP produced by *Lactobacillus plantarum*[b]. It exhibited a strong anti-fungal activity when tested against fungi that are usually related with food spoilage. Results such as the prevented fungal growth under laboratory conditions for about 2.5 years on LR14 treated wheat seeds presented a huge achievement for the food storage industries. In order to develop new strategies that aiming at blocking malaria transmission, Carter et al.[62] examined a wide range of AMPs to be used against *Plasmodium*[c] and anopheline mosquitoes. After several test and screening processes, the authors were able to narrow down to five AMPs effective against malaria parasites. The AMPs Melittin, TP10, Vida3, Mastoparan X and Anoplin presented themselves as promising candidates to limit malaria transmission in *Anopheles gambiae*[d]. The authors emphasized the importance of using multiple peptides, acting in synergy, which could possibly achieve a complete transmission blockade within the mosquito.

The use of AMPs as anti-virus and anti-cancer agents is also being thoroughly investigated due to their great potential. The use of AMPs to target the human immunodeficiency virus (HIV) and cancer cells are paradigmatic cases of their potential. Indeed, Wachinger et al.[63] reported that melittin and cecropin A suppressed the production of HIV by acutely infected cells. The authors suggested that the AMPs appear to interfere with the cellular capacity to support HIV replication by suppressing HIV transcription, thus reducing the overall levels of viral gene products. More recently, Wang et al.[64] investigated LL37 and BMAP-27 derivate AMPs which are active against HIV. From the 20 synthetic AMPs, GI-20 and BMAP-18 showed the highest therapeutic index. As a consequence, these AMPs may now be used as templates for the engineering of novel anti-HIV AMPs. Anti-cancer AMPs are unique compared to other cytostatic[e] drugs by selectively interfering with cancer cells via a charge-triggered membrane disruptive mode of action.[65] Chang et al.[66] synthesized tilapia hepcidin (TH)1-5 peptides and tested

---

[a] Gram-positive bacteria that is frequently found on the human respiratory tract and on the skin.

[b] Derived from the genus *Lactobacillus*, with applications ranging from the food industry to the production of AMPs.

[c] Parasite that causes the malaria infection.

[d] Mosquito widely associated with the spread of the malaria infection.

[e] Inhibiting or suppressing cellular growth and multiplication.

their anti-tumor activity against several tumor cell lines. The results showed that TH1-5 exhibited potent disruption of tumor cell membranes and was able to selectively induce blockage of cell cycle progression of cancer cells. In other work, Ausbacher et al.[67] reported that even small $\beta^{2,2}$-amino acid derivatives (BAA-1 and BAA-2) are active against cancer cells. Although by means of different mechanisms, BAA-1 destabilizes the cell membrane and BAA-2 causes apoptosis[f] by the mitochondrial mediated pathway, both AMPs killed lymphoma cells.

Cecropin-melittin

Cecropin-melittin is a hybrid peptide that combines two well-know natural peptides (cecropin A and melittin) that exhibit potent antimicrobial activity.[68] Cecropins are positively charged antibacterial peptides that were first isolated from the hemolymph[g] of *Hyalophora cecropia*[h]. The antibacterial spectrum of cecropins is broad and includes both Gram-positive and Gram-negative bacteria.[69] It is a small peptide, with a number of residues ranging from 31 to 37. Cecripin A (KWKLFKKIEKVGQNIRDGIIKAGPAVAVV-GQATQIAK) is one member of the cecripin family that presents high potential as AMP. It is a naturally occurring, linear, cationic, 37 residue AMP, that kills bacteria by dissipating transmembrane electrochemical ion-gradients.[70] Melittin is the principal toxic component in the venom of the European honey bee *Apis mellifera*[i]. It is a 26 residue (GIGAVLKVLTTGLPALISWIKRKRQQ) peptide characterized by its amphiphilic property and antimicrobial attributes.[71] To date, melittin has shown its potential to be used in the treatment of the yeast *Candida albicans*[j] [72], to suppress *Mycoplasma hominis*[k], *Chlamydia trachomatis*[l] and *Staphylococcus aureus*[m] infections[73,74], as well as anticancer properties[75].

Besides their unique characteristics solo, these two AMPs present a great potential when combined. While the residues might not be necessarily the same, multiple publications can be found advocating the potential of cecropin-melittin (CM) hybrids. Boman et al.[76], Saugar et al.[77] and Ji et al.[78] are some of the authors that addressed this hybrid. Boman et al.[76] was able to prepare 5 different CM hybrids with different combinations of sections of cecropin and melittin. From these 5 CM hybrids, 4 presented good antibacterial activity against representative Gram-negative and Gram-positive bacterial species. The CecropinA(1-13)Melittin(1-13), with the sequence KWKLFKKIEKVGQGI-GAVLKVLTTGL, was found to be 1OO-fold more active than single cecropin A against

---

[f] A form of cell death in which a programmed sequence of events leads to the elimination of the cell.

[g] Hemolymph is a fluid, analogous to the blood in vertebrates, that circulates in the interior of the arthropod (arachnids, crustaceans and insects) body.

[h] North America native moth.

[i] Western honey bee, or European honey bee, found in Europe, the Middle East, and Africa.

[j] Fungi commonly available in the gut flora which can become pathogenic under a variety of conditions.

[k] Bacteria often present concurrently in the lower urogenital tract of healthy adults.

[l] Bacteria responsible for the most common sexually transmitted infection worldwide.

[m] Bacteria known to cause a wide variety of clinical manifestations

Staphylococcus aureus. Saugar et al.[77] was able to demonstrate that 4 CM hybrids are active against two *Acinetobacter baumannii*[n] strains resistant to common antibiotics. The CM hybrids were able to permeate the inner membrane, regardless of the resistance pattern of the strain. Finally, Ji et al.[78] reports the biosynthesis process of a CM mutant, named CAM-W (KWKLWKKIEKWGQGIGAVLKWLTTWL). This was develop for the first time using a *Bacillus subtilis*[o] strain that was genetically modified. The CAM-W entity shows more potent antimicrobial activity against a wide range of clinically important bacterial and fungal pathogens than its parental peptide.

Cathelicidin-derived LL37

LL37 is the only cathelicidin-derived antimicrobial peptide found in humans. It is formed by 37 residues, has amphiphilic behavior, in some cases it exhibits α-helical structure, but most importantly, it has been shown to have a broad spectrum of antimicrobial activity.[79,80] LL37 acts as first line of defense against bacteria, virus and fungi[81]. Turner et al.[82] described the LL37 peptide antibacterial potential. The authors have identified considerable activity of LL37 against multiple pathogens, such as the well-know *Pseudomonas aeruginosa*[p] and *Salmonella typhimurium*[q]. Furthermore, due to broad-spectrum antimicrobial properties of LL37, it is present in neutrophis[r], and its influence in keratinocytes[s] suggests that this peptide may protect skin and other tissues from bacterial intrusions. Hase et al.[83] have also reported a new use of LL37 in the targeting of gastric pathogen *Helicobacter pylori*[t]. The authors claimed that LL37 significantly increases in the epithelium and gastric secretions in patients infected with *Helicobacter pylori*. This suggests that LL37 determines the balance between host defense and survival mechanisms, related to increase of *Helicobacter pylori*, that governs chronic infection with this gastric pathogen. Howell et al.[84] investigated the effect of LL37 in the *Vaccinia* virus[u]. Data from electron microscopy studies have shown that LL37 has direct effects on the integrity of the *Vaccinia* viral membrane structure. This data made possible to foresee the potential of LL37 in the inhibition of virus *Vaccinia* replication.

In addition to the remarkable AMP characteristics of LL37 mentioned above, it also defends the organism by speeding wound healing.[85] In fact, Ramos et al.[86] confirmed that a recombinant[v] LL37 preserves its wound healing capabilities and immunophysio-

---

[n] Bacterial pathogen associated with hospital acquired infections.

[o] Gram-positive bacteria found in soil and the gastrointestinal tract.

[p] Gram-negative bacteria commonly associated with hospital acquired infections.

[q] Gram-negative bacteria that can cause infections often related to food

[r] Neutrophils are the most abundant type of granulocytes and the most abundant (40% to 75%) type of white blood cells in most mammals.

[s] Keratinocyte is the predominant cell type in the epidermis, the outermost layer of the skin.

[t] Bacteria associated with chronic gastritis and gastric ulcers.

[u] Virus associated with smallpox disease.

[v] Recombinant artificially produced (and often purified) protein/peptide.

logical properties *in vitro* and *in vivo*. Gronberget al.[87] performed trials with LL37 in 34 participants with venous leg ulcers (one of the most prevalent types of chronic wounds). The results showed a three to sixfold higher healing rate constant than those treated with placebo. Furthermore, the treatment was able to decreased the mean ulcer area, 68% for 0.5 mg/mL and 50% for 1.6 mg/mL groups.

1.2.2 Noble metal nanoparticles

Noble metals have the well-known attribute of being resistant to corrosion and oxidation. Unlike transition metals based NPs, noble metal NPs (NMNPs) have lesser cytotoxicity, making them attractive candidates for biological and environmental applications (Fig. 1.3).[88] In fact, NMNPs are finding use in molecular-specific probes, bioimaging, cancer diagnostics and therapeutics across the biomedical spectrum due to their surface-plasmon resonance-enhanced optical and thermal properties.[89] Moreover, they have been successfully used in novel cancer therapies.[90,91] Although NPs are not restricted to spherical shape, this is probably the most common geometry because it can be easily obtained with a simple reduction of metal salts by reducing agents. However, despite the favorable attributes of NMNPs, there are toxicity effects that must be taken into consideration. Properties such as NP size and type noble metal can dramatically influence the cytotoxicity[16].

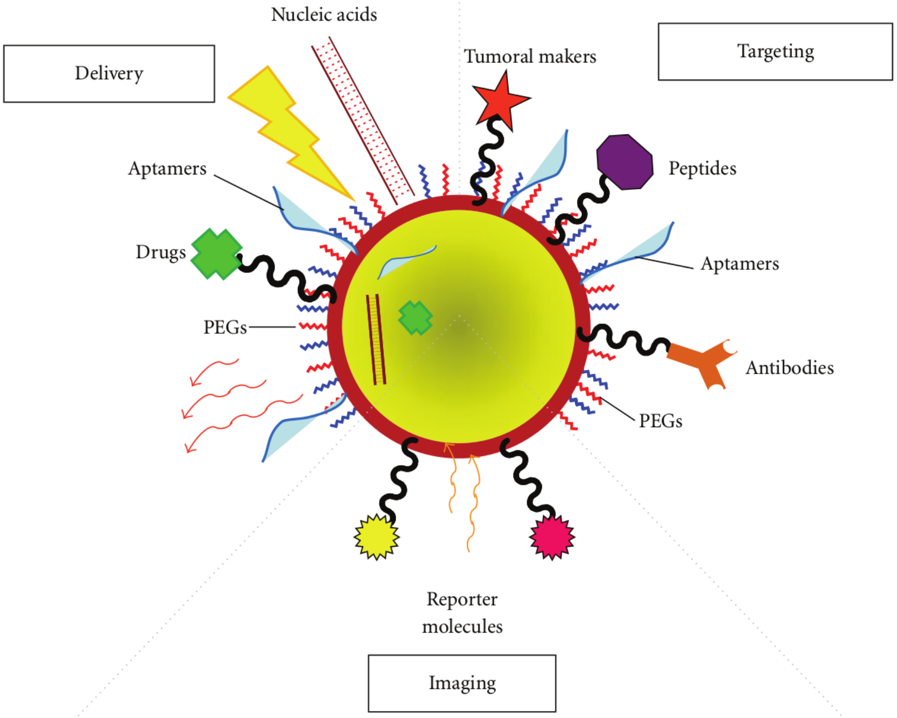

Figure 1.3: Schematic summary of potential characteristics and applications of NMNPs. Reprinted with permission from[16] - Published by Hindawi Publishing Corporation.

Among different possible NMNPs, silver NPs (AgNPs) and gold NPs (AuNPs) present the highest potential to be used in biomedical applications. Lara et al.[92] reviewed the recent advances in the understanding the biocidal mechanisms of action of AgNPs, and discussed the toxicity and the potential of AgNPs to be used as antibacterial, virucidal, and topical agents in mucosal human tissue, and topical agent on human cervical tissue. Indeed, one year earlier, Lara et al.[93] reported the antiviral effect of AgNPs on HIV-1. The results showed that AgNPs have anti-HIV activity at an early stage of viral replication by inhibiting the interaction of glycoprotein GP120 and the target cell membrane receptors. However, it has been shown that AgNPs are generally considered toxic, with several studies showing that cell exposure to AgNPs induced significant cytotoxicity[94–96]. More recently Xiu et al.[97] provided new insights into the mechanisms by which AgNPs exert toxicity to bacteria and other organisms. Contrary to common belief, properties such as size, shape, surface coating and surface charge did not affect the toxicity directly, which led the authors to advocate that antimicrobial activity of AgNPs results uniquely from the Ag^+ release, even at relatively low concentrations (few μg/L of Ag^+).

The applicability of AuNPs in current medical and biological research is extremely broad. Indeed, most therapeutic and imaging approaches based on noble metal NPs rely on AuNPs, mostly due to their low toxicity.[16,47] AuNPs have been extensively investigated for diagnosis and tracking applications.[18,98,99] In terms of cytotoxicity, AuNPs are considered to be benign, but at low diameters AuNP may present some cytotoxicity. In fact, Pan et al.[100] performed a systematic investigation of the size-dependent cytotoxicity of AuNPs, showing that specimens with 1 to 2 nm, were highly toxic, whereas those with 15 nm were comparatively nontoxic against the tested cells. The surface of the AuNPs also plays an important role regarding cytotoxicity. Modified or functionalized AuNP surfaces may present a totally different behavior from the unmodified ones. Simpson et al.[101] reported *in vivo* toxicity tests of glutathione-coated AuNPs. The authors suggested the replacement of polyethylene glycol (PEG), which reduces the potential of AuNPs[102], by glutathione. The synthesized glutathione-coated AuNPs with diameter ranging from 0.9 to 1.2 nm, were capable of rapid passage into the kidneys and bladder, and mice injected with glutathione-coated AuNPs did not experience any clinical signs of illness, stress, or discomfort, nor did any expire over the course of the entire 6-week study. Bozich et al.[103] investigated the toxicity effect of polyallylamine hydrochloride (PAH-AuNPs), citrate (Cit-AuNPs) and mercaptopropionic acid (MPA-AuNPs) functionalized AuNPs. Overall the NPs ranged from 4 to 5 nm and were tested against *Daphnia magna*[w]. The results showed that negatively-charged AuNPs, Cit-AuNPs and MPA-AuNPs, were orders of magnitude less toxic than the positively-charged, PAH-AuNPs. However, chronic exposure showed that both types of AuNPs affect *Daphnia magna* reproduction capabilities. The authors

---

[w] Water flea from the *Daphnia* genus widely used as a laboratory animal for testing ecotoxicity.

suggested that positively-charged AuNPs could have a high affinity towards the negative charged surfaces of the cellular membranes, causing higher toxicity.

Nonetheless, the mechanisms that govern AuNPs toxicity are still unclear. Properties such as surface charge[104–106], particle size[100,107,108], the type of coating and ligand density[109,110] on the surface and aggregation over time[111,112] have been advocated as the cause of toxicity.[113] However, it is important to stress that nearly anything can be toxic at a high enough dose and at specific concentrations. When addressing toxicity assays, the main question is to know how toxic are AuNPs at the potentially usable concentrations (estimated to be 1 to 100 NPs per cell[114]).[115]

1.2.3 Functionalized AuNPs

AuNPs used as nanocarriers have dramatically grown in the pharmaceutical field for intracellular drug and gene delivery. Apart from being quite easily synthesized, with fine control of size and shape, they present a large interacting surface, low environmental background level, and unique optical properties, thus having many potential commercial applications. Furthermore, unlike other functionalized metal and metal oxide NPs, AuNPs are resistant to dissolution and do not exhibit significant changes in size or shape under typical environmental and biological conditions.[103] This originated great interest on the functionalization of the AuNPs in an attempt to enhance their intrinsic properties from the combination with different materials.[47,91] In spite of this topic has been slightly addressed previously when discussing toxicity effects (Sec. 1.2.2), the current section deals with the end-function of the functionalized AuNP.

Gibson et al.[116] reported the example of 2 nm AuNPs covalently functionalized with chemotherapeutic drug, paclitaxel. The authors described the attachment of a flexible hexaethylene glycol linker to phenol-terminated AuNPs. The final product was a drug/AuNP conjugate which is soluble in organic solvents and able to retain its average size, shape, and high crystallinity after multiple synthetic steps and purifications. The results proved the concept that it is possible to covalently attach organic molecules to AuNPs in a controlled fashion. This opened a new door to the development of novel hybrid particles with a well-defined amount of drugs, offering new alternatives for the design of new nanosized drug-delivery systems. At the same time Saha et al.[117] and Grace et al.[118] functionalized a total of six drugs over the surface of AuNPs. All drug/AuNP conjugates presented high stability, some of them showed higher activity against the tested bacteria, and only two conjugates showed significant decrease in the activity when compared to the free drug.

Years later Serizawa et al.[119] have reported a novel synthetic route to produce peptide-capped AuNPs. The obtained conjugates presented approximately 10 nm diameter and narrow size distributions. This was achieved by combining cysteine terminated peptides with 2-[4-(2-hydroxyethyl)-1-piperazinyl]ethanesulfonic acid (HEPES) and tetrachloroaurate ions. The AuNP growth was found to be slow, and was attributed to the affinity between the gold and the thiol groups (in cysteine), which was preferentially captured during the AuNP growth instead of the HEPES molecules.

Rai et al.[120] have reported a method to synthesize AuNPs from cefaclor, a β-lactam second-generation antibiotic, that allowed to obtain NPs ranging from ca. 22 to 52 nm. The authors showed that the amine group present in cefaclor acts both as a reducing agent, responsible for the AuNP growth, and a capping agent. The latter attribute allowed cefaclor to keep its activity, which was proved later by the potent antimicrobial activity of the conjugate on both Gram-positive and Gram-negative bacteria. More recently, Kumar et al.[121] have reported the development of peptide functionalized AuNPs to be used in cancer treatment. The authors described the synthesis of 2 nm AuNPs functionalized with the therapeutic peptide PMI (p12) and a targeted peptide, CRGDK, for cancer treatment. The selected peptides aimed at inhibit MDM2, MDMX and neuropilin-1 (Nrp-1) complexes which are related to tumor development. The nanocarrier, named Au@p12 + CRGDK, was successfully synthesized and characterized. The uptake of p12 was significantly facilitated by cancer cells due to Nrp-1 mediated and the complex exhibited stronger *in vitro* anti-cancer activity than other conjugates.

NPs functionalized with AMPs have recently been proposed for the treatment of infectious diseases, such as hantavirus cardiopulmonary syndrome and meningitis. It has been shown that NPs increase the stability of AMPs in biological environments, enhancing their antimicrobial properties, presumably due to an increase in the local density of positive charges and peptide mass. This also allows the combination of other functionalities (such as targeting) in the same formulation.[28,29] Since the earlies 2000s several publications regarding these kind of materials have emerged. In 2003 Gu et al.[27] developed AuNPs functionalized with vancomycin, a glycopeptide antibiotic, and its *in vitro* antibacterial activity. This was achieved by previously functionalize AuNPs surface with Au−S bonds which then reacted with the peptide. During their investigation, the authors were able to demonstrate that a low aggregation of the complexes was achieved. Finally, it was shown from *in vitro* assays that the the peptide kept its activity after bonded to the AuNP.

In this context, Rai et al.[1] and Comune et al.[2] have investigated the functionalization of AuNPs with CM and LL37, respectively. Rai et al.[1] have reported a one-step synthesis of CM/AuNP conjugates with high AMP concentration, low polydispersity and controlled size. The reasoning behind this characteristics was mainly attributed to the presence of a thiol group located at the C-terminal of the AMP. The authors have advocated that this functional group controls the reduction rate of the Au ions, leading to the the observed enhanced properties of the conjugate when compared to the soluble AMP, namely higher stability and activity, without compromising the low cytotoxicity against human cells.

Similarly, Comune et al.[2] have reported that LL37/AuNP conjugates presents higher *in vivo* and *in vitro* bioactivity when compared to the soluble LL37. Additionally, the authors demonstrated that the conjugate exhibit regenerative properties mediated by an increased IL6[x] production. This is a particularly relevant attribute since many chronic wounds get infected during healing process.

More recently, Zong et al.[122] have reviewed the topic of peptide-functionalized gold nanoparticles. They addressed subjects such as the synthesis, properties and applications of of these materials. The process was differentiated in three groups, viz. ligand exchange (displacement of one ligand for another), chemical reduction (reduction promoted by the peptide residues) and chemical conjugation (chemical biding between peptide sites and AuNP). They also have explored the application of these materials in terms of sensitive biosensors, drug carriers, anti-cancer therapeutics and gene delivery vectors. Despite the remarkable potential of these materials, the authors identified some issues that still need to be to be solved, such as the "elucidation of mechanisms of molecular recognition on the surface of GNPs", as well as the "mechanism of internalization of peptide-GNPs into cells"[122].

1.2.4 Cellular uptake of nanoparticles

The penetration of NPs into cell membranes is a phenomena that has been extensively investigated during the past decades. In fact, the process on how NPs interact with a membrane presents great interest within the scientific community[123], characterized by the large amount of publications in the field. Since the ultimate objective is to use the materials under study as therapeutic agents, and considering we are still characterizing and validating their applicability, most of the cellular uptake studies fall within the scope of toxicity assessment. Obviously, when talking about cellular uptake, one should notice that the conclusions drawn from a specific system (NP-cell combination) can dramatically change by a small shift in the system conditions.

Albanese et al.[110] reported an holistic approach of the subject, by rationalizing multiple studies on "The Effect of Nanoparticle Size, Shape, and Surface Chemistry on Biological Systems". The premise is that by identifying how size, shape and chemistry of NPs influence the delivery, one should be able to maximize their effect. In the review, the authors identify three generations of NP when addressing the Nanoparticle design subject. The first generation was the proof of concept of these materials. It was demonstrated the potential applications, established synthesis processes and assessed their biocompatibility. The modification and optimization of the surface chemistry was addressed during the second generation. It mostly focused on the use nanoparticles to diagnose and treat cancer with two different approaches, stealth and active targeting. The stealth concept

---

[x] Interleukin, expressed by with blood cells, with a role during inflammation and immune response.

aimed at maximizing the blood circulation life to ensure the continuous delivery of the material to the targeted location was also developed at this stage. This was achieved by adding PEG[124] and lipids[125] to the NP surface. Unfortunately, active targeting did not achieve drastic increase in tumor targeting during this generation. To address this outcome, researchers developed a new generation (third) of nanomaterials. This generation was characterized by having materials with environment-responsive properties. These NPs use biological, physical or chemical cues in their target environment to trigger modifications of their properties. One example, is the use of PEG that acts as pH-triggered shield described by Poon et al.[126]. This shield is used to reveal, while within a given range of pH, a positively charged surface that causes nonspecific uptake of drug-filled nanoparticles. A analogous model can be found in Fig. 1.4, where the triggering cue is the temperature. Albanese et al.[110] state that, despite the already demonstrated great value to the fields of optics and electronics, it will be important to characterize the effect of nanomaterials on biological systems.

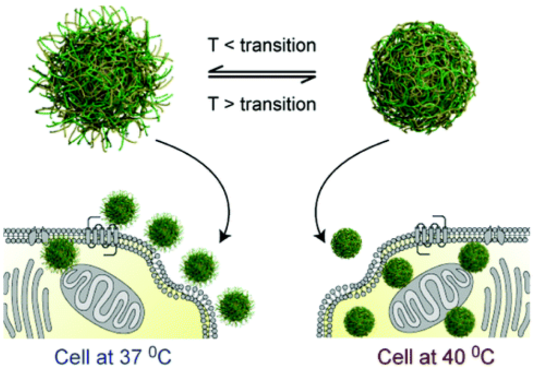

Figure 1.4: Schematic representation of the formulation of a thermoresponsive NP. Below the thermal transition temperature the NP outer shell is hydrophilic (left-hand side) and less prone to enter the cell. When the temperature goes above the thermal transition temperature, the NP surface becomes hydrophobic (right-hand side) and the nanomaterial enter the cell easily. Reprinted with permission from[127] - Published by The Royal Society of Chemistry.

One of the first questions that arise when investigating cellular uptake is how the diameter will affect the uptake dynamics. Shang et al.[128] published a review with the outcome of multiple publications concerning nanoparticles interacting with cells, with special attention to the size property. The authors were able confirm that NP size may affect the uptake efficiency and kinetics, the internalization mechanism (Fig. 1.5), and also the subcellular distribution. Moreover, size-dependent interaction of NPs with the cell membrane is likely related to the membrane-wrapping process that initiates endocytosis. While small NPs have less ligand-to-receptor interactions than the larger ones, multiple small NPs are required to simultaneously interact with the receptors in order to trigger membrane wrapping. On the other hand, large NPs can induce uptake by cross-linking the receptors. It should be noticed that if a protein corona is present, the cellular response towards the NP might differ. In the end, the authors conclude that: "i) There is an optimal size for efficient endocytosis of NPs independent of the particle composition; ii) This critical size can vary with cell type and surface properties of the NPs; iii) Small NPs have a higher probability to be internalized by passive uptake than large ones; iv) Under otherwise identical conditions, small NPs are more likely to cause toxic cellular responses". More recently Moser et al.[129] shared their results for a system with AuNPs. The author stated that AuNPs have diameter-dependent cellular uptake and retention. From spectral position determination microscopy the authors were able to observe that on average, the uptake by incubation after 2 h was approximately double for 10 nm AuNPs when compared to 25 nm AuNPs.

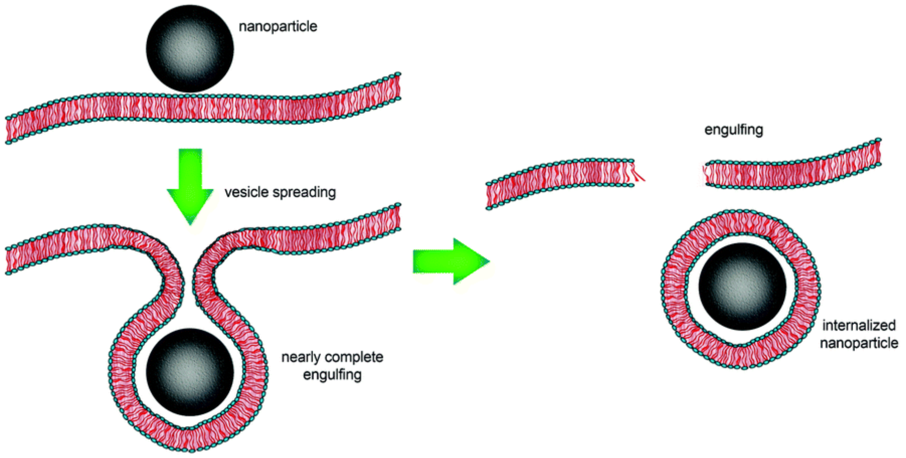

Figure 1.5: Schematic illustration on how the internalization of a NP occurs into a liposome through active process. Reprinted with permission from[130] - Published by The Royal Society of Chemistry.

This topic was further explored by Fratoddi et al.[131]. The authors summarized the current state-of-the-art about the toxicity of AuNPs and provided an overview of the most recent experimental results. Fratoddi et al.[131] mentioned the importance of surface functionalization of the AuNPs because they influence cellular uptake more strongly than hydrophobic or van der Waals interactions. By changing the surface charge, the AuNPs become prone to be internalized within a cell by endocytotic pathways.[132] The authors cited some publications that demonstrate that, despite having a positive effective surface charge after being synthesized, the AuNP were no longer cationic within the cellular media. This should be consequence of the adsorption of plasma protein to their surface, adopting the physico-chemical properties of the adsorbed material.[132–134] This shell is called protein corona and is known to strongly influence cellular uptake.[134] Regarding the effect of the AuNP diameter on the cellular uptake, it is mentioned that smaller size AuNPs plays a major role in the cellular uptake. A study conducted by Chithrani et al.[135] showed that maximum cellular uptake occurred at a AuNP size of 50 nm for 6 h in

Dulbecco minimum essential media[y] plus 10% serum. A similar study was conducted by Connor et al.[114] and Murphy et al.[115] on human leukemia cells. The results suggested that none of the AuNPs (4, 12, and 18 nm in diameter) used were toxic. However, due to the number of fundamental issues that remain to be addressed, Fratoddi et al.[131] end their paper by questioning the *status quo* that AuNPs are non-toxic. The authors argue that a collaboration between different research groups should be established the properly correlate physico-chemical properties of AuNPs and their effects on biological structures.

1.2.5 Computational-based studies

The use of computational techniques to investigate the interaction of proteins or peptides with gold surfaces started to emerge during the late 2000s-early 2010s. Most authors justify the use of these techniques as a way to understand the underlying adsorption mechanism of proteins on surfaces, which is yet not well understood, due to the difficulty to analyze them experimentally. In 2012 Bellucci et al.[33] issued a book chapter which describes the principles, assumptions and limitations of *ab initio*, classical atomistic MD, and other methods applied to computationally investigate the interaction of proteins with gold surfaces. The publication is mainly focused on the work developed by their group, which is both experimental and computational. The authors start by stating that "[w]hile various experimental methods have been used to explore protein-surface interfaces these are by no means routine experiments. In this context, computational simulations can provide an important contribution to the understanding of protein surface interaction.". This quote highlights quite well the potential of computational techniques to study these type of interactions, anticipated above. After the initial considerations, the authors present several systems investigated by different computational methods. The first section reports the use of *ab initio* methods, time independent and time dependent. With these methods, the authors have investigated the interaction of small amino acids, such as cysteine and histidine, with a gold surface[136,137], and data such as adsorption energies, electronic density of states and bonding and antibonding orbitals have been reported. Regarding time dependent methods, more specifically Car-Parrinello MD, it is presented a short excerpt with results from the interaction of polyserine with a {111} gold surface. It should be stressed that, because of the system size (ca. 600 atoms), these simulations required a supercomputer to be performed. Løwdin net atomic charges during the simulation for the gold atoms, for oxygen atoms of water and oxygen of serine side chains have been reported. With these data it was found that there is an electron donation from the serine hydroxyl groups and water molecules to the gold surface leading to a net electron accumulation on the outer gold layers. It was also found that the hydration layer plays an important role on the adsorption process, since it acts as the last layer between the

---

[y] Synthetic media formulated to cell media culture.

peptide and the gold. The authors have also reported some results from systems simulated with classical MD methods, such as residue-surface distances, adsorption energies and trajectory analysis.

Hoefling et al.[138] investigated the interaction of polypeptides with β-sheet folds with {111} gold surfaces. The authors observed that the amino acid arginine facilitated the initial contact between the protein and the surface. The adsorption was very strong and fast. However, the polypeptides did not unfold on the gold surface within the simulation time despite the domain of orientation changes. Similarly, Yu et al.[31,32] investigated the interaction of a small peptide with gold surfaces. In this case, besides the gold slab, it was also investigated the interaction with gold nanoparticles. The tested peptide was the A3 (AYSSGAPPMPPF). This study led the authors have discriminated the following regimes in the binding process: i) diffusion regime, characterized by diffusion of the peptide through water while approaching to the gold surface; ii) anchoring regime, occurring when the first residue of the peptide touches the surface; iii) crawling regime, confined between the first anchor and the formation of the first stable bond of the peptide on the Au surface; iv) binding regime, between the first stable bond and the full stabilization of the peptide on the surface. The authors were also able to establish that tyrosine, methionine, and phenylalanine are strong binding residues, and serine serves as an effective anchoring residue. When comparing the adsorption energies of the peptide to gold nanoparticles different sizes (2.3 nm, 3.2 nm, 4.6 nm and 6.0 nm) the authors found that the size effect plays an important role in the stabilities. It was found a critical size threshold near 5 nm, beyond which the strong binding of peptides limits or slows the AuNP from further growth.

The adsorption mechanism of peptide/surface systems was further explored by Penna et al.[39]. The authors performed 240+ molecular dynamics simulations for periods ranging from 20 ns to 100 ns on two systems, viz. SD152 (CPTSTGQAC) peptide with a platinum surface and a A3 peptide with a gold surface. They advocated that by simulating two completely distinct systems a generalized peptide adsorption mechanism at a molecular level could be obtained. Overall, Penna et al. were able to identify three different phases in the adsorption mechanics: i) biased diffusion; ii) anchoring; iii) lockdown. The first phase was the one which introduced new insights in the field. Until then, it was unknown what was the trigger that promoted the diffusion of the peptides towards the surface. The authors also reported that the existence of water layers adjacent to the solid, and orientational ordering therein, project the surface potential around 0.8 to 1.0 nm into the water. They claimed this long-range force as the source that induces the start of the biased diffusion phase. The subsequent phases, i.e. anchoring and lockdown, also described in the study of by Penna et al. are in line with what was reported previously by Yu et al.[31,32] earlier.

More recently, Shao et al.[139] investigated the influence of the AuNP diameter on the adsorption process of 19 natural amino acids. The authors applied well-tempered metadynamics simulations (see Chap. 2) to compute the potentials of mean force between the entities. This approach permitted to understand the dependence of the binding preferences of each amino acid upon different AuNP sizes (1, 2 and 4 nm of diameter), as well the role of the respective backbone and side chain in that preferences. The simulations showed that AuNPs with higher diameters had water solvation shells denser than those with lower sizes. The solvation shell differences were preponderant in establishing the specific amino acid interacting with the AuNP. Those whose binding free energy depended mainly on their ability to reorient water molecules (Asp, Glu, Met, Phe, Thr, Trp, and Tyr) preferred a smaller, 2 nm, AuNPs. The remaining amino acids (Ala, Arg, Asn, Gln, Gly, His, Ile, Leu, Lys, Pro, Ser, and Val) preferred the larger AuNP, 4 nm, a consequence of their binding free energy be mainly depend on the replacement of water molecules.

Within the realm of metallic nanoparticles it is important to highlight the work developed by Heinzet al.[140,141]. Since the early 2000s, the Heinz's group have been developing and validating the force field parameterization of several inorganic nanostructures to be used in classical MD calculations. Since all the classical MD codes were firstly developed for organic systems, most of the inorganic entities are still lacking of a proper parameterization or a parameterization at all. This issue requires the combination of a wide set of experimental and computational tests, as well an extensive know-how of the details underlying the force field structure. From all the work developed, the most relevant in this context are those for metallic entities and biomolecular adsorption[30,142], in which the molecular interactions of short peptides with surfaces of Au, Pd, and Pd-Au bimetal were thoroughly investigated. A quantitative analysis of changes in energy and conformation upon adsorption on different types of surfaces, viz. {111} and {100} (Fig. 1.6), was also assessed.

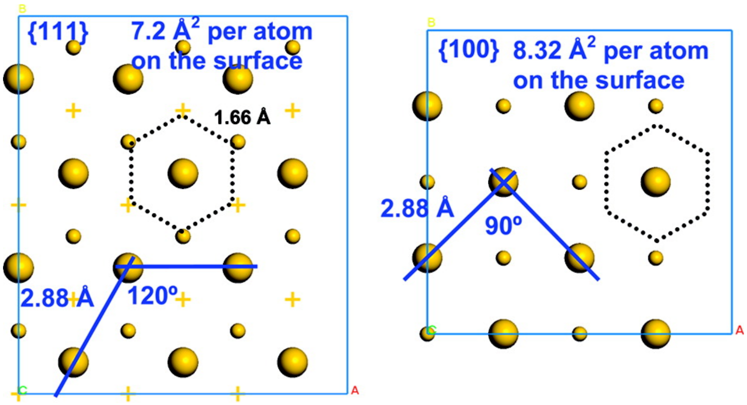

Figure 1.6: Comparison of the geometry of the {111} (left) surface with {100} (right). Reprinted with permission from[30]. Copyright 2018 American Chemical Society.

The authors were able to observe changes in the chain conformation from the solution to the absorbed state and conclude that the peptides interact preferably with vacant sites on the face-centered cubic (fcc) lattice above the metal surface. It was also observed that the residues that contribute to the biding process are in direct contact with the surface whereas the other residues are found with one or two layers of water between them and the metallic surface. The spacing available between lattice sites on the surface {111} was found to be beneficial to the adsorption of aromatic side groups as well various other residues. On the other hand, the quadratic spacing between available lattice sites on the {100} surface presented much lower affinity with the peptides. More recently, Feng et al.[143] and Heinz investigated the adsorption mechanism of single amino acid and surfactant molecules to Au {111}. The authors found that the adsorption energy is related with molecular size and geometry rather than the specific molecule chemistry. Large molecules with planar sp^2 hybridized groups adsorb more strongly, followed by molecules with polar sp^3 hybridized groups, and short molecules with sp^3 hybridized alkyl groups exhibit less attraction. Ultimately, the authors were able to show that the computational results are consistent with combinatorial binding experiments, observations in the growth and stabilization of metal nanoparticles, and *ab initio* data.

Cysteine is one amino acid with very interesting characteristics, mainly ascribed to the presence of a thiol group. Besides participating in enzymatic reactions, it is very susceptible to oxidation. This property has been exploited to bind peptides or proteins to metal surfaces, such as gold. In order to determine the nature itself of the anchor atoms, Gronbeck et al.[144] and Andreoni et al.[145] investigated how thiols and disulfides bind to gold surface. Since these type of interactions imply the variation of states of oxidation, the use of *ab initio* or DFT techniques is crucial. The authors were able to obtain a complete characterization of the complexes, binding energies, and the type of bond formed. The authors found that the binding energy of the thiol to the surface only differs $3\,\mathrm{kcal\,mol^{-1}}$ depending on dissociation of the S−H bond. This means that thiolates resulting from S−H bond cleavage in thiols can coexist with the adsorbed "intact" species. Later, Kruger et al.[136] investigated gold-sulfur bonding using a variety of electronic structure methods. The authors found that, structurally, the thiolate sulfur-gold bond has a distinctive directional (covalent) character which results in a clear preference for Au-S-C bond angles in the range of 103.5° and 108.7°. Based on *ab initio* simulated annealing, the authors were able to show that the thiolate-gold interaction can lead to the rearrangement of the gold atoms of the structure. However, the authors have stated that "the effects of chain length on sulfur-gold bonding have to be assessed in order to devise meaningful models".

In order to understand the complexity underlying the preparation of biochips, Piana et al.[146] investigated how the biochemical properties of the immobilized molecules can be influenced by the inorganic surface, more specifically DNA with the gold surface. To achieve this, the authors simulated the interaction of adenine, thymine, cytosine, and guanine (four nucleobases) with a gold surface by performing DFT, post-Hartree-Fock and classical MD calculations. From the DFT calculations, the authors were able to observe that the nucleobases are preferably oriented parallel to the gold surface. Despite the substantial charge polarization of the surfaces, the authors conclude that the interactions between the gold surfaces and the nucleobases, except for adenine, should be described as a physisorption. With the post-Hartree-Fock calculations, more specifically Møller-Plesset second-order perturbation theory (MP2), the Lennard-Jones parameters to describe the nucleobase-surface interaction were derived. These parameters were tested by performing classical MD simulations of monolayers of methane, ethylene, benzene, and pyridine adsorbed on the gold surface. After validated, the parameters were used to obtain the the binding energy of nucleobases with the gold surface at different levels of coverage. These computed values were then compared with their experimental counterparts. A remarkable agreement was found, with the exception of the value for cytosine. This is a clear indication that Lennard-Jones parametrization derived from the MP2 is good enough to properly characterize these entities.

Despite the numerous experimental studies performed in the past few years to probe NMNP-cell interactions, the cell uptake mechanism of NMNP is still poorly understood. While cytotoxicity measurements give astounding results of NMNPs with different physical and chemical characters, the principles underlying NMNPs cytotoxicity are not yet established. In fact, the lack of atomic-level details on NMNP-cell interactions continues to be a drawback to consistently new developments in the field. Some authors[147] have already performed MD simulations of the interaction of AMP-NMNP complexes with biomembranes. Nevertheless, coarse-grained models (end Sec. 2.1.1) and approximations thereof were used, thus missing atomistic detail.[147,148]

As mentioned in Sec. 1.2.4, cellular uptake is a very complex and difficult subject to address. The simulation of systems characterized large spacial and time scales often require simplifications in the mathematical model. Within this context, the work of Lin et al.[147] should be highlighted. The authors applied classical MD to investigate the penetration of lipid membranes by AuNPs. However, a coarse-grain model of the system was used. Despite loosing some resolution, by oversimplifying the system, the coarse-grain approach enables the simulation of larger systems for longer time, the simulation of phenomena such as membrane penetration being a notable example. By functionalizing ligands to the AuNPs with different charges and surface densities it resulted in either repulse of, adhesion to, or penetration into the lipid bilayers. It was also found that the interaction between the AuNPs and bilayers was governed by electrostatic interactions of the ligand terminals on the AuNPs with the bilayer head groups. Upon penetration of the AuNP, a pore is formed which transports water between the layers. Ultimately, the findings from the Lin et al.[147] investigation suggest that it is possible to control the AuNPs cellular uptake by tuning its surface charge density. Gkekaet al.[149] also have used similar models (coarse-grain) to investigate the permeation of nanoparticles through lipid membranes. This simplification permitted to understand if the organization of the corona, homogeneous or heterogeneous, affects the passive translocation of the NP through the bilayer. In the end, the authors have postulated that, if preserved, homogeneous patterns facilitate permeation of NP through lipid membranes by preventing lipid aggregation on its surface.

In short, AMP-NMNP complexes present a great potential in the treatment of wide range of diseases. Nonetheless, the lack of experimental tools that enable the motorization in real time and at the nanoscale, precludes a complete understanding of important phenomena, such as diffusion, binding and cell membrane permeation, on which data are either scarce or non-existent. The use of advanced molecular modelling and simulation techniques may consistently provide fundamental insights into research and development of AMP-NMNP systems.

2. Methods and computational details

2.1 Molecular dynamics

Currently, the (possibly) only way to study the dynamic behavior of the described NP based systems at an atomistic level relies on molecular modelling and simulation tools. Molecular dynamics (MD) methods, classic or *ab initio*, present a huge potential in a such kind of investigations (Fig. 2.1).

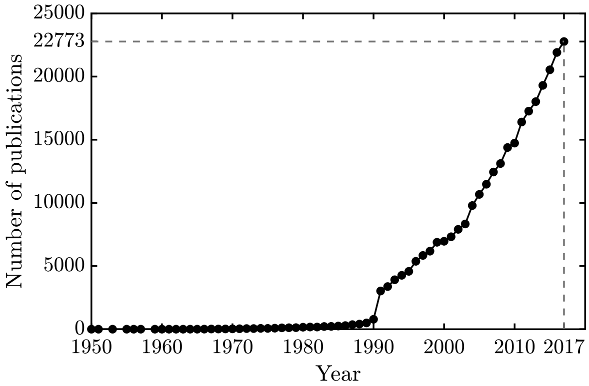

Figure 2.1: Number of publications indexed by Web of Science with the topic "molecular dynamics".

Computation quantum chemistry (CQC) resorts to a high level of theory, i.e. *ab initio* and density functional theory (DFT) based methods, in order to describe molecular systems with electronic detail, typically without including the time component. On the other hand, classical MD adds the time variable to the simulations, thus enabling the assessment of dynamic behavior, although from a classical molecular mechanics (MM) approach (the generic mathematical formalism of MD will be addressed in Sec. 2.1.1). Depending on the size of the molecular system and the available computational resources, MD can also be performed within a so-called *ab initio* MD (AIMD) framework. The most common AIMD method is based on DFT, thus incorporating the electronic effects in the the dynamic simulations. It should be stressed out that these type of computational simulations require a huge processing workload. AIMD-based calculations are out of the scope of the current work.

The articulation of the available techniques allows to target a wide range of length (Å to nm) and time (fs to ns) scales.[37,38,150]. The use of central processing units (CPUs) based clusters has been the way *par excellence* to overcome this issue. Still, very recent and noticeable increase in the performance of graphics processing units (GPUs) boosted computing power one step beyond, enabling faster simulations of larger systems.[151,152] In fact, the advent of the GPU computing, during the early 2000s, lead to a paradigm shift in computing science. Nowadays, a modern GPU is not only a powerful graphics engine, but is also highly parallelizable programmable processor that features peak arithmetic and memory bandwidth substantially superior to its CPU counterpart.[153,154] If we narrow down to computational chemistry field, common MD, CQC, visualization, and docking applications more than 5 times faster when compared to CPUs.[155] Some authors, such as Kutzner et al.[156] and Pall et al.[157], performed a thorough analysis to assess which hardware is most economical using GROMACS (performance vs. price). In both cases, the authors found out that by adding a GPU to a computer node, the simulation performance is significantly boosted (see Fig. 2.2 for performance gains of adding GPUs to the calculations). The performance/price ratio is even higher when we consider consumer-class GPUs.[156]

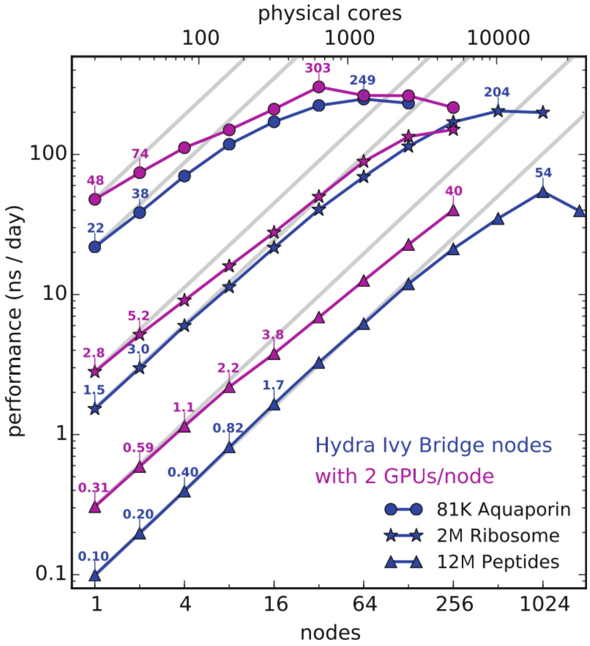

Figure 2.2: Scaling of GROMACS 4.6 on the HYDRA heterogeneous GPU-equipped machine in Garching, Germany. Gray lines indicate linear scaling. Note that the scale is logarithmic. Reprinted with permission from[157] - Published by Springer International.

Biomolecular simulations became one of the go-to tools to capture the behavior of biological macromolecules in full atomic detail. This technique enables the replication, computationally, of key biochemical processes such as protein folding, drug binding, membrane transport, and the other conformational changes critical to protein function.[35] In fact, one can find several studies addressing adsorption process of peptides onto gold surfaces.[3,30,32,39] However, in some cases, these algorithms fall short. Biological systems are characterized by rough energy landscapes, with many local minima separated by high-energy barriers (Fig. 2.3).[40–44] With the increase of computational power, it is now possible to probe the free-energy variation of a specific protein taking in account its conformation. This enables the production of data with statistical significance, which, until recently, was only achievable by performing several independent simulations. Due to the significant development of MD codes and computing power availability, it became possible to model and simulate larger systems for tens to hundreds nanoseconds. Nonetheless, the production of a single trajectory is most likely not going to probe all relevant conformations. Approaches such as replica exchange[158] and metadynamics[159] (see Sec. 2.1.1) are some of the most used methods to address the sampling issue. Conceptually these methods work similarly, in a way that causes a perturbation in the system by adding a biased potential. The nature of this bias potential is what differentiates the methods. This approach facilitates the characterization of the free-energy landscape while producing data with improved statistical significance.

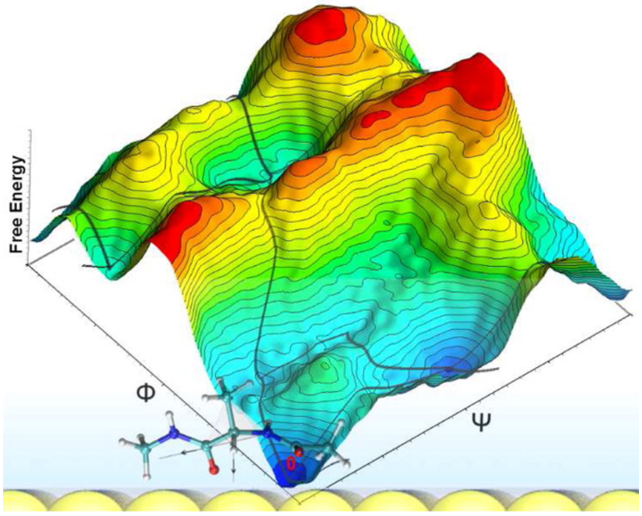

Figure 2.3: Adsorption free energy profile between Au111 and dipeptide. Reprinted with permission from[34]. Copyright 2018 American Chemical Society.

2.1.1 Mathematical background

Standard MD simulation consists essentially in finding the numerical solution of the classical equations of motion. The Hamiltonian of the system can be used, considering all energy contributions in which the degrees of freedom take part. The formulation is defined for a system of N particles with masses $\{m_1...m_N\}$, velocities $\{v_1...v_N\}$ and cartesian coordinates $\{r_1...r_N\}$. The variables r and v are time, t, dependent. The Hamiltonian that describes a system by its coordinates, is formed by two terms, representing the kinetic, K, and potential, V, energy[160,161]:

$$H(p,r;m,s) = K(p,m) + V(r,s) \ , \tag{2.1}$$

were H is the Hamiltonian, p the momenta, r the particle coordinates, m the mass and s the force-field parameters.

The calculation of the kinetic energy is quite simple. It corresponds to the sum of the kinetic energy of all the particles of the system:

$$K(p,m) = \sum_{i=1}^{N} \frac{p_i^2}{2m_i} = \sum_{i=1}^{N} \frac{1}{2} m_i v_i^2 \ . \tag{2.2}$$

The potential energy term (Eq. 2.5) describes the energy of the interaction between the atoms in terms of their coordinates, r, and the force-field parameters, s. The force-field parametrization is based on experimental data and/or *ab initio* calculations. However, to perform a MD simulation, one needs to calculate forces on atoms, F_i, apart from the potential energies. To compute the forces, MD simulations solve Newton's equations of motion for a system of N interacting atoms, in short time iterations (fs):

$$m_i \frac{\partial^2 r_i}{\partial t^2} = F_i \ , \tag{2.3}$$

where the forces are the negative derivatives of a potential function, V:

$$F_i = -\frac{\partial V(r,s)}{\partial r_i} \ . \tag{2.4}$$

The force-field parametrization consists on several contributions, which are divided in two major types: bonded and nonbonded. Interactions such as bond stretch, angular vibration and torsions are considered bonded interactions, whereas van de Waals and electrostatic interactions are included in the nonbonded interactions (Fig. 2.4).

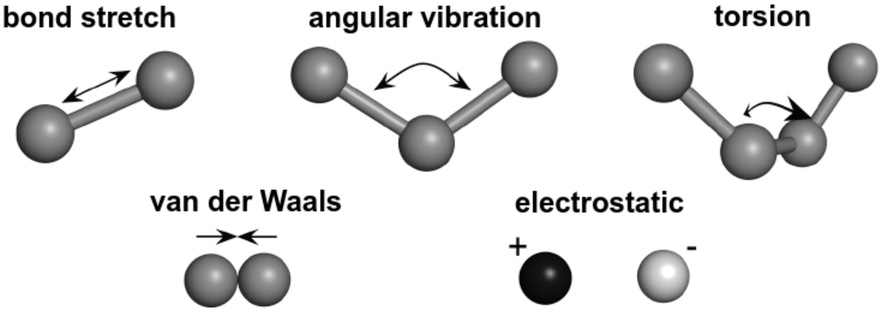

Figure 2.4: Molecular interactions (adapted from[162]).

The combination of all contributions the potential function is then expressed as:

$$\begin{aligned} V(r,s) = &\sum_{\text{bonds}} \frac{k_b}{2}(r_{ij} - r_{ij,0})^2 + \sum_{\text{angles}} \frac{k_\theta}{2}(\theta_{ij} - \theta_{ij,0})^2 \\ &+ \sum_{\text{torsions}} \frac{k_\phi}{2}[1 + \cos(n\phi_{ijkl} - \gamma)] + \sum_{\text{improper}} \frac{k_\xi}{2}(\xi_{ijkl} - \xi_{ijkl,0})^2 \\ &+ \sum_{i,j} 4\varepsilon_{ij} \left[\left(\frac{\sigma_{ij}}{r_{ij}} \right)^{12} - \left(\frac{\sigma_{ij}}{r_{ij}} \right)^{6} \right] + \sum_{i,j} \frac{q_i q_j}{4\pi\epsilon_0 r_{ij}} \ . \end{aligned} \tag{2.5}$$

The first four and the last two terms in equation 2.5 are the mathematical representation of, respectively, bonded and nonbonded interactions. The first term treats the variations of the bond length, r, between atoms i and j. The second term gives the angular variation, θ, formed by two adjacent bonds. The third term corresponds to the torsion, ϕ, defined from three atomic bonds, and the periodicity of the molecule is characterized by the n and γ parameters. This description is useful to distinguish between *cis* and *trans* conformations. The fourth term treats the improper dihedral, defined as the angle formed by two atomic planes, which is very useful for aromatic molecules and enantiomers (Fig. 2.5).

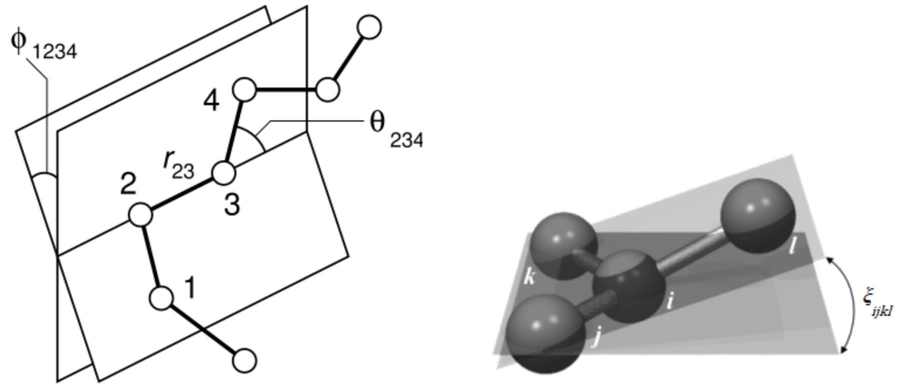

(a)

(b)

Figure 2.5: (a) - Geometrical illustration of an atomic bond r_{23}, angle θ_{234}, and torsion ϕ_{1234} of an hypothetical molecule[163]. (b) - Schematic representation of a molecular dihedral[164].

The van der Waals interactions (fifth term) are described using the Lennard-Jones potential, in which σ is the collision diameter and ε the depth of the potential well. Finally, the last term refers to the electrostatic interactions based on the Coulomb's law, in which q is the partial charge.

All these parameters are referred as force field (FF). This involves hundreds, if not thousands, of parameters that need to be selected in a way that ensures an accurate representation of the Hamiltonian of the system. Currently, there are four popular force fields: GROMOS[160,165–168], AMBER[169,170], CHARMM[171,172] and OPLS[173,174]. The latter is more oriented to model lipid based systems. In contrast, GROMOS, AMBER and CHARMM force fields are more specific for proteins, amino acids and nucleic acids. This partially reflects different parametrization philosophies.

Some force fields allow to create more simplistic molecular models, and three major types of molecular description can be identified: all-atoms, when all atoms are described; united-atoms, when each aliphatic methylene group is treated as a single particle; coarse-grain, when functional groups are agglutinated in a single particle. Figure 2.6 illustrates such representations for the lipid 1,2-dimyristoyl-*sn*-glycero-3-phosphocholine (DMPC).

The simplest way to develop a force field for a new molecule, based on one of the major biomolecular force fields, is by analogy with molecules that have equal or similar functional groups that are already described. Still, this "[p]rocess is tedious, time-consuming, and error-prone"[175] for larger molecules such as polymers. Moreover, to create a proper

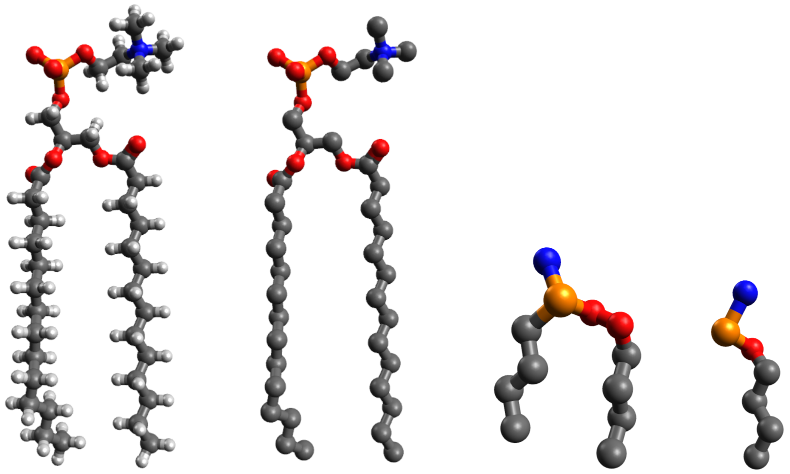

(a) (b) (c) (d)

Figure 2.6: Representation of a DMPC lipid: (a) - All-atoms; (b) - United-atoms; (c) - Coarse grain; (d) - More simplistic coarse-grain model.

parameterization for a new molecule, a deep knowledge of the force field background is required, since some parameterizations are tuned with some empiricism. To overcome these problems, several research groups have been developing tools to generate the parameterization of new molecules requiring only as input the atoms coordinates. Some of the most popular tools to generate new parameterizations are the PRODRG server[176], the Automated Topology Builder (ATB)[175], and SwissParam[177].

2.1.2 Advanced sampling methods

Mathematically, advanced sampling methods work out as an external layer to the classical MD, either running multiple analogous systems parallel that share information between them or by adding a bias potential to the system. This way, classical MD is able to overcome local minima and explore a larger section of the energy landscape. Fig. 2.7 highlights a free energy surface with multiple local minima.

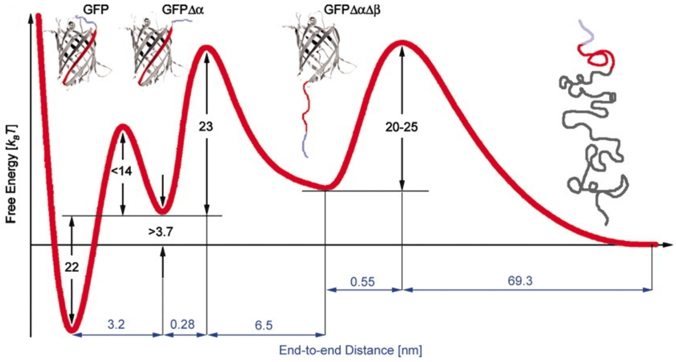

Figure 2.7: Projection of the energy landscape along the unfolding pathway onto one reaction coordinate. Reprinted with permission from[178] - Published by the National Academy of Sciences.

Replica exchange

Replica exchange (also known as Parallel Tempering) method is based on the premise that systems at higher temperatures can overcome energy barriers easier. A first version of this method was introduced by Swendsen et al.[179] as a variant of Monte Carlo. However, it has became quite popular since it was modified by Sugita et al.[180] to be used in the MD framework.

Replica exchange molecular dynamics (REMD) starts by choosing a temperature range. For a small protein, the selected temperature range is usually characterized by 15 to 50 temperature points, with values in the lower range of 270–300 K to 400–500 K at the highest range. This range should cover biologically relevant temperatures as well as those where sampling is significantly enhanced (viz. higher temperatures). After the multiple simulations (replicas) start running in parallel, the energy of neighbor replicas is compared occasionally. When the potential energy of the replica at higher temperature is lower, the coordinates of the replicas exchange. In this case, the replica at lower temperature continues at higher temperature and *vice versa*. A schematic view of this workflow can be seen in Fig. 2.8.

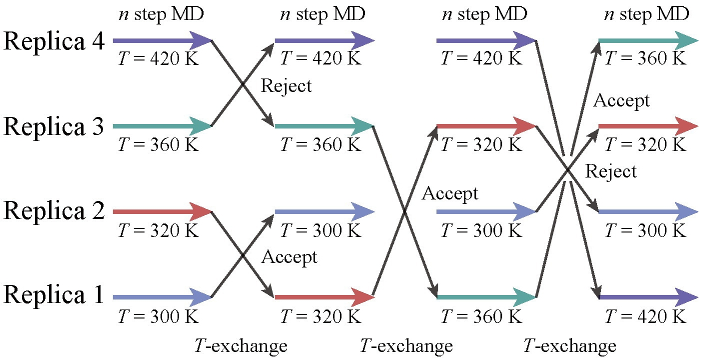

Figure 2.8: Generic scheme of a REMD workflow. Reprinted with permission from[181] - Published by Elsevier B.V..

In any other situation, a shift in the coordinates of the replicas exchanged is given by exchange probability. This probability is calculated from the potential energy difference as:

$$P = e^{\left(E_i - E_j\right)\left(\frac{1}{kT_i} - \frac{1}{kT_j}\right)}, \tag{2.6}$$

where E_i and E_i and T_i and T_j are energies and temperatures of the *i*th and *j*th replica, respectively, and k is the Boltzmann constant.[42] This probability is then compared with a random number generated by the computer. If P is higher, then the exchange occurs.

Metadynamics

Another way to improve sampling capabilities of standard MD is by applying metadynamics, which is a powerful technique, initially described by Parrinello et al.[159,182], for enhancing sampling simulations and reconstructing the free-energy surface (FES) as a function of few selected degrees of freedom, often referred to as collective variables (CVs). The algorithm discourages previously visited sates being resampled, allowing to allocate computational resources to explore a broader section of the FES (Fig 2.9).

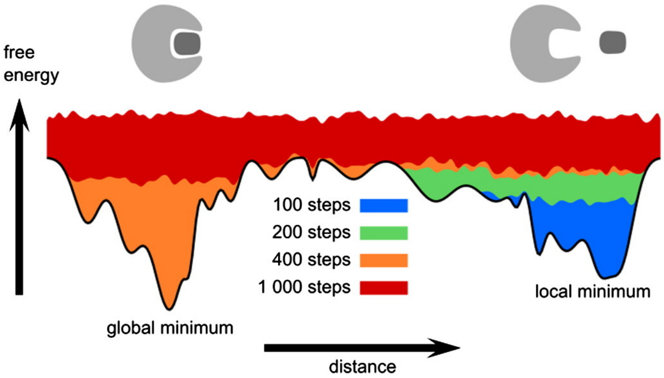

Figure 2.9: Schematic representation of metadynamics flooding on a model energy surface of a protein-ligand interaction. Reprinted with permission from[42] - Published by Elsevier Inc..

The process starts with the selection of CVs, usually 2 or 3. This is a crucial step as pointed out by Parrinello et al.[159] by stating that "[i]dentifying a set of CVs appropriate for describing complex processes is far from trivial". The simulation itself starts as an usual classical MD, the only difference being the addition of a bias potential hill to the system at regular intervals. At time t, the metadynamics bias potential can be written as:

$$V_G(S,t) = \int_0^t \omega \exp\left\{ -\sum_{i=1}^{d} \frac{\left[S_i(R) - S_i(R(t'))\right]^2}{2\sigma_i^2} \right\} \mathrm{d}t', \tag{2.7}$$

where ω is an energy rate, σ_i is the with of the Gaussian for the ith CV, and S is a set of d functions of the microscopic coordinates R of the system:

$$S(R) = (S_1(R), ..., S_d(R)). \tag{2.8}$$

The energy rate constant (ω) is usually expressed in terms of the Gaussian height W and decomposition stride τ_G:

$$\omega = \frac{W}{\tau_G}. \tag{2.9}$$

In the end, this technique presents several advantages: i) it accelerates the sampling of rare events by pushing the system away from local free-energy minima; ii) it allows exploring new reaction pathways as the system tends to escape the minima passing through the lowest free-energy saddle point; iii) no *a priori* knowledge of the landscape is needed, since it inherently explores the low free-energy regions first; and iv) the bias potential V_G provides an unbiased estimate of the underlying free energy.[159]

Within the scope of metadynamics, a new algorithm, named well-tempered metadynamics, was proposed by Barducci et al.[183]. Well-tempered metadynamics was designed to be able to overcome some of the metadynamics limitations, such as the inability of the free energy to converge to a definite value, fluctuating around the correct result, and avoid pushing the system to regions not physically relevant. This is achieved by smoothly reducing the initial Gaussian height (W_0) based on user defined ΔT and the simulation time:

$$W = W_0 \exp\left(-V_G(S,t)/\Delta T\right) \tau_G. \tag{2.10}$$

Since the intrinsic nature of the metadynamics is to add bias potentials to the system, one must invariably reweight the FES after producing the simulation runs.[184] The reweight consists in the neutralization of the potential added to system in order to determine the full unbiased distribution. All the analysis performed should be based on the reweighted FE values.

Ultimately, well-tempered metadynamics was the algorithm selected to enhance the sampling the targeted systems. The reasoning behind this selection is that it allows to select which CVs to probe and only requires a single simulation run to sample and characterize the system FES.

2.2 Computing details

This section gives an overview of computer codes used in this work to model, simulate and to process data, as well as a short description of the hardware used to perform those tasks. It also includes a set of technically relevant details shared by all performed calculations. Further modelling and simulation details that are specific of each target system will be provided in Chaps. 3 and 4.

2.2.1 Software and hardware

GROMACS[157,185–189] was the selected MD software package. It is a well-known and widely used classical MD code, with major applications in biochemical systems. Due to its excellent performance in calculating nonbonded interactions, it has been used also in the simulation of non-biochemical systems. One of the main benefits of GROMACS is its bottom-up performance-oriented design towards highly efficient use of the underlying hardware. GROMACS is written in C and it is well suited for parallelization on processor clusters. The careful optimization of neighbor searching and inner loop performance placed GROMACS on the forefront of fastest MD simulation packages. The code encompasses a minimal-communication domain decomposition algorithm, full dynamic load balancing, a state-of-the-art parallel constraint solver, and efficient virtual site algorithms that allow removal of hydrogen atom degrees of freedom to enable integration time steps up to 5 fs for atomistic simulations also in parallel. GROMACS is free, available under the GNU General Public License, and can be run in parallel, using standard MPI communication.

PLUMED2[190] plug-in was used in conjunction with GROMACS to perform metadynamics simulations. PLUMED is an open source library for free energy calculations in molecular systems which works together with some of the most popular MD engines. Free energy calculations can be performed as a function of many order parameters with a particular focus on biological problems, using state of the art methods such as metadynamics, umbrella sampling and Jarzynski-equation based steered MD. The software, written in C++, can be easily interfaced with both fortran and C/C++ codes.[191]

Data treatment was mostly performed resorting to the toolboxes provided by the GROMACS suite. Apart from being very fast, it provides a large selection of flexible tools for trajectory analysis. Fig. 2.10 depicts a generic flowchart of the a typical preparation and simulation of a system for a GROMACS run. Overall, the simulation can be divided into three sections. The first is dedicated to the preparation of the system, in which all molecules are modelled with the respective FF, and the simulation box is prepared to mimic the system under study. The second section corresponds to the simulation itself, which consists in solving the system step by step using the formalism summarized in Sec. 2.1.1. The last section is dedicated to data treatment and visualization. At this stage, the outputs from the simulation can be either treated using the included toolboxes or simply visualized by means of external software. The workflow is similar when running metadynamics, the only difference being the existence of a parallel code to **mdrun** (PLUMED) that updates the system forces with the selected bias potentials. A schematic diagram of the process can be seen in Fig. 2.11. A more in depth overview of the preparation and simulation processes, as well the a short description of the type files and their content, is presented in appendix A.

The analysis of bilayer properties such as area per lipid (A_{lip}) and bilayer thickness (D_{HH}), was performed using the APL@Voro tool[192]. This tool uses the triangulation between key atoms of the lipids, thus ensuring high accuracy of the computed metrics.

The trajectory outputs from MD calculations were analyzed through the VMD[193] package. Apart from being rather versatile, with most parameters being highly customizable, it allows to export high resolution and quality snapshots and movies from the loaded trajectory.

Most of the referred codes require some level of data processing before and/or after the MD run. To achieve this, MATLAB™[194] is a quite good choice due to its versatility

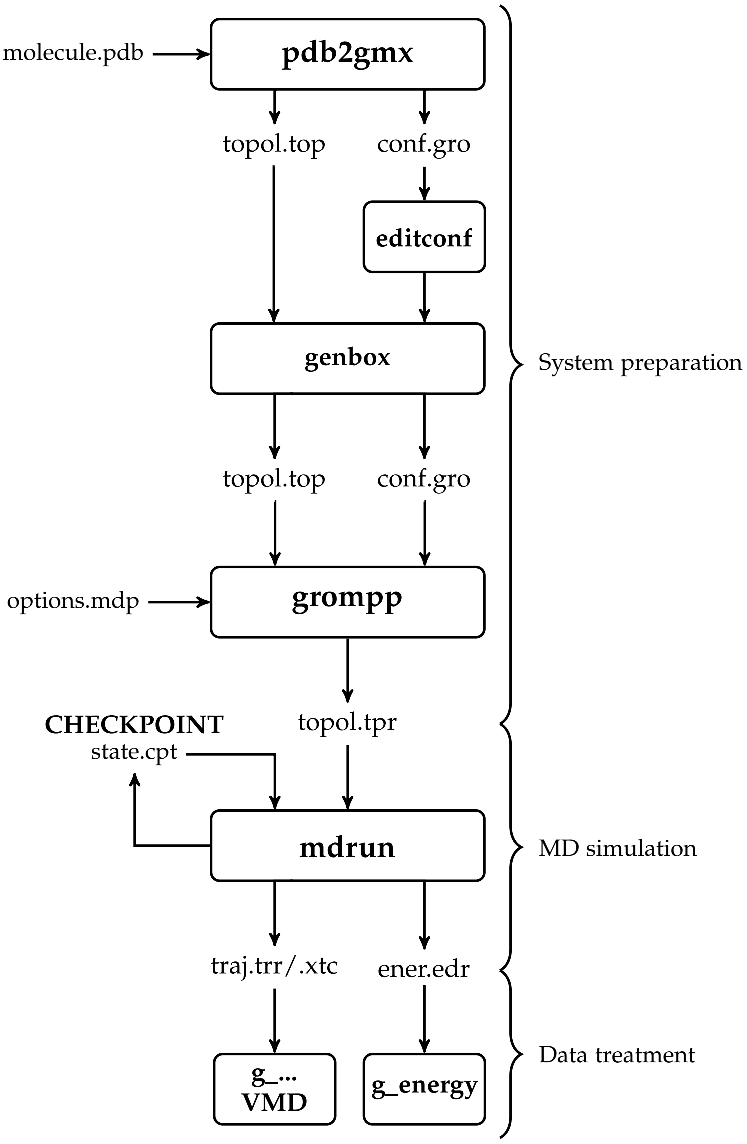

Figure 2.10: Generic flowchart of the modelling and simulation processes with the GROMACS package.

and robustness to manage, treat and represent large amounts of data.

Regarding the hardware available for carrying out this work, it includes a computer cluster with ten computing nodes, each equipped with two 3.06 GHz Intel™ Xeon™ Gulftown EM64T architecture with Hyper-Threading technology. The computing nodes are connected by gigabyte ethernet, used for NFS and for the Apache HTTP Server, and Inifiniband™, which provides high throughput and low latencies, which are critical attributes in HPC clusters. Rocks 6.1 (64-bit version) is an open-source Linux cluster Red Hat based distribution that was used since it enabled to easily build computational clusters. As MPI protocol, the MVAPICH2 version 1.7 is used. Added advantage was also taken from the capabilities of general-purpose computing on graphics processing units (GPGPU). In doing so, a Ubuntu 14.04 64 bit workstation based on Intel™ Xeon™ CPU

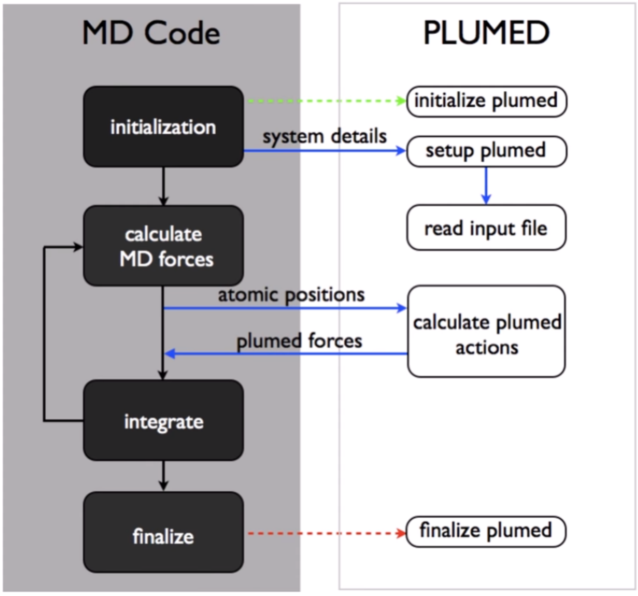

Figure 2.11: Interface between regular MD and PLUMED when running metadynamics simulations. The gray section, described as MD code, corresponds to the **mdrun** block of Fig. 2.10. Reprinted with permission from[190] - Published by Elsevier B.V..

E5-2620 processors and four Kepler based Nvidia™ Geforce™ GTX 780 were used. Each GTX 780 was equipped with 2304 CUDA cores which can be used to accelerate the computations. At the moment GROMACS is among a short group of MD packages that support CUDA accelerated calculations.

2.2.2 Modelling and simulation technicalities

The MD simulations which are reported in Chaps. 3 and 4 were performed with GROMACS v4.5.4[157,185–189] for the conventional approach, and GROMACS v2016.1[157,185–189] with the PLUMED2[190] plug-in for the metadynamics studies.

The Au structures were modelled using force field parameters developed by Heinz et al.[140]. The Au slab model considered was formed by 6 Au layers (24 by 32 atoms per layer) in a {111} geometry[31]. For AuNP, 4.2 nm and 6 nm diameter models formed by 1985 and 6531 Au atoms, respectively, were used, with face-centered-cubic lattice, dominated by {111} and {100} facets.

The ff99SB force field[148] and TIP3P[195] were to describe, respectively, the peptides and water molecules. For the simulations with the biomembrane, the SLipids[196,197] force field was used to model both the lipids and cholesterol.

The bilayer formulation was based on the Keratinocyte cells[198], and was sized in order to accommodate at least an additional LL37-SH/AuNP conjugate in each direction. This scheme prevents the conjugate from interacting with its own image, causing artifacts. Overall, the bilayer was formed by 1440 lipids (cholesterol included) with a molecular

POPC:POPE:POPS:CHOL ratio of 4:2:1:3, and 124971 water molecules.

The peptides were firstly relaxed in aqueous solution at 298.15 K, with the resulting conformations used as the initial structures for the subsequent simulations. All systems were pre-equilibrated using energy minimization runs. The box volume was relaxed for 100 ps in NPT ensemble under periodic boundary conditions (PBC). The simulation time varied from simulation to simulation (see each corresponding system in Chaps. 3 and 4), and were performed with a 2 fs time step, in NVT ensemble under PBC. The temperature was fixed at 298.15 K using the Nose-Hoover thermostat[199]. The electrostatic interactions were treated with the particle mesh Ewald (PME) method[200,201] with a real space cutoff of 1.0 nm. A cutoff of 1.2 nm was applied to Lennard-Jones interactions. Hydrogen bonds were constrained with the LINCS algorithm[202,203]. A neutral pH was used in all simulations.

3. Cecropin melittin hybrid based AMP

Cecropin-melittin (CM) is a peptide with a broad antimicrobial activity and great potential to inhibit fungal plant pathogens which displaying low hemolytic properties[76,204]. Very recently it was reported a study on new AMP-conjugated NPs, based on AuNPs and CM as the AMP, in which a cysteine amino acid was added to the C-terminus of the peptide (CM-SH)[1]. The CYS residue was added aiming at favoring the orientation of the peptide on the Au surface and to enhance the peptide activity. This approach was proved to improve the AMP effectiveness and achieve high antimicrobial activity after *in vivo* administration of the complex while keeping low cytotoxicity against human cells. Nonetheless, and despite most of CM peptide properties and antimicrobial capabilities being already described like most of other AMPs, a detailed description on how CM based peptides interact with noble metal surfaces is still laking.

In this context, a systematic computational investigation of the interaction of a cecropin-melittin hybrid (CM-SH) with a Au surface was carried out. The peptides were simulated in presence of water and then in the a presence of a gold slab. The outcome of these simulations allowed to establish a baseline of the systems to be used onwards as reference, and to clarify how to outline the required simulations (viz. simulation time, number of molecules in the system, distance between entities, etc.). To accomplish this, two distinct approaches were used. The first one, classical approach, consisted in the simulations of multiple analogous independent systems. Additionally, advanced sampling methods, that force the system to probe the complete structural landscape, were used as the second approach to probe the systems.

Forty independent all-atom MD simulations with 100 ns length of the interaction of the CM (20 simulations) and CM-SH (20 simulations) peptides with a $\{111\}$ Au surface were performed was part of the classical approach. This approach was selected based on the nature of the system in order to ensure that statistical significance is achieved, and to provide new data, such as diffusion trends and residue (or even moieties) preferences during the adsorption process. The investigation was mainly focused on the CYS immobilized peptide (CM-SH) in an attempt to bridge our computational results with the experimental counterpart recently reported[1]. Our MD-based study also looked toward validating this concept (CYS immobilization) and toward understanding how does the adsorption process takes place by carefully investigating each regime – biased diffusion, anchoring and lockdown – recently postulated by other authors[32,39]. Despite the special focus on the CM-SH peptide, both CM and CM-SH specimens and their residues were individually analyzed in order to discriminate their role in a specific stage of the adsorption process.

The dynamic behavior of the AMPs interacting with AuNP was also assessed by MD.

With the introduction of the AuNP in the system, it was possible to evaluate the influence of the surface geometry, and, at the same time, narrow the difference between the systems being simulated and the experimental data. A 6 nm AuNP composed by {111} and {100} facets was used to interact with the AMPs. The approach used to prepare the systems was slightly different. Instead of preparing five independent systems with each peptide (CM and CM-SH), two systems with one AuNP and five APMs of each kind was built. Using this approach it was possible to reduce the number of simulations perform (each peptide in the system can be analyzed independently) and assess the effect of AMP concentration into the adsorption mechanisms which govern the process.

Advanced sampling methods, namely well-tempered metadynamics, were used to the study of the adsorption process of the CM and CM-SH into the gold slab. This approach allowed to characterize the system free energy based on the select set of collective variables. This is extremely valuable since it allows, as an example, to have the system free energy as function of the distance between the AMP and the Au Slab. Moreover, unlike the classical approach, metadynamics only requires the simulation of one system of each kind (CM-SH with Au slab and CM with Au slab) to ensure statistical significance. Additionally, the outcome of these simulations will be compared with the data obtained using the classical approach.

By adopting this approach it was possible to understand the effect of different surface topologies, simulation methodologies and system conditions in the adsorption process. Ultimately, this investigation contributed in shedding new light on all stages regarding the adsorption mechanism at an atomistic scale, as well as in contributing to explain some experimental issues related to the CM-SH/Au conjugates, namely the polydispersity.

System characterization. The investigation started toward unveiling the structural properties of the AMPs alone. To do so, the peptides were properly neutralized in aqueous solutions and stabilized by performing an initial energy minimization followed by 30 ns of molecular dynamics. Properties such as radius of gyration and secondary structure (Fig. 3.1) were extracted from the trajectories.

This analysis allowed to conclude that none AMP presented a defined structure, with most part of the chain being either random coil or bend. This conclusion was consolidated by the evolution of the R_g with its standard deviation being more than 10 % higher than the average value (15 % for CM-SH and 12 % for CM). The R_g of a protein or a peptide, as in this case, is a measure of its compactness. If a macromolecule is stably folded, it will likely maintain a relatively steady value of R_g [205].

In addition, two simulations of 50 ns were performed, each with five peptides of each type. The objective was to understand if the peptides tend to aggregate in water and, therefore, to adsorb to the gold surface as clusters. The distance distance between pairs

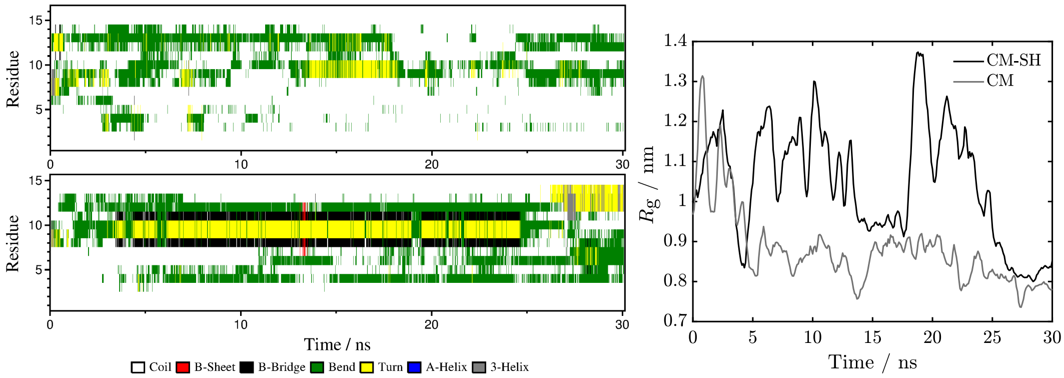

(a)

(b)

Figure 3.1: Evolution of the (a) secondary structure (CM-SH top and CM bottom) and (b) radius of gyration (R_{g}).

of AMPs was the metric used to assess if clusters were being formed (Fig. 3.2). CM-SH was the only AMP that presented some peptide interaction. This behavior is characterized by the drop of the minimum distance at the 30 ns and 40 ns timestamps (Fig. 3.2(a)). The decrease of the distance can be explained by the formation of hydrogen bounds between the AMPs (Fig. 3.2(b)), which occurs only for CM-SH. Despite these sporadic interaction, the hydrogen bounds split frequently and CM-SH AMPs were found free most of the simulation time. Therefore, one can assume that these peptides do not interact strongly with each other.

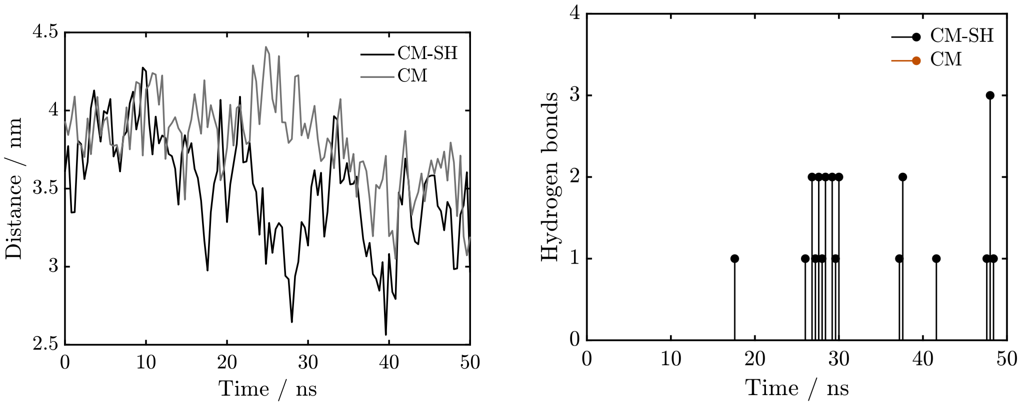

(a)

(b)

Figure 3.2: Evolution of the (a) minimum distance between all peptides pairs. Each curve was obtained of the averaging the minimum distance between all the AMP pairs for each step; (b) total number of hydrogen bounds in the system between AMPs.

In an attempt to understand how much simulation time is required to probe the complete adsorption process, both peptides were simulated in the presence of a gold surface. At this stage, only one AMP was added to the system. This was crucial to establish a baseline on how the AMPs interact with the gold without the influence of additional molecules. Sets of simulations of 50, 70 and 100 ns, values selected based in our previous experience with biological systems, were performed as initial tests. These data provided substantial information regarding these systems. It was possible to observe that the final conformation of the peptide (after the adsorption to the Au surface) was different in all simulations (Fig. 3.3(a)). This was a clear indication that some kind of sampling was required in order to properly probe all possible conformation. It was also found that 50 ns might be not enough to grasp the complete adsorption process (test for 70 ns, Fig. 3.3(b), indicated that the peptides promptly adsorbed to the surface). While in some cases the peptides migrate almost immediately to the surface (under 10 ns), in other simulations much rather time was necessary. However, it should be stressed that the adsorption rate is strongly related to the distance at which the peptide is located from the surface (in these evaluations less than 3 nm). Since in the subsequent studies the peptide was planned to be located at a distance of, at least, 3 to 3.5 nm to the surface a higher simulation time would be required. Ultimately, it was found out that 100 ns of simulation was a good compromise between towards a reliable study of the adsorption by an acceptable computational load. These preliminary considerations were very important since they shaped the way that these systems were addressed henceforward.

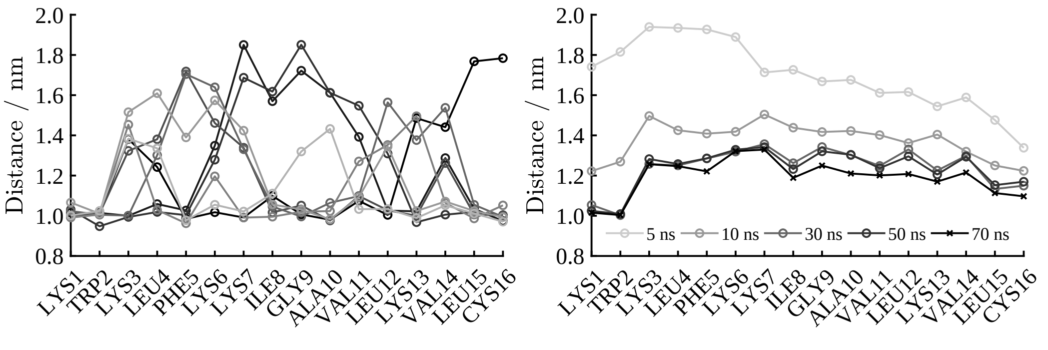

(a)

(b)

Figure 3.3: Assessment of the dynamic behavior of the CM-SH system. (a) - Distance of each residue (center of mass) to the Au slab at the end of a 70 ns simulation (each gray tone curve correspond to a different simulation); (b) - Evolution of the distance of each residue to the Au slab for multiple simulation timestamps (each curve corresponds to an average over all simulations).

3.1 Interaction with a Au slab

Modelling details. The peptides CM-SH (KWKLFKKIGAVLKVLC) and CM (KWKLFKKIGAVLKVL) were firstly relaxed for 20 ns in aqueous solution at 298.15 K. For each one, the resulting conformation was then used as the initial structure for the subsequent simulation. Twenty independent systems for each peptide were prepared and simulated for statistical relevance. Each initial peptide position relative to the Au surface was prepared by rotating the peptide backbone relative to *zz* and *yy* axes, and by locating its center of mass at a distance of ca. 3.0 nm normal to Au (hereinafter, all distances to Au surface should be considered perpendicular to the surface). This condition ensured that, at the beginning of the simulation, the peptide was outside the range of influence of Au (see discussion below). With the systems prepared, the simulations were carried out for 100 ns. All the uncertainties here reported are referred to a confidence interval of 95%.

Results and discussion. Before looking into the peptide-surface interaction in detail, mention should be made to the exact location of the nearest water layer to the surface in order to establish the boundaries of adsorption regimes. This characterization is crucial in order to understand the first stages of the interaction between peptides and Au surface (hereinafter mostly referred to as surface). In this regard, our results show that the first and the second water layers (WL1 and WL2) are located at a distance of ca. 0.29 nm and ca. 0.56 nm, respectively (see Fig. 3.4). The location of WL1 is particularly important because it establishes the cut-off which defines if a specific residue is in direct contact with the surface, i.e. the condition for the occurrence of strong adsorption[30]. In line with recent results reported by Penna et al.[39], our study reveals that the surface projects an attraction field into the solvent by ca. 0.8 nm to 1.0 nm (Fig. 3.4(b)).

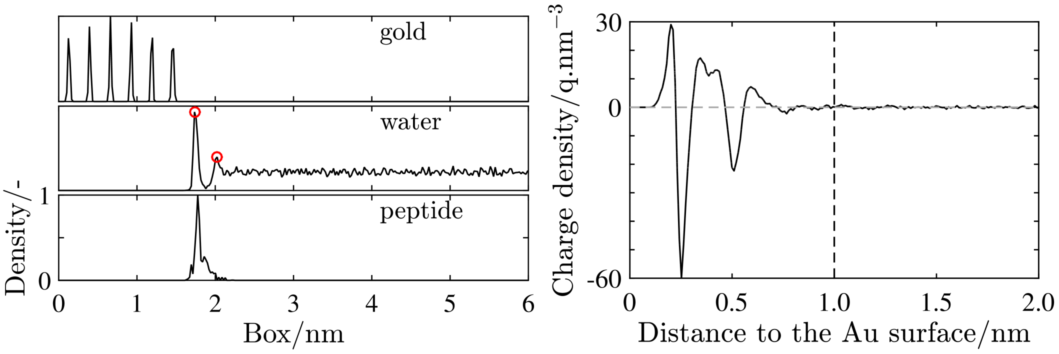

(a)

(b)

Figure 3.4: Representative (a) density profile normal to the surface (taken for the last 1 ns of simulation), in which the location of the WL are highlighted by circles; (b) charge density variation normal to the surface (calculated from the GROMACS **gmx potential** command). Dashed vertical black line at 1 nm pinpoints the end of the attraction field.

Structural features of the peptides interacting with the Au surface were firstly assessed based on the root mean square deviation (RMSD). The structures obtained from the NPT ensemble (see Sec. 2.2) were used as reference for the RMSD calculations. The time evolution values for each peptide were averaged from all the simulations (Fig. 3.5) reveal two distinct patterns over the simulation time, viz. before and after the structural lockdown

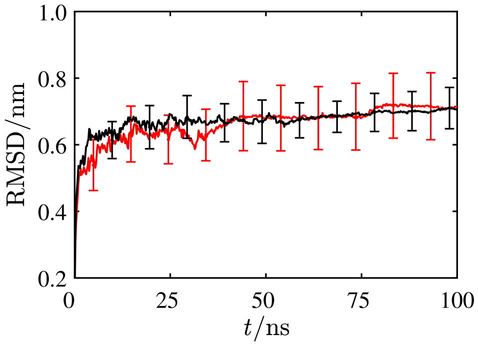

Figure 3.5: Evolution of RMSD for each peptide backbone (CM-SH black and CM red). Each curve was obtained by averaging the RMSD values from all simulations for each peptide.

of the peptide to the surface. Data for each individual simulation can be found in Fig. B.1 in Appendix B. This result also provides relevant information regarding the convergence of the system. The fact that the RMSD value tends to plateau during the later stages of simulation, is a clear sign that the simulations converged to a stabilization point.

While peptides are out of the influence of the surface, some fluctuations in RMSD are observed as a consequence of a random diffusion in the bulk water. Fig. 3.5 also evidences that RMSD for the CM-SH peptide reaches a plateau much faster than its CM counterpart (a tendency which is substantiated by the narrower uncertainty range in the case of the CM-SH specimen). These results are a first sign that CM-SH peptide is prone to faster achieve a stable conformation after the adsorption when compared to CM. This distinct behavior should be ascribed to the CYS16 residue, being a first evidence of its role in the anchoring and/or lockdown process, possibly by enhancing the stability of the complex. Nonetheless, the large confidence intervals hint that, despite achieving adsorption, the peptide locked structure is not necessarily the same for all the simulations.

For most biological systems the stabilization of the RMSD value is usually a good indicator that the systems converged, but it is also true that such a stabilization might not be a sufficient condition to ensure convergence. In fact, the concept of convergence in MD simulation is not consensual. By searching the bibliography[206–208], no definitive criteria and/or method exists. In our study, the adsorption process between interacting entities was investigated. The evaluation of distances between them provides important information regarding the stabilization of the system, specially during the latter stages of the adsorption process. Fig. 3.6 combines the information provided by the distance of the peptide to the surface and RMSD. Clearly, both metrics tend to plateau during half/three-quarters of the simulation. This is a clear sign that the simulations converged to a stabilization point.

Despite these evidences, the convergence was further investigated from a recently reported approach[209]. The method statistically investigates the RMSD matrix (a different

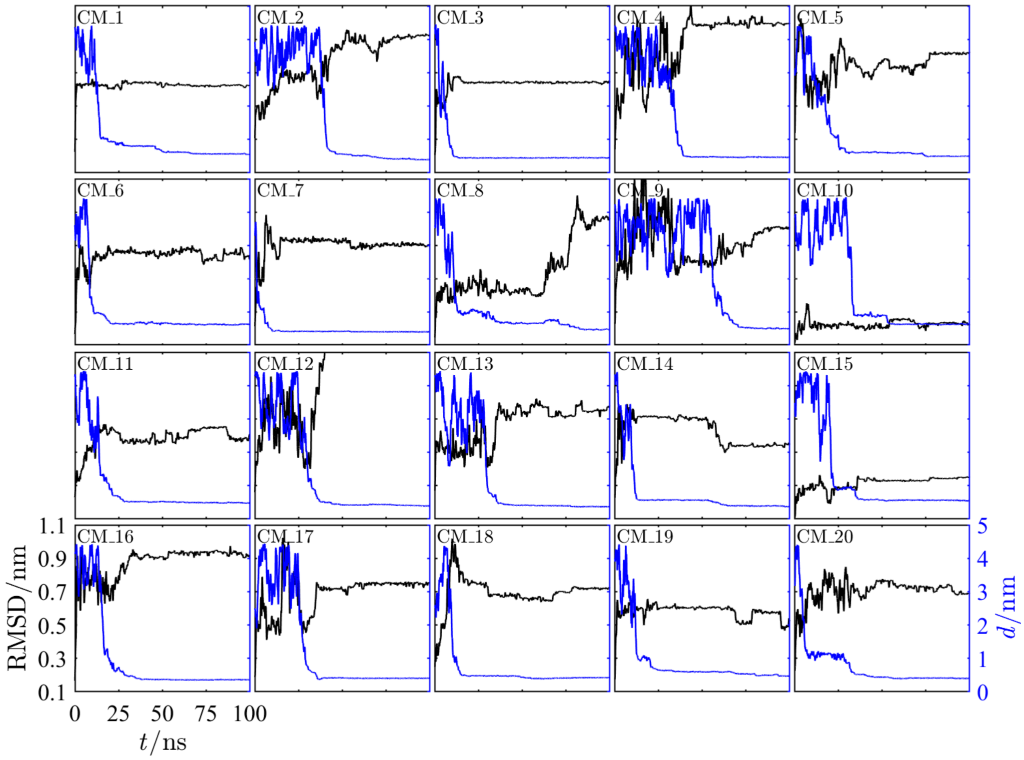

(a) CM peptide.

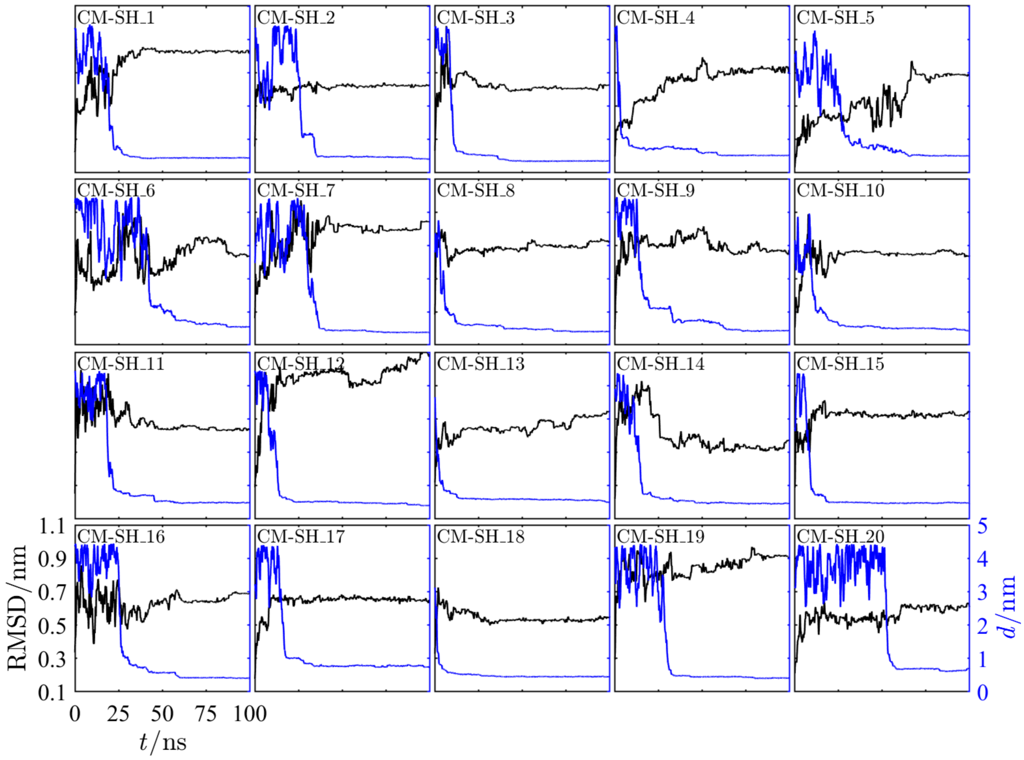

(b) CM-SH peptide.

Figure 3.6: RMSD *versus* the distance of the center of mass. Data from all simulations.

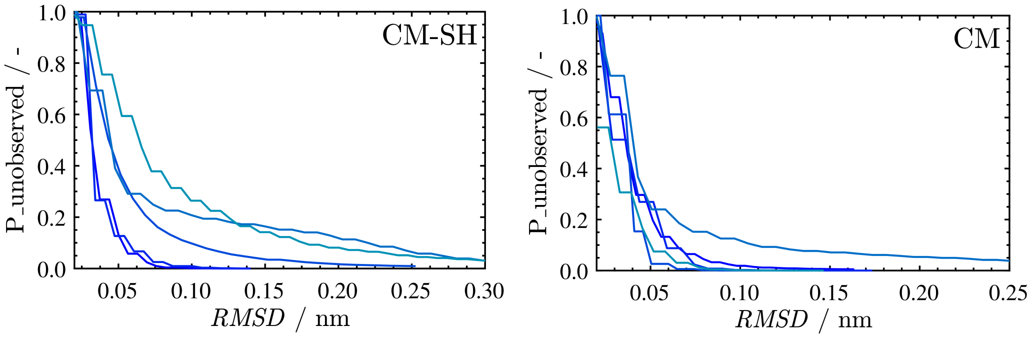

(a) CM-SH.

(b) CM.

Figure 3.7: Probability of finding a new conformation if the simulation is extended. Each curve corresponds to one independent simulation.

metric compared to the RMSD *versus* time previously discussed) and tests what is the probability that structures with RMSDs higher than a given threshold have not yet been observed in the simulation. This provides an extra layer of confidence regarding our results, ensuring that a given conformation was observed during the simulation. Since this method requires high computational power, ten randomly selected systems (five for each CM and CM-SH specimen) were tested. The results, resumed in Fig. 3.7, indicate that the probability of finding a new conformation if the simulation would be extended (beyond 100 ns), ranges from 0 to 0.05. These results, combined with the data regarding distances and RMSD fluctuation, clearly indicate that 100 ns of simulation is enough to ensure that the simulation ensemble has converged.

To support these results even more, some of the simulations were extended for 50 ns (totaling 150 ns of simulation) to verify if there were major differences in the trajectories. Fig. B.3 in Appendix B summarizes two of the systems that were extended. Again, it was not found any significant alterations in the system metrics.

The analysis of the distance of the center of mass of the peptide (CM and CM-SH) to the surface provides an overview of the evolution of the adsorption process. Fig. 3.8 gathers the outcomes of the 20 simulations for the CM-SH peptide (comparable trajectories were obtained for the CM peptide; see Fig. B.1).

Our approach was somehow more conservative with regard to the initial condition of the simulations when compared to other works[32,39]. In order to provide a stochastic element to the simulations from the very beginning, the peptides (CM-SH or CM) were located ca. 3.5 nm away from the surface, i.e. clearly out of the surface field projected into the solvent (see Fig. 3.4(b)), as well out of the specified cutoff Coulomb (1.0 nm) and Lennard-Jones (1.2 nm) interactions (see Methods and computational details). As a consequence, the peptide typically starts to randomly drift for 10 to 20 ns in the bulk solvent (which also explains the fluctuation of the RMSD at the first stages of the simulation discussed earlier;

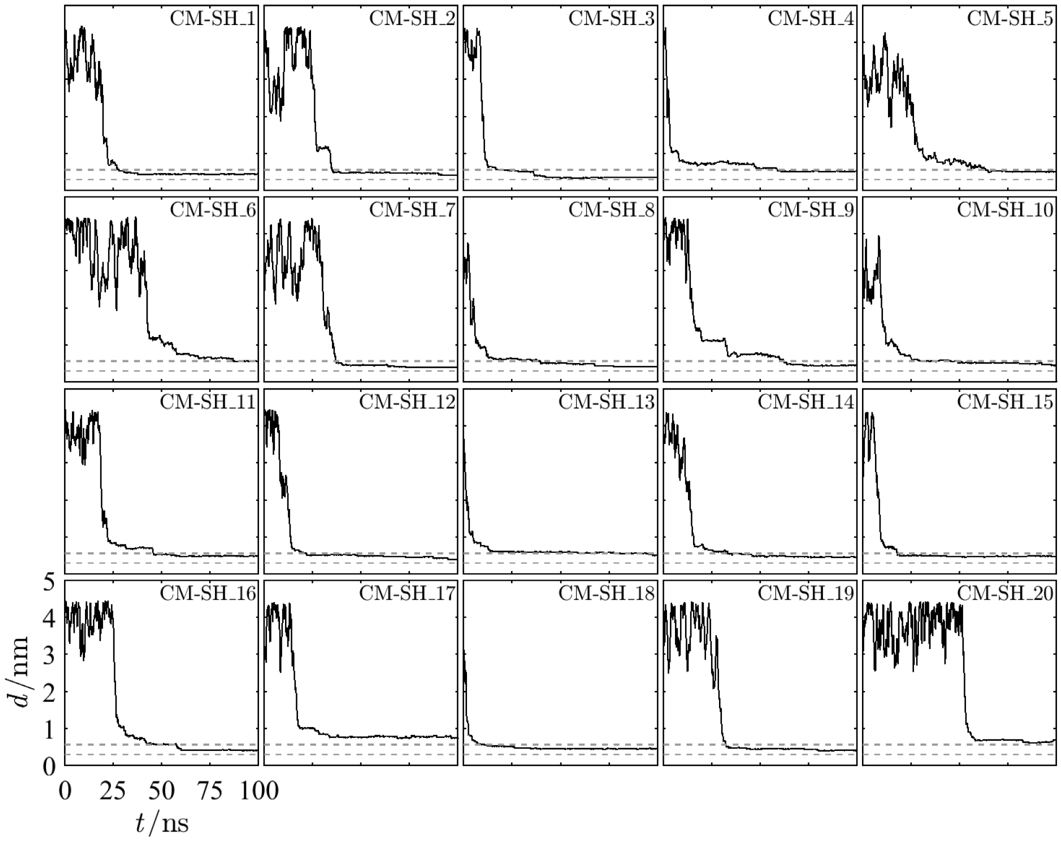

Figure 3.8: Distance of the center of mass of the CM-SH peptide to the Au surface (see Fig. B.2 for some representative snapshots of the MD runs). Each plot represents one simulation and its unique identifier is located on the top right. Gray dashed lines indicate the location of the water layers

see Fig. 3.5). Then, as the peptide gets closer to the surface, it falls within the surface attraction field and biased diffusion starts. These simulation conditions allow unambiguous definition of the starting point of the biased diffusion, for each individual simulation. In this way, it was considered that the biased diffusion follows two (necessary but not sufficient) conditions: i) it starts once the peptide approaching to the surface reaches a point of no return, i.e. a moment from which its distance to the surface is always decreasing; and ii) when at least one of its residues (center of mass) is at a distance of 1.0 nm or less to the surface (distance based on the surface attraction field; see Fig. 3.4(b)). Fig. 3.9 shows the distance of each residue to the surface for the a CM-SH system (see Fig. 3.8) as typical result (a representative system of the CM peptide can be found in Fig. B.4).

Taking the analysis of data from Fig. 3.9 as an example (of the analysis performed on the full set of results), it is observed that the biased diffusion is triggered by the LYS1 residue (first residue to be at a distance of 1.0 nm to the surface). (This instance is highlighted in the snapshot inserted in Fig. 3.9). When this happens, the residue pulls the remaining chain towards the surface, culminating in the anchoring of the peptide to the WL2. It is worth mention that this a necessary but not sufficient condition for biased

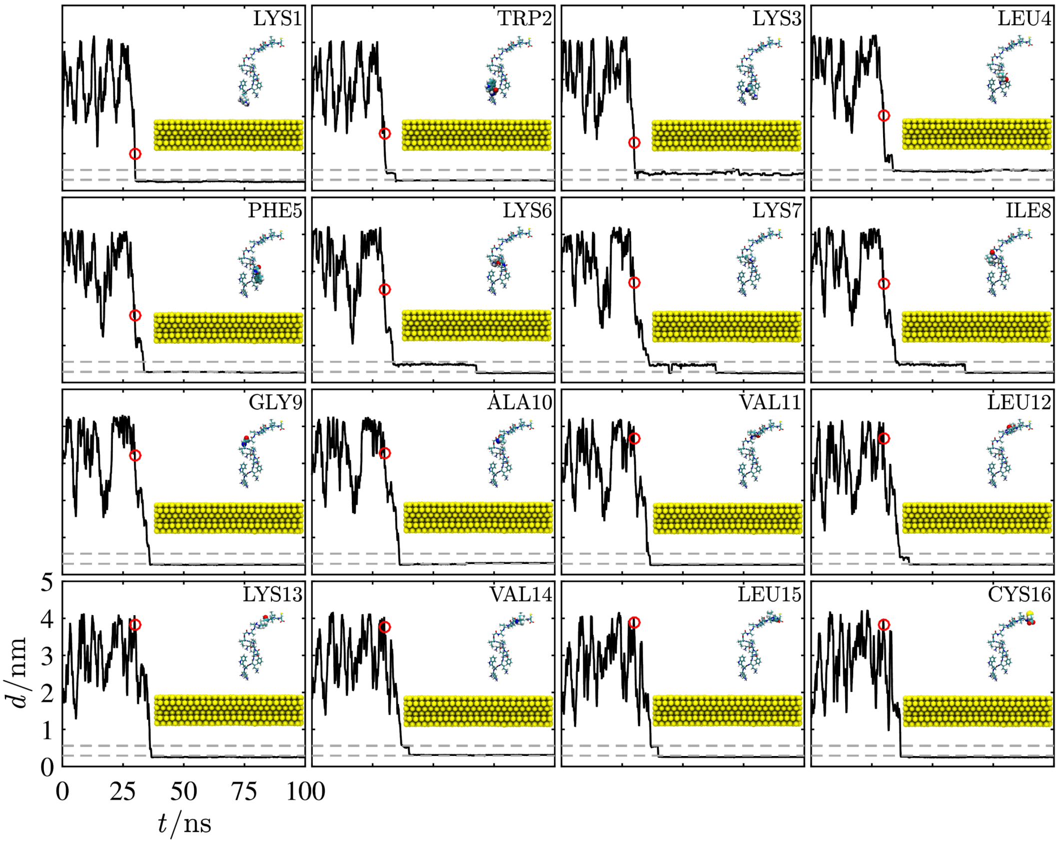

Figure 3.9: Normal distance between the closest atom of each residue to the surface for the system CM-SH_7 (representative simulation). The red circle represents the time at which the biased diffusion regime stars. Gray dashed lines indicate the location of the water layers.

diffusion and anchoring. The fact that a residue is at a distance to the surface less than ca.1 nm does not necessarily means that the peptide will start biased diffusion. This can be checked in Fig. B.4, for instance in the case of residue LYS6 (also LYS1, PHE5, LEU12 and LEU15), which reaches a distance of ca. 1 nm to the surface, at the 20 ns mark, and does not irreversibly trigger the biased diffusion. This behavior was observed in several simulations (in both peptides) by analyzing the distances of each residue to the surface. During the anchoring process, some residues detached from the WL2 (viz. LYS1 and TRP2 at ca. 34 ns in Fig. B.4) and moved back to the bulk of the solvent. This result shows that the anchoring process is reversible and that residues can occasionally detach back to the bulk solvent, as also reported by Penna et al.[39].

A thorough analysis of the peptide-surface distance profiles (Fig. 3.8 and Fig. B.5 in Appendix B) suggested that the trajectory profile from the start of the biased diffusion regime fits the behavior of an exponential decay. Thus, having evaluated the starting point of the biased diffusion for each simulation, the selected data were fitted by a exponential decay model as an approach to assess the apparent kinetics of the biased diffusion (for comparative purposes). An example of this fitting can be found in Fig. B.5.

The obtained decay constant was $(0.50 \pm 0.04)\,\mathrm{ns}^{-1}$ for CM-SH and $(0.48 \pm 0.04)\,\mathrm{ns}^{-1}$ for CM . The difference indicates that CYS essentially does not affect the rate of the biased diffusion, a result that makes sense considering the dimension of the CYS16 relative to the remaining peptide chain. This approach (exponential decay model) also permits the isolation of the time interval (within the overall 100 ns simulation time) in which the biased diffusion, anchoring and lockdown regimes take place. The starting point of the biased diffusion was already described above (it occurs when at least one of the peptide residues is at a distance of 1.0 nm or less to the surface). The end of the lockdown regime is characterized by the lock of the peptide structure at the end of the adsorption process. This translates in to a low variation of the distance of the center of mass of the peptide to the surface, and the corresponding instant was chosen by considering the point in the trajectory from which such a variation was less than 0.01 %. With this threshold, no noticeable residue adjustments are found, only some minor variations of the peptide side chain are visible, as illustrated in Fig. 3.10.

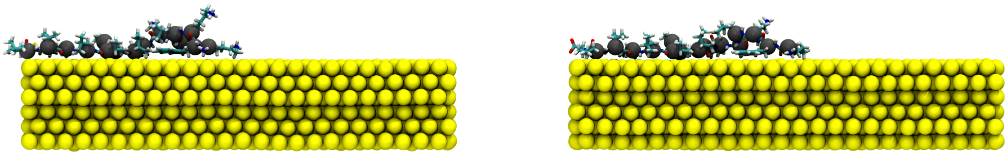

(a) (b)

Figure 3.10: Location of the α-carbon of each residue (highlighted in gray by a van der Waal's-based representation) for the system CM-SH_7 (a) at the end of the lockdown regime (variation of the distance is less than 0.01 %) and (b) at the end of the simulation.

According to this criteria, the time for the adsorption process (biased diffusion, anchoring and lockdown) was (40.61 ± 11.33) ns for CM-SH and (42.03 ± 12.40) ns for CM. The CM-SH peptide seems to go through the adsorption process marginally faster (ca. 3.4 %) than CM, but the uncertainty intervals do not allow definitive conclusions to be drawn. The diffusion coefficients for both peptides were calculated (from the GROMACS command **gmx msd**) for all the simulations. The calculations were limited to the biased diffusion regime. Thus, the interval of simulation selected to perform the fitting was from the start of the biased diffusion to the occurrence of the first anchoring point. The obtained coefficients, $(5.28 \pm 0.76) \times 10^{-7}\ \mathrm{cm}^2\,\mathrm{s}^{-1}$ for CM-SH and $(4.24 \pm 1.08) \times 10^{-7}\ \mathrm{cm}^2\,\mathrm{s}^{-1}$ for CM, also suggest that the CM-SH diffuses slightly faster. However, considering again the uncertainty intervals, definitive conclusions cannot be drawn. This indicates that the CYS residue has marginally no effect in the diffusion process.

Downscaling the trajectory analysis toward an atomistic detail aiming at understanding the effect of each residue during the adsorption process with higher resolution, the distance of the closest atom within each residue to the surface was analyzed. With this purpose, a residue was considered adsorbed to the surface if it had an atom at a distance to the surface equal or less than 0.29 nm (location of WL1). Fig. 3.11 summarizes the adsorption map for all the simulations for the CM-SH peptide (data for CM can be found in Fig. B.6).

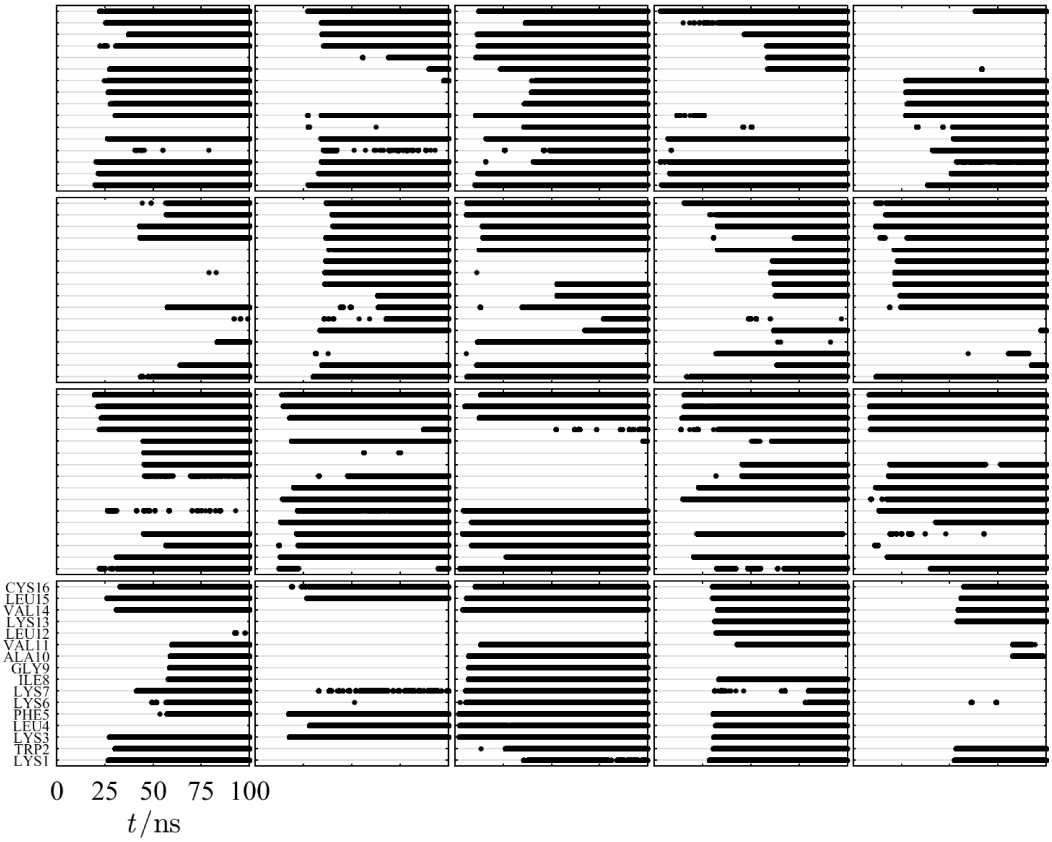

Figure 3.11: Residue adsorption map for the 20 simulations on CM-SH/Au interaction. Thick black line indicates that the residue is adsorbed. (Each plot corresponds to one simulation.)

A first glance, Fig. 3.11 reveals the variability in the set of simulations. Clearly, the peptide approaches to the surface in different ways depending on its conformational history. Then, due the strong metal-peptide interaction, it anchors and locks to its final conformation within a relatively short time interval. The way the peptide approaches the surface will determine its final conformation, and, despite the already mentioned variability in this event, a large portion of the peptide is adsorbed to the surface by the end of the simulation [(74.00 ± 7.90)% of the chain for CM and (70.31 ± 7.40)% for CM-SH].

Several trends in the peptide residues, as well as in their moieties, are identifiable during the adsorption process. With few exceptions, the N-terminus exhibits a tendency for being adsorbed in most of the simulations (see Fig. 3.11 for CM-SH and Fig. B.6 for CM). On the other hand, the larger time interval required for the adsorption of the C-terminus reported by some authors[32,39], appears here to be attenuated by the presence of cysteine. Comparing the averaged distances of VAL14 and LEU15, these residues take about 70 ns to achieve a stable conformation in CM against only ca. 55 ns in CM-SH (see Fig. 3.12).

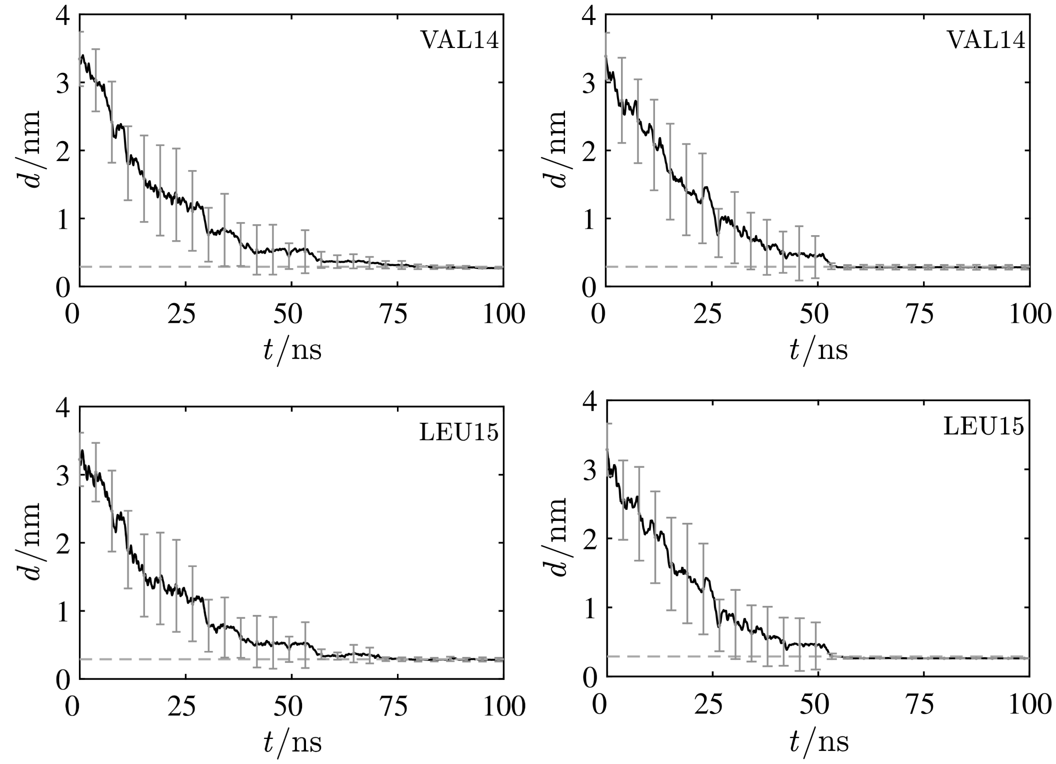

(a) CM

(b) CM-SH

Figure 3.12: Averaged time evolution of distance of the closest atom of the residue to the surface (dashed gray line corresponds to the location WL1).

Our MD simulations also predict a clear trend of CYS16 (the terminal residue of CM-SH peptide) to remain very close to the surface. This behavior agrees with quantum chemistry (DFT) studies[144] reporting the tendency of thiols to bind covalently to Au metal surfaces. Indeed, the presence of CYS appears to be a key factor in the adsorption process, also contributing to strengthen the adsorption of the terminal residues. This analysis allows us to postulate that the CM-SH peptide is much more readily stabilized over Au when compared to the CM specimen.

In both CM-SH and CM cases the residues LYS1, TRP2 and LYS3 at the N-terminus appear less susceptible to be adsorbed to the surface (Fig. B.7). This is a very interesting feature considering that these first residues are determinant in the antimicrobial activity of the peptides[76], being in line with experimental data showing that CM-SH/AuNPs conjugates retain the antimicrobial activity[1]. Also, the residues of the central segment of the peptide (LEU4 to LEU12) are frequently found not adsorbed, indicating that the adsorption occurs preferentially through the N-terminal and C-terminal.

As a complement to the previously discussed trajectory analysis, the percentage of occurrences of atoms at an adsorption distance ($\leq 0.29\,\text{nm}$) to the surface during all the simulations for the CM-SH peptide was calculated. The results for the CM-SH peptide are summarized in Fig. 3.13 (results similar to CM Fig. B.8). This analysis shows that most of the occurrences are related to the proton bound to the α-carbon. This applies to almost all residues, the LYS, LEU4 (proton of the carbon where isobutyl branches) and PHE5 (methylene proton adjacent to the aromatic ring) being the exceptions. For LYS the adsorption location is consistently the proton of the methylene (ε-carbon) adjacent to the NH_3^+ in the side chain (which is adjacent to an alkyl chain). The adsorption points in the three mentioned exceptions are characterized by a region of hydrophobicity. Since there is a location without water molecules between the Au surface and the WL1 due to the layering of water molecules (Fig. 3.4(a)), this region favours the accommodation hydrophobic moieties of the peptide. The high number of contact occurrences for the CYS16 residue when compared to the remaining chain corroborates the previously discussed data, consistently demonstrating that the CYS16 plays an crucial role in the adsorption process, and with all probability, in the conjugate formation It should be stressed here that it was not found any particular kind of order or orientation of the water molecules forming the water layers after the adsorption process

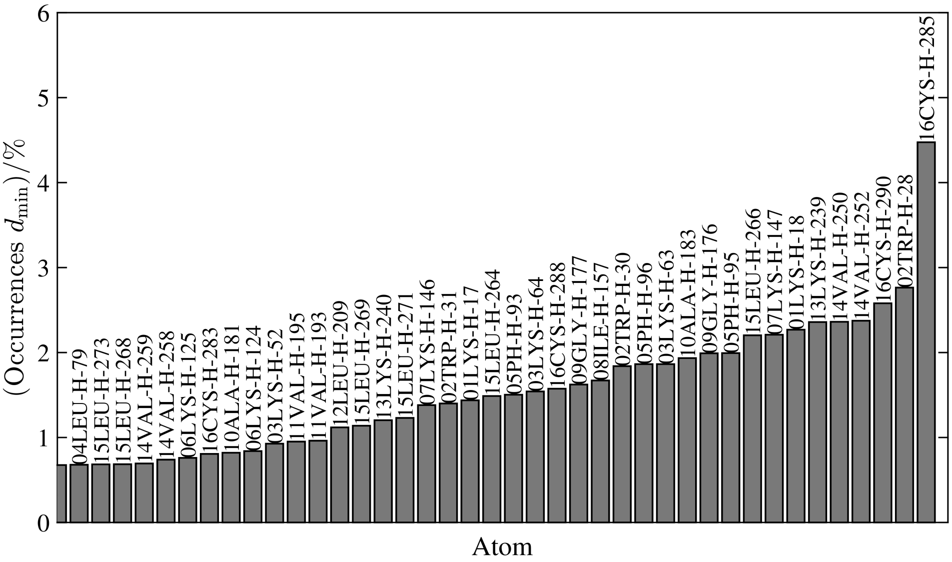

Figure 3.13: Percentage of occurrences of atom at an adsorption distance ($\leq 0.29\,\text{nm}$) to the surface during all the simulation for the CM-SH peptide. (The less populated cases are omitted for simplicity. Atom numbering can be found in the list B.1 in Appendix B.)

It is worth mentioning that our MD results help in rationalizing experimental evidence for the contribution of CM-SH in the formation of AuNPs with low size and polydispersity in remarkable contrast with AuNPs under the influence of the CM peptide[1]. The computed results confirm that CYS plays an important role during the later stages of the adsorption process characterized by its systematic strong interaction (possibility by chemical bounding) with the surface. Such a bridge between experimental and calculated data is in line with the statement that "lower stabilities are less likely to slow particle growth in real time, resulting in aggregation of AuNPs", whereas "strong binding of peptides limits or slows the Au NP from further growth"[31]. Moreover, the experimental results demonstrate that the peptide activity is retained after being supported in the AuNP. This was also suggested by the MD results, according to which the key residues with antimicrobial activity are less prone to adsorption.

3.2 Interaction with a AuNP

Modelling details. The effect of AMP concentration into the adsorption mechanism was assessed by considering a set of systems prepared with more than one AMP. Overall, a total of two systems formed by one AuNP and five APMs of each kind was built. The peptides were inserted randomly in the system resorting to the **gmx insert** command, ensuring however that they were at a distance of around 2.5 nm of the AuNP. To understand how many peptides can adsorb to the 6 nm AuNP, 200 ns simulation of a system with 70 peptides and AuNP was performed. The number of peptides bound onto the surface of AuNP was estimated at the end of the simulation.

Results and discussion. We started by performing some quick tests with AuNP of 2, 4 and 6 nm of diameter. The diffusion profiles were found to be very similar regardless of the NP diameter (results can be found in Fig B.9 in Appendix B). It should be mentioned that this outcome contrasts with what was found by Yu et al.[31,32] (the AuNP diameter affected the conjugate stability). The difference can be attributed to the distinct AMP dimension (CM-SH is ca. 33% larger than A3) and to the presence of CYS in our AMP. Therefore, we ended up using the 6 nm AuNP since it was closest to the diameter of the AuNP reported in the experimental work[1]. An initial set of 10 simulations were performed for the interaction of the CM-SH peptide with a 6 nm AuNP. The evolution of the distance of the peptides to the AuNP can be found in Fig. 3.14.

The trajectories summarized in Fig. 3.14(a) indicate that the terminal cationic residues of CM-SH (LYS1 and LYS3 at the N-terminus), an important component in antimicrobial activity of the peptide, appeared to be less prone to adsorption to the surface. Our simulation results also showed that PHE5 is important for the peptide anchoring process. This attribute has been reported previously[30–32], and is explained by the fact that the aromatic ring fits the fcc lattice structure of the Au surface. MD simulation predicted a clear tendency of CYS16 (the terminal residue of CM-SH peptide) to remain very close to the Au surface (below 0.3 nm), and this configuration is thus a key factor in the binding process (Fig. 3.14(b)).

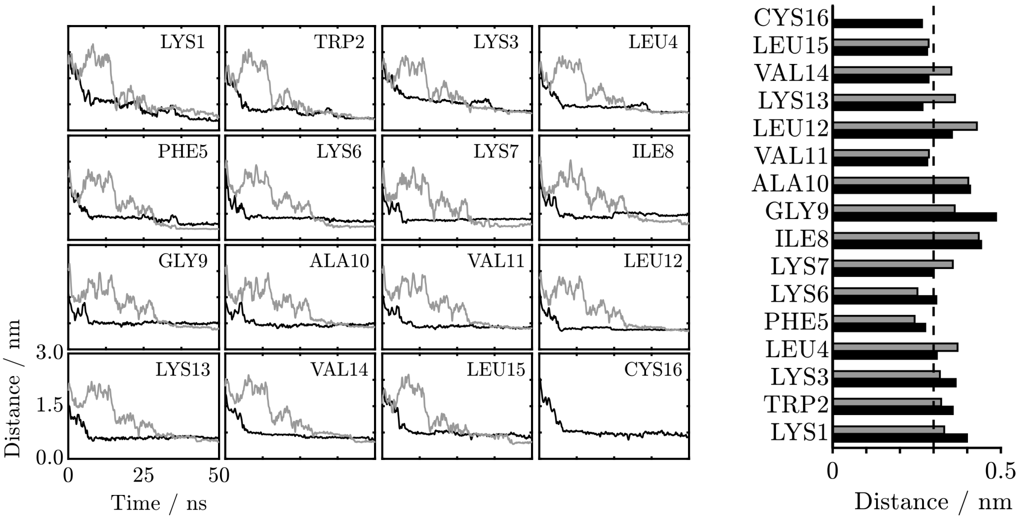

(a)

(b)

Figure 3.14: (a) Averaged MD trajectories for the interaction of five CM-SH (black) and five CM peptides (gray) with an AuNP. (b) Distance of the residues to the Au surface at the end of the simulation. The line at 0.3 nm represents the cut-off used to define direct contact between the atoms of the amino acids and the Au surface.

With regard to the RMSD of the peptides, it was found that the CM-SH peptide hits a plateau at around 35 ns of simulation while CM still presents some variation, results are summarized in Fig. 3.15. In fact, when comparing the RMSD and residue distance to the Au surface profiles to those obtained for the Au Slab (Fig. 3.6), clear similarities are found. This indicates that no substantial differences are found between the surface topologies (NP vs. Slab), at least at the diffusion level. The same can be said for the AMP concentration. This was, however, somewhat expected due to lack of strong interaction between the AMPs. With that said, this can change in the case of AMP supersaturation, in which different phenomena my govern the adsorption process.

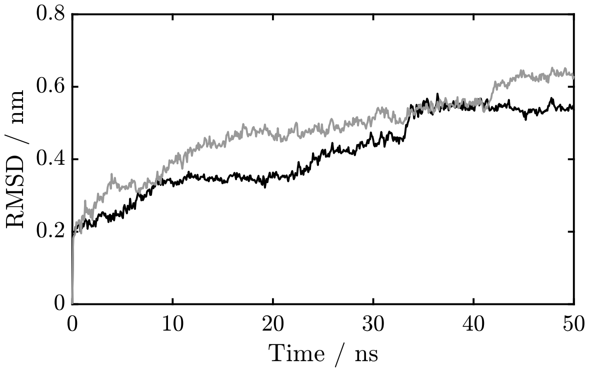

Figure 3.15: Averaged RMSD for the cecripin peptides (CM-SH in black, CM in gray). Starting conformation used as reference.

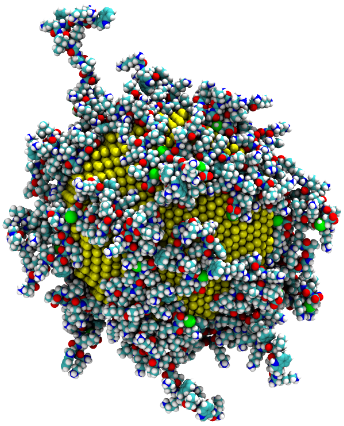

Figure 3.16: Formed CM-SH/AuNP conjugate at the end of 200 ns MD simulation.

Next, a system with 70 CM-SH peptides and one AuNP was simulated. With the data of this simulation it was intended to estimate how many peptides the AuNP could accommodate (in optimal conditions). From the 70 initial peptides, 42 ended up binding to the surface (snapshot of the CM-SH/AuNP conjugate Fig. 3.16).

With the data obtained from this simulation, we were able to estimate that a 14 nm AuNP (similar to the ones used by Rai et al.[1]) would be able to capture ~230 CM-SH peptides. In fact, this result is quite similar to the one obtained by the authors, ~237 CM-SH per AuNP. This indicates that the CM-SH/AuNP conjugate obtained by Rai et al. is near, or already, saturated by peptides.

3.3 Metadynamics approach

Modelling details. The AMPs were inserted in the simulation box with its center of mass at a distance of ca. 6.0 nm normal to Au. Next, two well-tempered metadynamics[183] runs under aqueous conditions were performed in the presence of the Au surface – with CM-SH and CM – for 500 ns. The peptide radius of gyration (R_g) and distance of the center of mass (COM) of the peptide to the COM of the AuNP (d_{COM}) were chosen as collective variables (CVs). For the system without AuNP, the R_g was the only CV used. The widths of the Gaussian function were set to 0.1 nm for the R_g, and 0.2 nm for d_{COM}. The height of the Gaussian functions was set to 1 kJ mol^{-1}, and the bias potential was updated every 5 ps throughout the simulation. The temperature was set to 298.15 K with a bias factor of 10 K.

Results and discussion. The use of well-tempered metadynamics allows to efficiently probe the free energy (FE) of the system during the adsorption process. Since we are investigating an adsorption process, the vartion of the FE with the d_{COM} allow us to understand if the peptide is preferable free or adsorbed, while the R_g allow us to infer how the peptide is folded or elongated. This is the rationale underlying the choice of d_{COM} and R_{g} as CVs.

Looking at the FES of both peptides (Fig. 3.17), some fundamental differences are noticed. The most obvious is the fact that the region with the lowest FE is smaller, and narrower for d_{COM} in the case of CM-SH. The region with the lowest FE for CM occurs between 3 nm and 1 nm for the d_{COM}, while for CM-SH it is between 2 nm and 1 nm. This indicates that the CM-SH peptide tends to be closer to the gold slab. Putting these results side by side with those obtained through the approach using to multiple simulations (Section 3.2), it can be concluded methods produced a similar outcome.

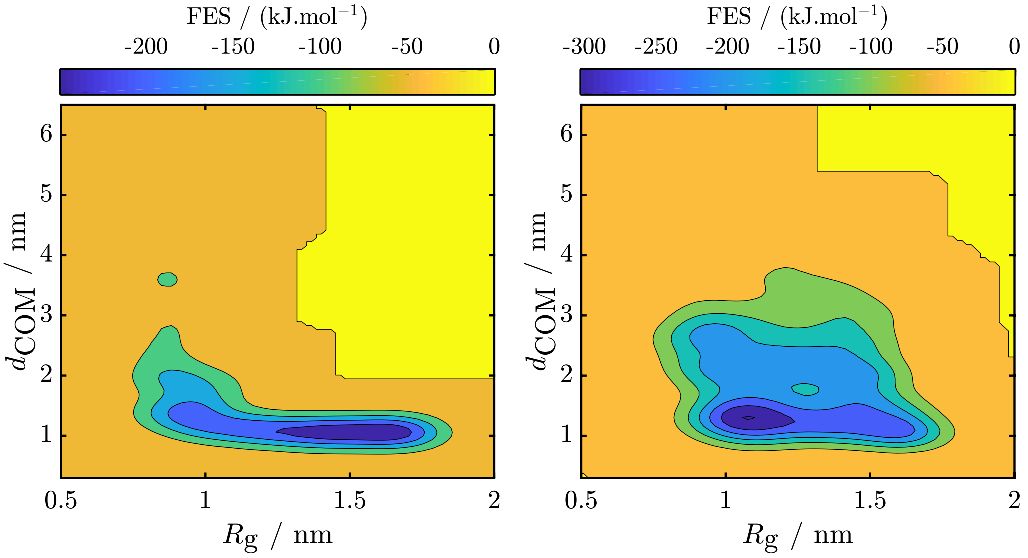

Figure 3.17: FES of the system taking in account both CVs for CM-SH (left) and CM (right).

For the R_{g} CV, the difference between the peptides is also clear. The CM-SH presents a higher R_{g} value for the global minima, which indicates that this peptide tends to be more elongated. The calculated values for the FES global minima are 251.2 kJ mol^{-1}(R_{g} 1.59 nm and d_{COM} 1.07 nm) for CM-SH and 304.2 kJ mol^{-1}for (R_{g} 1.07 nm and d_{COM} 1.28 nm) CM.

3.4 Conclusions

The preliminary simulations with a Au slab permitted rationalize the computational strategy. The data from these simulations clarified that none of the peptides have a clear secondary structure at pH 7. Additionally, it was found that the AMPs migrate quickly to the Au surface. However, no clear pattern of adsorption was found, with the AMPs having different conformations at the end.

Thorough analysis of data obtained from 40 independent simulations here reported provided new information that helps to rationalize the adsorption process of both CM-SH and CM peptides onto a gold surface. Due to the nature of the system (strong peptide/metal interaction), the way the peptides (CM and CM-SH) approach the surface determines how the adsorption process occurs. The dynamic behavior of the adsorption process of CM-SH and CM is consistent with the generic adsorption mechanism described by other authors. Our study was extended to a random diffusion in the bulk water, unbiased diffusion, that precedes biased diffusion, showing that the transition from the random to the biased diffusion is triggered by the projected attraction field into the solvent by the gold surface. It was shown that the presence of CYS has essentially no effect during the biased diffusion regime, characterized by similar diffusion coefficients in both the peptides. Regarding the later stages of the adsorption mechanism it was found that protons bound to α-carbons present the highest number of contacts to the gold surface ($\leq 0.29\,\text{nm}$) during the simulations. This indicates that, whenever possible, the adsorption occurs by means of the α-carbon moiety. Our results also clearly suggest that the antimicrobial activity is retained after the adsorption process because the residues with antimicrobial activity are less prone to be adsorbed.

It was demonstrated that the presence of cysteine at the C-terminus plays a stabilization role on the later stages of the adsorption process. The CYS residue promotes a quicker stabilization of the CM-SH peptide than its CM counterpart without significantly affecting the diffusion regime. Unlike the other residues, CYS was found consistently interacting closely with the surface, displaying negligible occurrences of detachment back to the solvent. It was also possible to observe a stabilization of the residues near the C-terminus (VAL14 and LEU15) for the CM-SH when compared to the same residues for the CM peptide. This strong CYS/Au interaction can be postulated as the reason underlying the formation of low size and polydispersity resulting from the preparation of AuNPs with CM-SH compared to the corresponding conjugate based on CM.

Negligible differences were identified for the three AuNP diameters tested (2 nm, 4 nm and 6 nm). Therefore, the AuNP with the dimension closest to the materials characterized experimentally by Rai et al.[1], in this case 6 nm, was the selected one. The different surface topologies tested, slab vs. NP, seem not to substantially affect the adsorption process or the final structure of the AMPs. Nonetheless, some differences were found.

The lower distance between the entities (AMP and Au surface) at the beginning of the simulation (2.5 nm for the AuNP vs. 3.5 nm for the Slab) led to the absence of the unbiased diffusion step for the systems with the AuNP. The remaining diffusion steps presented a similar profile for both topologies, in which, the obtained conjugates were characterized by a C-terminal section mostly in direct contact with the surface, with the CYS16 residue consistently in direct contact in all simulations (NP or Slab). The only difference worth notice is the PHE5 residue presented higher affinity to AuNP. Due to the AuNP curvature, its surface is rougher than the slab, this can lead to the formation of preferential spots of adsorption for the PHE5.

Finally, the results obtained with the metadynamics simulations were consistent with the data gathered using the other approaches – independent and concentrated system –. By using the R_{g} and d_{COM} as CVs, it was possible to map the FES for each peptide and understand how they impact the system. With the FES it was possible the identify that both global minima can be found for a low d_{COM}, with the CM-SH FES showing a clear profile of low FE near the surface while for the CM the low FE region spreads slightly for higher d_{COM} values. For the R_{g} the results were substantially different, 0.52 nm higher for CM-SH, meaning that CM-SH is preferably unfolded after the adsorption. These observations are consistent with the results obtained using different simulation techniques, indicating that data obtained using the classical approach is, in fact, has statistical significance. Nonetheless, metadynamics presents a more sophisticated platform to perform these types of simulations, with the advantage of the characterization of the FES of the system in function of the selected CV.

4. Cathelicidin-derived LL37 AMP

LL37 is the only cathelicidin-derived antimicrobial peptide found in humans. It is formed by 37 residues, has amphiphilic behavior, in some cases displays α-helical structure, and, most importantly, has been shown to exhibit a broad spectrum of antimicrobial activity [79,80]. LL37 acts as first line of defense against bacteria, virus and fungi [81]. The wound healing potential of free and immobilized (LL37/AuNP) LL37 has been investigated recently [2,210]. The results showed that LL37/AuNP conjugate have enhanced pro-regenerative properties when compared to the soluble LL37. The dynamics behind the formation and stability of this conjugate, however, is yet to be further explored. Details on how the peptide is adsorbed onto the surface and if the final structure is stable are issues not well-known. Large peptides and, *a fortiori*, proteins, are characterized by multiple local minima which are separated by high-energy barriers which results in a coarse energy landscape [40–43]. Advanced sampling methods, such as metadynamics [159], are required to properly address the conformation variability inherent to these molecular systems.

Considering the potential of the LL37/AuNP conjugate, we hereby present a computational study on the interaction of a LL37 AMP with a AuNP, in which the investigated AMP is modified with cysteine (CYS) at the C-terminal to favor its interaction with the Au surface. Similar to what was done for the CM AMP (Chap. 3), initial assessments of the AMPs alone in water and with a AuNP were performed. Furthermore, the possibility of inter and intra molecular interactions were assessed by including several AMPs in the physical model. These initial tests were undertaken using the conventional MD approach. The outcome of this study provided crucial data regarding the LL37 structure and dynamic behavior with the AuNP.

In looking towards a complete picture of the dynamics of the target AMP, four scenarios were tested: the interaction of i) plain (LL37) and ii) CYS-modified (LL37-SH) AMPs with a 4.2 nm face-centered-cubic (fcc) lattice AuNP; and reference systems consisting in iii) LL37-SH and iv) LL37, both alone in water. A set of all-atom well-tempered metadynamics simulations were performed for the four independent systems in order to sample the free energy barriers associated with the adsorption process of the LL37-SH onto the AuNP. This study also provides original quantitative information in terms of free-energy on the immobilization of the AMP (LL37-SH) onto a AuNP. These computational results contributed to rationalize some of the experimental findings reported recently [2].

Finally, the effect of these materials – i.e. both AMPs and AuNP alone, and their conjugates – with a bilayer composed by phospholipid analogous to a keratinocyte cell was investigated. It should be stressed that considering the dimension and complexity of the LL37-SH/AuNP conjugate, the simulation of its interaction with a bilayer is a daunting task. The main challenge is the dimension of the system, formed by more than 500000 particles, and the simulation time required to replicate the dynamics of this type of phenomena, multiple hundreds of nanoseconds. This challenge was tackled by preparing a framework of simulations that allowed a first understanding of each meterial in connection to the bilayer. The simulated systems were the following: i) water + bilayer; ii) water + bilayer + LL37-SH; iii) water + bilayer + AuNP; iv) water + bilayer + LL37-SH/AuNP.

System characterization. The LL37-SH peptide was firstly relaxed in aqueous solution 50 ns at 323.15 K, and then at 298.15 K for more 50 ns. The resulting conformation was then used as the initial structure for the subsequent simulations. A total of 20 peptide positions relative to the AuNP, located at a distance of 2 nm to the surface, were prepared by rotating the backbone and then simulated for 150 ns. The obtained results are summarized inf Fig. 4.1.

The simulations show that most of the residues take ca. 50 ns to be in direct contact with the surface (Fig. 4.1(a)). However, the C-terminal and their adjacent residues exhibit a faster diffusing process, ranging from 25 to 30 ns. These residues rapidly adopt a stationary, possibly strong, adsorption to Au surface, as indicated by the constant distance to the AuNP surface until the end of the simulation (Fig. C.1). The radius of gyration (R_g) profile[205] also suggests that the peptide conformation changes during initial stages and ends up adopting a more compact structure after adsorption (see Fig. 4.1(b)). The observed initial fluctuation of both parameters (R_g and distance) up to 45 ns corresponds to the diffusing process, followed by the initial stages of the anchoring of the peptide to the AuNP. Afterwards, a sharp decrease on the fluctuation of those variables, around 50 ns, and a stationary regime, which characterizes the adsorption stage, is reached. These results clearly suggest that a stable complex is formed, thus hampering the detachment of the peptide from the surface. The possible formation of a secondary structure of the immobilized peptide was also investigated (Fig. 4.1(c)). Despite some few sections indicating the presence of alpha-helix along the simulation time, no clear clues on the formation of secondary structure after the adsorption to the surface are found (Fig. 4.1(c)).

With this initial assessment no substantial differences were found in terms of adsorption profile when compared with the CM-SH peptide. Nonetheless, one can anticipate that the FES profile for the LL37-SH might be more complex when compared with CM-SH. This prediction is based on the difference in size between the AMPs (LL37-SH 675 atoms vs. CM-SH 293 atoms), which translates in more points of contact between LL37-SH and the AuNP. Consequently, the simulation time was increased to 150 ns to fully probe the adsorption process. Furthermore, for these reasons (1. potential rough FES landscape and 2. higher simulation times required), metadynamics was used to study this system in deeper detail.

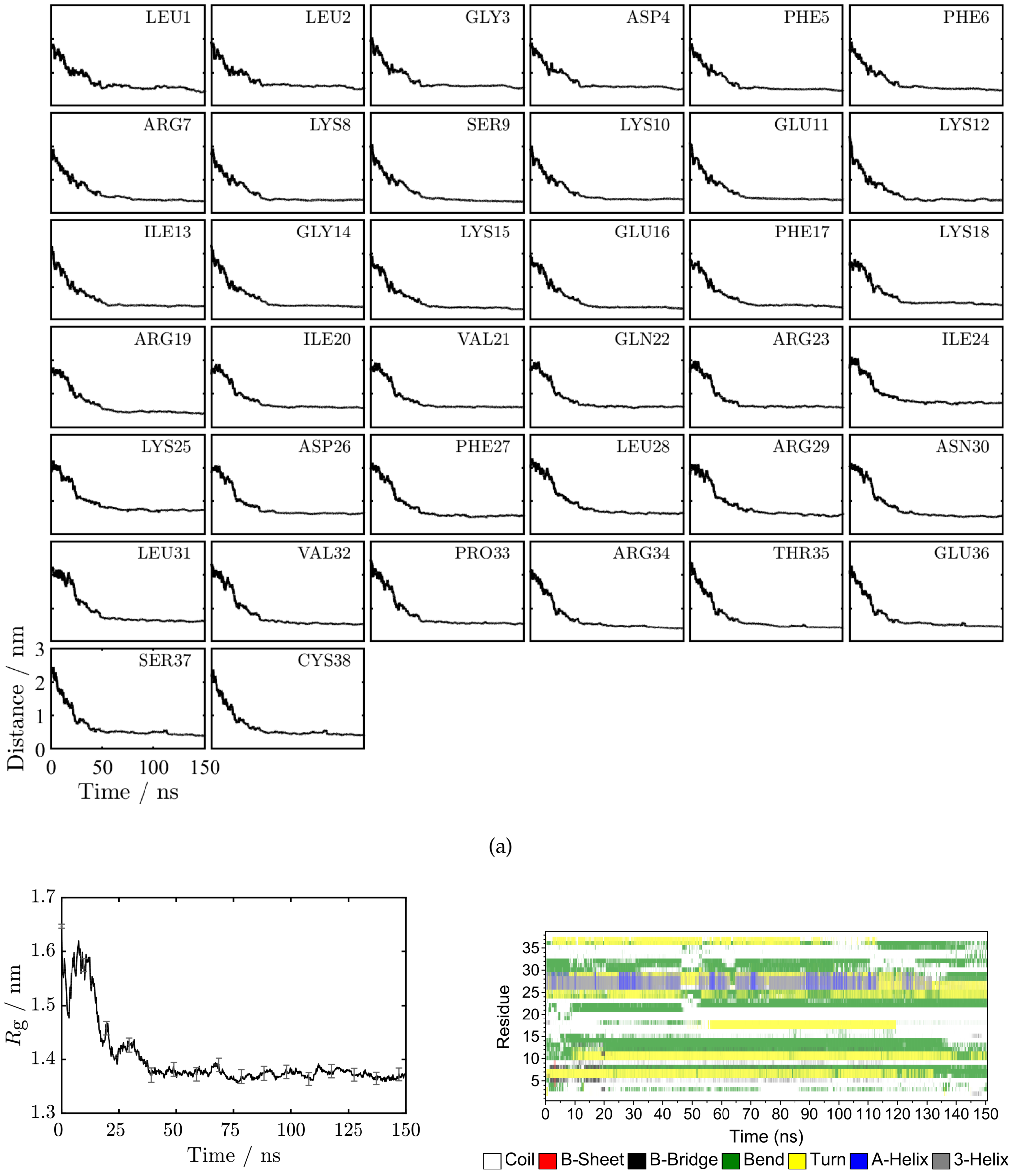

(a)

(b)

(c)

Figure 4.1: Time evolution of (a) averaged distances between each residue and AuNP; (b) R_g of the peptide backbone; (c) secondary structure.

4.1 Interaction with a AuNP

Modelling details. Four well-tempered metadynamics[183] runs under aqueous conditions were performed for both LL37-SH (LLGDFFRKSKEKIGKEFKRIVQRIKDFLRNLVP-RTESC) and LL37 (LLGDFFRKSKEKIGKEFKRIVQRIKDFLRNLVPRTES) specimens: two in presence of the AuNP and two in absence of the AuNP, the latter to be used as reference. The AMPs were firstly relaxed in aqueous solution for 50 ns at 323.15 K, and then at 298.15 K for further 50 ns. The resulting conformations were afterwards used as the initial structures for the subsequent simulations. All systems were pre-equilibrated using energy minimization simulations. The box volume was relaxed for 100 ps in NpT ensemble under periodic boundary conditions. A box of 1500 nm^3 (10 nm in xy and 15 nm in z) was prepared with the LL37-SH and a 4.2 nm diameter AuNP. For each system, well-tempered metadynamics was performed for 500 ns. Peptide radius of gyration (R_g) and peptide center of mass (COM) distance to the AuNP COM (d_{COM}) were chosen as collective variables (CVs), whereas for system without AuNP the R_g was the only CV used. The widths of the Gaussian function were set to 0.1 nm for the (R_g) and 0.2 nm for d_{COM}. The height of the Gaussian functions was set to 1 kJ mol^{-1}and the bias potential was updated every 5 ps throughout the simulation. The temperature was set to 298.15 K with a bias factor of 10 K.

For the trajectory analysis the following GROMACS and PLUMED tools were used: **gmx covar** and **gmx anaeig** for conformational entropy calculations; **gmx sasa** for solvent accessible surface area calculations; **sum_hills** to sum the Gaussians deposited during the simulation in the HILLS file; **REWEIGHT_BIAS**, **HISTOGRAM** and **CONVERT_TO_FES** algorithms[184] were used to reweight the FE energy profiles (similar approach is detailed by Klug et al.[211]).

Results and discussion. The LL37-SH/AuNP conjugate is a system whose therapeutic activity for the enhanced wound healing was recently reported by Comune et al.[2]. The authors demonstrated the improved activity of LL37-SH/AuNP conjugate compared to that of the soluble LL37-SH peptide, in consequence of a prolonged activation of EGFR in keratinocytes. An increase of the skin wound healing activity in an acute wound model was also reported for the LL37-SH/AuNP conjugate. For these reasons, the LL37-SH/AuNP conjugate is the main focus of the current discussion. Nevertheless, from a fundamental point of view, a complete analysis should also include the relevant parts of the system. Thus, results of the LL37/AuNP conjugate and LL37-SH and LL37 alone, will also be mentioned and discussed when appropriate. The analysis is based on four selected metrics: minimum distance between the centers of mass of peptides and AuNP, d_{COM}; radius of gyration R_g; end-to-end distance, $d_{End\text{-}End}$; and RMSD of the peptide backbones (the initial structure was used as reference). The discussion is organized as follows: 1) structural-related analysis; 2) free energy and entropy analysis; 3) LL37-SH bioactivity assessment.

Structural analysis

The profiles in Figure 4.2(a) show that both LL37-SH and LL37 peptides migrate to the gold surface within the first 20 ns. Overall, the peptides exhibit a typical three-stage behavior already reported in other studies[3,32,39]. In the case of LL37-SH, the first stage, corresponding to the diffusion of the peptide, is characterized by the approximation of

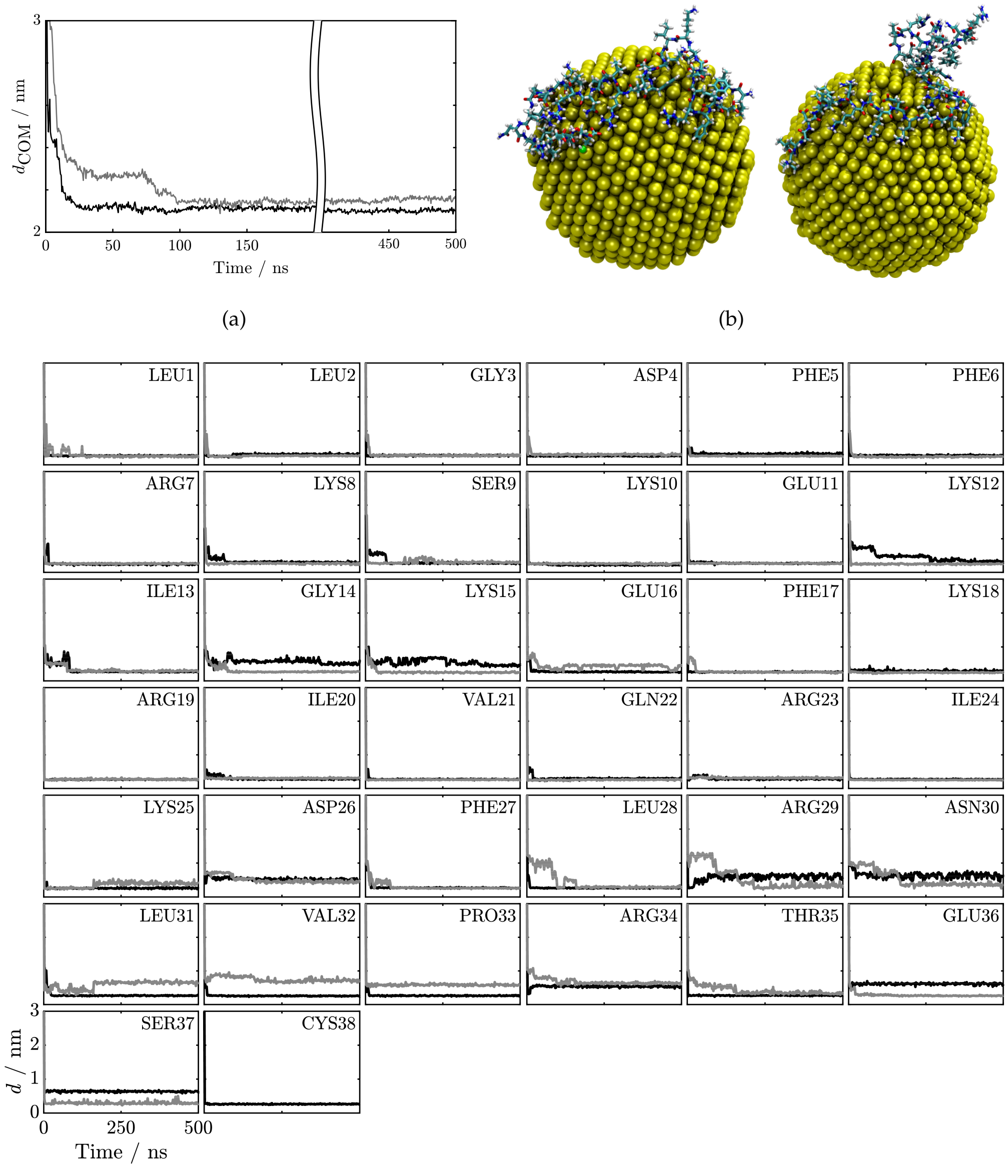

(a)

(b)

(c)

Figure 4.2: Time evolution of (a) distance between the centers of mass of peptides and AuNP (d_{COM}); (b) snapshot of the conjugates (LL37-SH left and LL37 right) for 50 ns of simulation; (c) distance of each residue to the AuNP for each peptide. (black - LL37-SH, gray - LL37)

the the peptide to the surface within the first 5 ns, after which the anchoring and step-wise lock-down to the surface occur (along the 5 ns to 100 ns interval). At the end of these two stages, the peptide is considered fully adsorbed to the surface, with limited rearrangement. Notably, the step-wise lock-down for LL37 takes longer times when compared to the LL37-SH (see Figure 4.2(a) and 4.2(c)). The time evolution of the distance of each residue to the surface is shown in Figure 4.2(c). Globally, both peptides display a similar behavior, with all the residues fastly moving towards the AuNP within the first few nanoseconds of the simulation. However, there are some distinct features near the

C-terminal. These differences are most likely caused by the presence of the CYS residue, whose strong interaction with the Au surface ends up conditioning the adjacent residues, and, consequently, their adsorption profiles (compared to those of LL37). In fact, the CYS residue itself adsorbs and locks to the AuNP at the very beginning of simulation time.

The information provided by $d_{\text{End-End}}$, RMSD and R_g (Figure 4.3) data, which not only give a clearer picture on the peptide evolution throughout the adsorption process, but also provide additional information regarding the conformational trend and arrangement of the LL37-SH, i.e. whether it remains elongated or folded. Again, the plateauing effect is observed in all metrics plotted in Figure 4.3, which demonstrates the convergence of the system to a stationary state. On the other hand, while the $d_{\text{End-End}}$ converges to ca. 3.40 nm in the LL37-SH/AuNP conjugate, it it arrives at ca. 1.84 nm in the case of the LL37-SH/AuNP. This is a clear indication that the adsorption of the peptide on the AuNP surface promotes its elongation, an effect which, however, is quite more pronounced for the LL37-SH when compared to LL37.

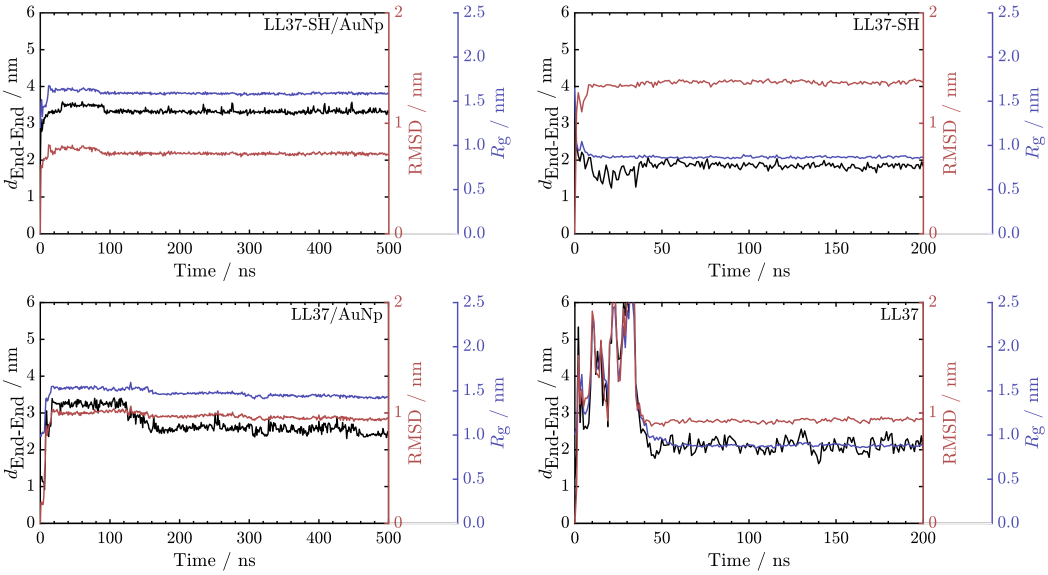

Figure 4.3: Time evolution of end-to-end distance ($d_{\text{End-End}}$), RMSD and R_g with the simulation time for LL37-SH/AuNP and LL37/AuNP conjugates (top and bottom left), LL37-SH and LL37 peptides (top and bottom right).

Free energy and entropy analysis

To check if the FES of the system was properly scanned, its value was determined as a function of the simulation time in terms of the selected CVs. At convergence, the reconstructed profiles should be similar. The outcome of this analysis is shown in Figure 4.4, where the profiles start to overlap from a simulation time of 400 ns, hence demonstrating that the system was properly sampled for the selected conditions. This, alongside the results previously described (Figs. 4.2 and 4.3), confirms that the simulation most likely converged.

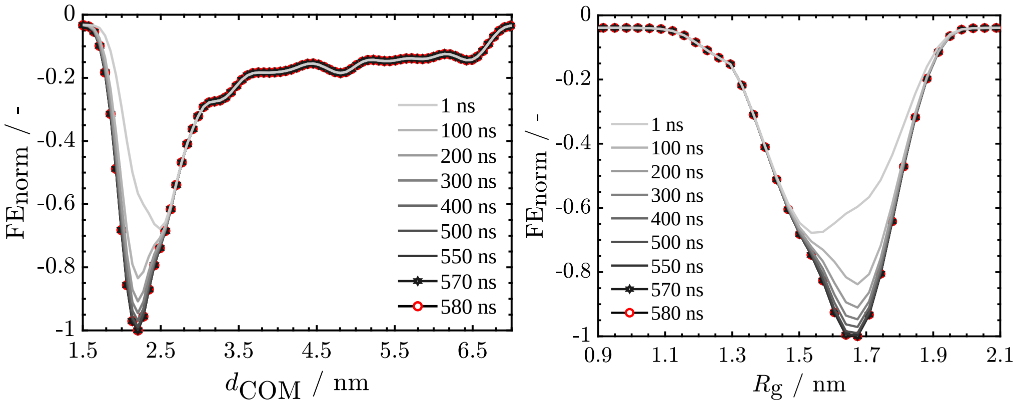

(a) (b)

Figure 4.4: Normalized FE at different timestamps for the evaluated CVs and for the LL37-SH/AuNP conjugate: (a) d_{COM}; (b) R_{g}.

Figure 4.5(a) offers an overview of the reweighted FES (the raw FES, i.e., that was obtained before the reweight process, can be found in Fig. C.3 in Appendix C) as function of both CV, while Figs. 4.5(b) and 4.5(c) show the normalized Free Energy (FE$_{\mathrm{norm}}$) as a function each each CV. A global minimum of -31.4 kJ mol^{-1} occurs at $R_{\mathrm{g}} = 1.62$ nm and $d_{\mathrm{COM}} = 2.11$ nm in the case of LL37-SH/AuNP conjugate (-31.3 kJ mol^{-1} at 1.55 nm R_{g} and 2.16 nm d_{COM} for LL37/AuNP). Figure 4.5(a) highlights the relation between R_{g} and d_{COM} (red curve). When LL37-SH is free the R_{g} value fluctuates between 1.3 to 1.5 nm. However, as it gets closer to the AuNP, this value increases, hitting the lowest free energy at 1.62 nm. The LL37 exhibits a much steadier value when free, around 1.16 nm, eventually hitting 1.55 nm near the surface. The tables with the FE values of both systems can be found in Appendix C.

The energy profiles for both CVs (Figure 4.5(b) and 4.5(c)) are mainly characterized by a single basin, meaning that the FES profile is not complex, and that the metadynamics approach was able to easily reach global minimum and properly describe the complete FES. Bellucci et al.[34] used a similar methodology (metadynamics) to investigate the interaction of alanine dipeptide with a gold surface. Some shoulders in the FES profile for d_{COM} were reported, and the ascribed such a trend to the first contact of the peptide with the gold surface. In fact, for LL37 (Figure 4.5(b) gray curve), d_{COM} starts decreasing steadily from 4.5 nm onwards to the global minimum, but a small shoulder at ca. 2.8 nm is observed. This feature can be related with the first contact of the peptide with the surface and indicate that a metastable conjugate might occur during the adsorption process of the LL37 to the AuNP (two basins visible in Figure 4.5(a)). On the other hand, in the case of LL37-SH (Figure 4.5(b) black curve), d_{COM} decreases steadily up to 3.5 nm before a steeper descent to the global minimum. These FE profiles indicate that the LL37 peptide

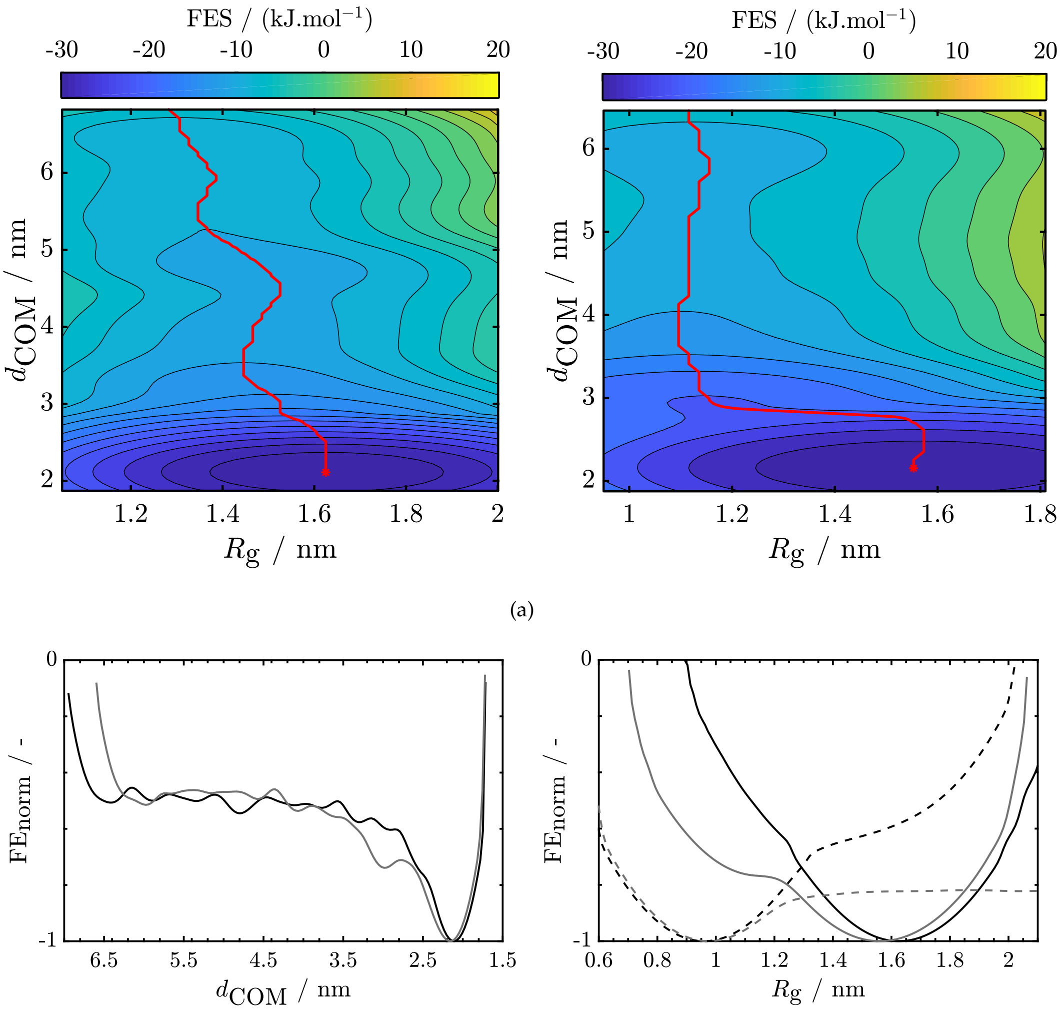

(a)

(b)

(c)

Figure 4.5: (a) Reweighted FES of the system taking into account both CVs for LL37-SH (left) and LL37 (right). Red curve indicate the path of lowest FES for each unique d_{COM} value. Normalized relative FE (reweighted) of the evaluated CVs: (b) (d_{COM}); (c) (R_{g}). (black - LL37-SH, gray - LL37)

can take a longer adsorption process, which is in consistent with the precedent analysis. Being CYS the only differentiating element between the peptides, its presence seems to have a noticeable effect in the formation of the conjugate, and the unveiled smoother FES shows that LL37-SH/AuNP conjugate is more easily achieved. A similar behavior, i.e. enhancement of the interaction of a AMP with a gold surface due to the presence of a CYS residue, was reported by Rai et al.[1].

When comparing the R_{g} for both peptides, remarkable differences are found depending whether AMPs are in the presence of the AuNP or alone in water (Figure 4.5(c)). As the FE reaches the minimum, R_{g} tends to ca. 1.6 nm for both LL37-SH/AuNP and LL37/AuNP conjugates, whereas for the peptides alone that characteristic value decreases to ca. 1.0 nm. Hence, the AMPs in the presence of the AuNP are preferably elongated instead of folded, i.e. the AuNP has a great impact over the AMP structure, somehow compensating the preferable energy state (characterized by lower R_g) of the LL37-SH or LL37 specimens alone. This result, combined with the data shown in Figure 4.3, demonstrate that LL37-SH tends to be elongated in the AuNP surface. In the light of these results, we postulate that the elongation of the peptide might lead to an increased availability of the more active functional groups compared to the free peptide, thus enhancing its activity. This inference is consistent with, and support, experimental evidences on these systems recently reported [2].

With FES properly described for both conjugates, the conformational entropy of each peptide was determined. This metric is commonly used to assess a protein stability. [212] It can be easily determined by evaluating the covariance matrix of Cartesian positional coordinates obtainable by computer simulation, namely from the Schlitter's equation (Eq. 4.1), which uses to the quasi-harmonic quantum mechanical formulation (S'): [213]

$$S' = \frac{1}{2} k_B \ln \left(1 + \frac{k_B T e^2}{\hbar^2} m \langle x^2 \rangle_c \right). \tag{4.1}$$

where k_B is Boltzmann's constant, T is the temperature, e is Euler's Number, $\hbar = h/2\pi$ (here h is Planck's constant), m is the mass and $\langle x^2 \rangle_c$ classical variance. By using the covariance matrix Cartesian positional coordinates, the method circumvents the need to express the entropy in internal coordinates, although at expenses of a somewhat lower accuracy [214]. We believe that the fact of being a quite approximative approach is not a critical issue when used for comparative purposes, as the case. In fact, this approach has being extensively used on peptides [215–219]. The conformational entropies (S_{conf}) for both peptides free (S_{conf}^{Free}) and interacting (adsorbed) with the AuNP (S_{conf}^{Ads}) were computed for the last 5 ns. The results are summarized in Table 4.1. The values for the free peptides reveal a significant loss in entropy. Being the incorporation of CYS (i.e., on going from LL37 to LL37-SH) the only difference between the peptides, this loss is probably consequence of an additional intramolecular stabilization potentiated by that residue. The loss in S_{conf} observed after the adsorption (both peptides) is explained by the decrease of flexibility, i.e. internal degrees of freedom, caused by the structural lock of the peptides into the AuNP. When confronting the two entries of Table 4.1, it appears that the adsorption process has a higher impact in the LL37-SH conformation flexibility, probably due to the strong interaction between cysteine and the AuNP. A detailed analysis of this interaction, however, requires to consider not only entropic effects but also enthalpic issues, notably a presumed covalent binding involving the CYS and the metal surface. The later topic can not be afforded by classical molecular dynamics and therefore is out of the scope of this study.

Table 4.1: Conformational entropy of the peptide backbone using Schlitter's quasi-harmonic approximation.

	$S_{\mathrm{conf}}^{\mathrm{Free}}\,(\mathrm{J\,mol^{-1}\,K^{-1}})$	$S_{\mathrm{conf}}^{\mathrm{Ads}}\,(\mathrm{J\,mol^{-1}\,K^{-1}})$
LL37-SH	6275.48	5154.60
LL37	6616.61	5592.82

LL37-SH bioactivity assessment

Aiming at understanding the reasoning behind the higher antimicrobial activity of the LL37-SH adsorbed to the AuNP than its free counterpart recently reported[2], the solvent accessible surface area (SASA) and the distance of the positively charged functional groups to the peptide backbone was computed. The SASA values refer the total solvent accessible surface area if a molecule was in a bulk solvent alone. This means that this value is not affected when LL37-SH adsorbs to the AuNP surface. Therefore, a decrease of the SASA would represent a compaction of the peptide structure with a decreasing in its surface area, rather than a contact between the peptide and surface with the subsequent exclusion of water[220,221]. However, as it can be seen in Figure 4.6(a), the LL37-SH/AuNP conjugate has a substantially higher SASA, which indicates that the LL37-SH peptide alone tends to fold. Thus, the AuNP induces the LL37-SH to adopt a more elongated conformation, which is expected to promote an increased availability of the functional groups to interact with cells. This was further explored by assessing the location of the positively charged functional groups relatively to the peptide backbone. In fact, considering that positively charged residues play an important role in the AMP activity[222,223], the understanding of its location is crucial. The LL37-SH AMP, among other residues, has multiple arginine and a single lysine. These two residues are characterized by being positively charged. At the

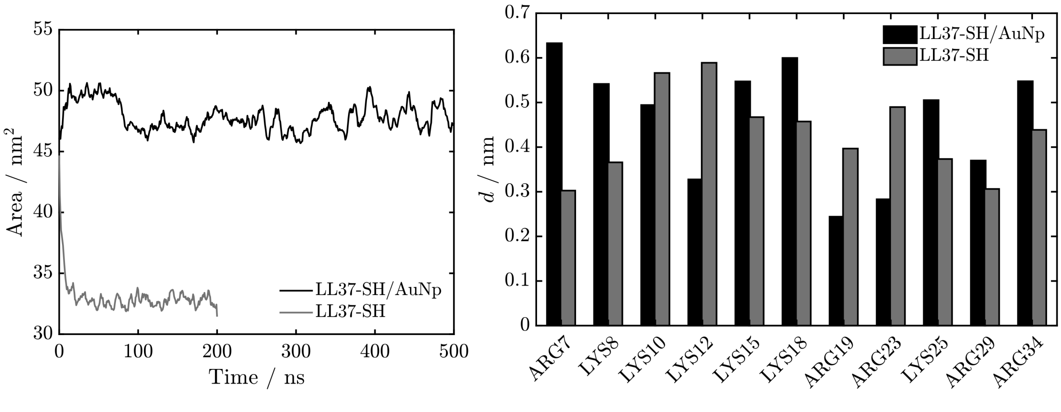

(a) (b)

Figure 4.6: (a) Solvent accessible surface area; and (b) distance of the positively charged functional groups to the peptide backbone for the LL37-SH with the AuNP and alone.

atomistic level, the functional groups responsible for this charge are guanidino group of arginine, and a protonated amine in lysine. Thus, the distance between these groups, 11 in total, to the peptide backbone was computed for the last 10 ns of simulation. The average values for each system are resumed in Figure 4.6(b) (error bars are not shown do to their low values, around 0.01% for the highest value). Overall, for LL37-SH/AuNP conjugate 7 of the 11 functional groups are further away from the AMP backbone when compared to LL37-SH alone. This clearly suggests that the LL37-SH adsorbed to the AuNP tends to have the positive side chains more available to interact with biological systems. Thus, these two factors – i) the tendency to be elongated and; ii) having the positively charged side chains more available – form a quite plausible explanation for the enhanced activity of LL37-SH when adsorbed on a AuNPs.

4.2 Conjugate and biomembrane

Modelling details. Two 200 ns simulations of a system with 20 peptides and AuNP were performed at first. The purpose of these simulations was twofold: i) to estimate how many peptides can adsorb to the surface a 4.3 nm AuNP; ii) to prepare a LL37-SH/AuNP conjugate to be added to the bilayer as an input for the system **BL+AMP/NP** (see below).

Four distinct systems were simulated for analysis purposes. The first (**BL**, the control system to be used as baseline) consists in the bilayer itself neutralized in water, and the second in a stabilized bilayer to study the interaction of a bare AuNP with it (**BL+NP**). The remaining two systems are both formed by the bilayer and 12 LL37-SH peptides. In one case the peptides are dispersed in the simulation box (no AuNP in the system, **BL+AMP**), while in the other case the 12 peptides are adsorberd in the AuNP (**BL+AMP/NP**). This approach potentiate the assessment of the effect of the each component on the bilayer, apart from the conjugate itself. Due the system dimensions, particularly large in some of the cases, the simulation times were adjusted individually in order to produce runs with the duration strictly needed to probe the intended dynamics. Therefore, the he simulations were carried out for 200 ns for **BL**, 600 ns for **BL+NP**, 400 ns for **BL+AMP**, and 1500 ns for **BL+AMP/NP**.

Results and discussion. Starting with the preparation of the LL37-SH/AuNP, it was found that 12 of the 20 peptides inserted in the system adsorbed to the AuNP after 200 ns of simulation (this result was identical in two performed simulations). Snapshots of the final LL37-SH/AuNP conjugate are shown in Fig. 4.7.

The obtained LL37-SH/AuNP conjugate had a concentration of 0.19 LL37-SH per nm^2 of AuNP surface (141 g of LL37-SH per mg of AuNP). Assuming that the number of peptides adsorbed into a AuNP scales linearly with its surface area, one could anticipate that a 21 nm AuNP, i.e. as those reported recently by Comune et al.[2], would be able to accom-

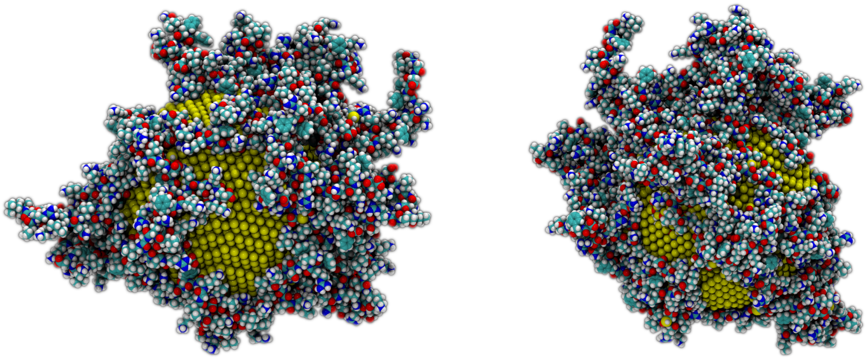

Figure 4.7: Schematic overview of the obtained LL37-SH/AuNP conjugate.

modate ca. 260 peptides. This theoretical value differs considerably from that reported experimentally on the basis of spectroscopic data, viz. 154 peptides per AuNP. This can be explained by some limitations in both the experimental and theoretical approaches in assessing that concentration. Regarding the model, it corresponds to an ideal scenario, in which, strictly speaking, neither the assumed linear scale mentioned above nor the simulated LL37-SH peptides inserted near to the AuNP to promote the adsorption process have an experimental counterpart. Nevertheless, we assume here a somehow ideal condition in which a 21 nm should be able to capture 260 LL37-SH peptides.

The area per lipid (A_{lip}) is a basic metric used when investigating systems with bilayers. It describes the bilayer microstructure with regard to lipids packing, because of its high sensitivity to hydrophilic attraction between head groups and hydrophobic repulsion between non-polar hydrocarbon tails.[224] The A_{lip} is influenced by the selected lipid formulation and by external stimuli (e.g. temperature fluctuation or interaction with external molecules such as proteins). Additionally, the bilayer thickness (D_{HH}) combined with A_{lip} helps in the identification of bilayer microstructure alterations. Phosphorus and oxygen atoms (atoms in the water-bilayer interface region) from the lipidic and cholesterol compositions, respectively, are used as reference in the APL@Voro tool to compute A_{lip} and D_{HH} (Fig. 4.8).

Starting with the baseline system (**BL**) we can observe that both (0.5 nm^2) A_{lip} and (4.0 nm) D_{HH} profiles are fairly stable. The fact that these profiles do not present any major swift indicates that the bilayer is stabilized. The introduction of the 12 LL37-SH into the **BL+AMP** system leads to a slight increase in A_{lip} after 180-200 ns of simulation, although without change in D_{HH}. This can be explained by the migration of the AMPs to the bilayer surface, thus occupying free spaces and, consequently, pushing the lipids and increasing the A_{lip}. However, a different behavior is identified for the systems with a AuNP (**BL+NP** and **BL+AMP/NP**).

The **BL+NP** system exhibits a steep decrease in A_{lip} almost immediately after the start of the simulation. The magnitude of this variation suggests that some kind of substantial

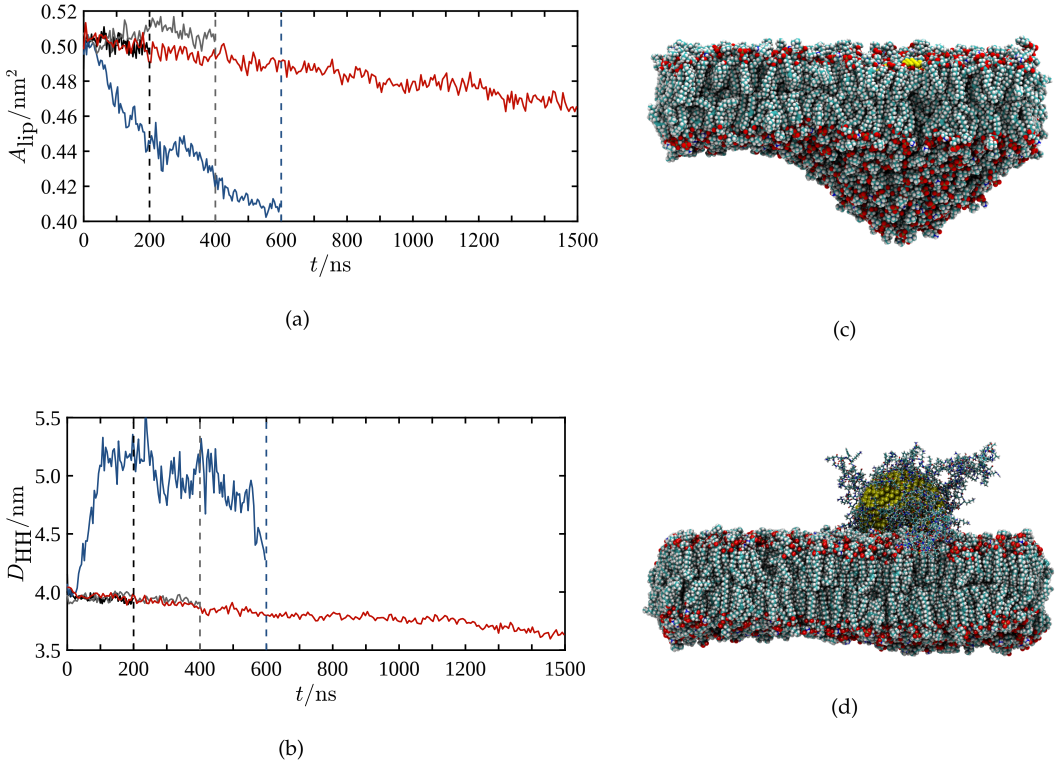

(a) (c)

(b) (d)

Figure 4.8: Evolution of the bilayer properties: (a) A_{lip} averaged between the bilayer leaflets and (b) D_{HH} using phosphorus and oxygen atoms as reference. Snapshots of the end conformations of the (c) **BL+NP** and (d) **BL+AMP/NP** systems. (— **BL**, — **BL+AMP**, — **BL+NP**, — **BL+AMP/NP**)

alteration of the bilayer structure takes place. After evaluating the trajectories, it is possible to observe that the AuNP interacts with the bilayer causing major deformations in its surface by permeating partially (Fig. 4.8(c)). This is corroborated by the increase in D_{HH}, which indicates that the AuNP permeates the bilayer and pushes the leaflets away from each other. A similar behavior was reported by Chen et al.[225] and Mhashal et al.[226] for neutral NPs. Therefore, we postulate that the deformation is caused by the adhesion of the lipids to the AuNP (similarly to the adsorption of the AMPs). Since organic nature of the lipids forming the bilayer makes them prone to adsorb strongly to the surface. In fact, when evaluating the number of solvent molecules near the AuNP surface at the start and at the end of the simulation (Fig. 4.9) a substantial decrease is encountered. This means that the lipids are displacing the water molecules near the AuNP to adsorb to its surface. This suggests that the adsorption mechanic might have some similarities to that of the AMPs.

The simulation results for the system **BL+AMP/NP** shows a less pronounced effect in the bilayer. The conjugate does not permeate the bilayer, remaining over its surface along a physical simulation time of 1500 ns (Fig. 4.8(d)). This could be expected considering that the conjugate has a larger surface area and volume than the bare AuNP, thus requiring more time to displace the bilayer lipids[123]. Nevertheless, a constant decrease of the A_{lip}

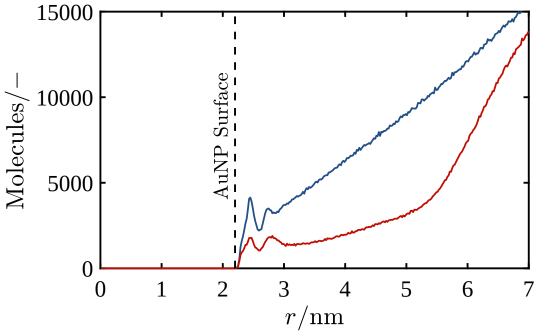

Figure 4.9: Distribution of the solvent molecules as a function of the distance to the AuNP center of mass radius. (— First and — last 1 ns of simulation.)

and D_{HH} can be easily identified (Fig. 4.8). The less pronounced effect that the conjugate has in bilayer properties, when compared to the bare AuNP, can only be attributed to the presence of LL37-SH on its surface. As a matter of fact, we postulate that this behavior is related to the AuNP surface being already saturated with LL37-SH and, therefore, not able to displace the lipids by adsorption (as observed in the **BL+NP** system). This hypothesis is further supported by the constant decrease of the D_{HH} metric, indicating that the conjugate is pulling the bilayer leaflets closer instead of displacing the lipids.

The density profiles of the systems were calculated for the last 2 ns of simulation. With the density profiles, one can pinpoint the the exact location of a given component (group of molecules, molecule or atom) in the simulation box. This is particularly useful for systems with structured materials, such as bilayers and nanoparticles, because it allows to understand their position with fine detail. The density profiles are compiled in the Fig. 4.10. Starting with the density profile of the **BL** system (Fig. 4.10(a)), the obtained profiles are in line with what expected for a bilayer. Bilayer systems are characterized by two symmetric density peaks (red curve) due to the polar groups (phosphorus and oxygen atoms of lipid and cholesterol, respectively) of each leaflet that are located in the interface with water. Between these peaks is located the lipids hydrophobic zone, characterized by the absence of water (blue curve) in this region. Using this profile as baseline, it is clear that the addition of the AuNP to the system, **BL+NP** system (Fig. 4.10(b)), severely affects the bilayer microstructure. The AuNP (yellow curve) is partially inside the bilayer and, consequently, the bilayer polar groups are pushed to the center of the bilayer, leading to the appearance of water molecules in the hydrophobic region of the bilayer. Nonetheless, if we evaluate the coordinates of the center of mass of the AuNP for the last 100 ns of simulation (Fig. 4.11) we can see that the nanoparticle is barely moving, indicating that the system converged to a stable complex.

The density profiles for the **BL+AMP** and **BL+AMP/NP** systems have two additional curves. The black curve describes the LL37-SH peptide residues with hydrophobic side-chains (ILE, LEU, PHE and VAL), and the gray curve is referred to the remaining LL37-SH

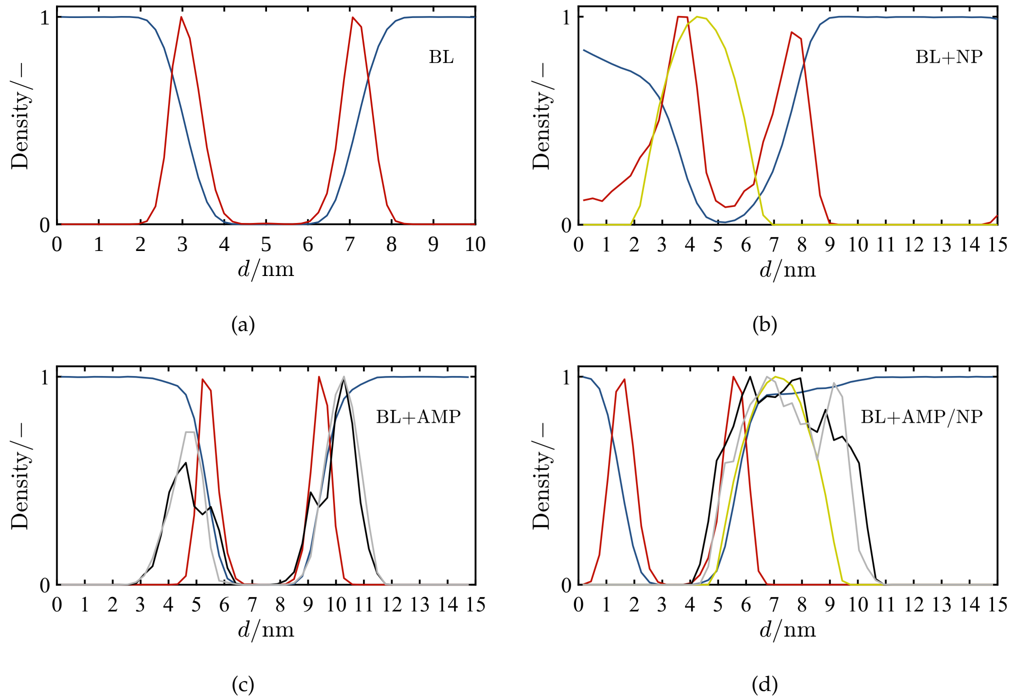

(a) (b) (c) (d)

Figure 4.10: Normalized density profiles, over the *zz* axes, for simulated systems: (a) **BL**; (b) **BL+NP**; (c) **BL+AMP**; (d) **BL+AMP/NP**. (— Water, — Bilayer head zone, — AuNP, — LL37-SH residues with hydrophobic side-chain, — LL37-SH residues with hydrophilic side-chain)

residues. Analyzing the results for the **BL+AMP** system (Fig. 4.10(c)), we can see that all AMPs migrated to the bilayer surface. Comparing the residue types, it is clear that the hydrophobic residues tend to be closer to the center of the bilayer. Expectedly, the residues with hydrophobic side-chain orient themselves to the center of the bilayer (also hydrophobic) acting as an anchor for the remaining peptide. Since only 13 out of the 38 residues have hydrophobic character, the AMP remains in the interface and does not fully permeate the bilayer. By remaining in the interface, the AMPs are capable to move freely in the bilayer surface without detaching (Figs. 4.11(c) and 4.11(d)). A similar behavior is identified for the **BL+AMP/NP** system which, unlike the bare AuNP, moves freely over the bilayer surface. This capability can be associated to the AMPs adsorbed in its surface which: i) occupy the gold surface precluding a direct interaction with the lipids; ii) the AMP hydrophobic side-chains are oriented to the bilayer center (Fig. 4.10(d)), anchoring the conjugate to the bilayer surface.

Finally, the lipid alkyl tails order parameter (S_{CD}) and the simulation box charge density of non-Water components were determined. The S_{CD} provide information regarding the flexibility of the lipid alkyl tails. Only the results for the SN1 tail are displayed because the tendencies are similar to the SN2. High S_{CD} values indicate that the lipids are more stiff and, therefore, the bilayer is less fluid. The charge density allows to map the distribution of charges throughout the simulation, in this case, with emphasis in the bi-

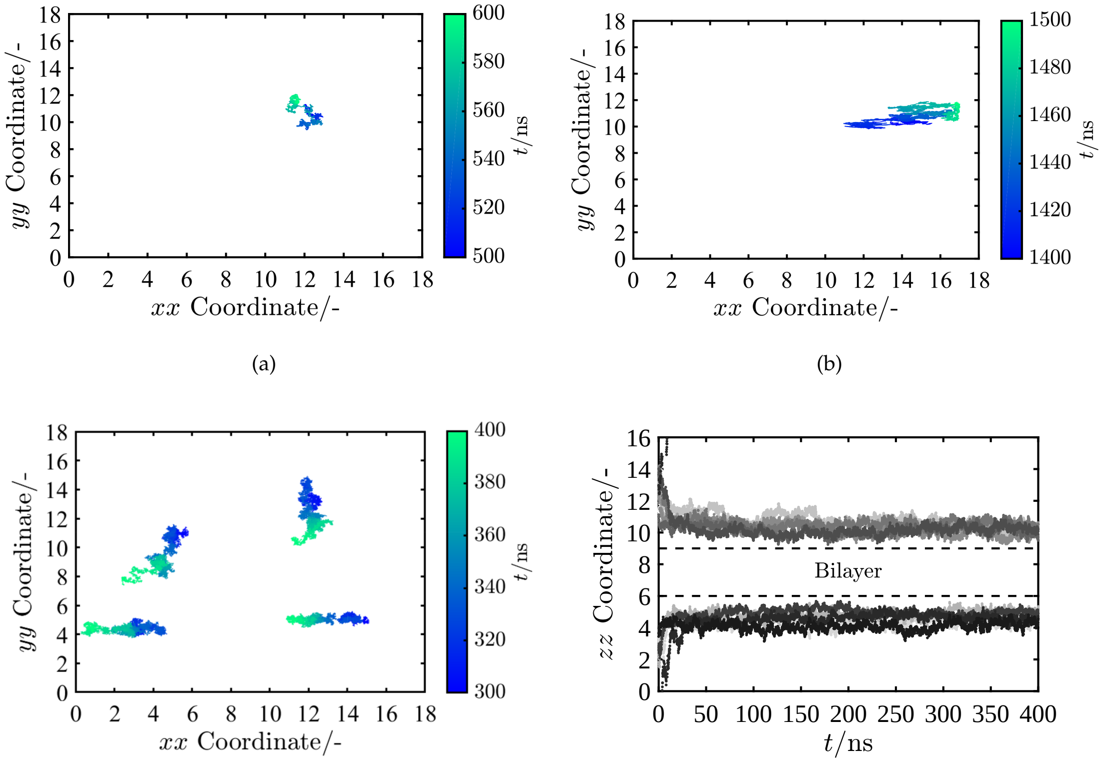

(a) (b)

(c) (d)

Figure 4.11: Coordinates of the AuNP center of mass: (a) **BL+NP**; (b) **BL+AMP/NP**; and of the center of mass of 4 representative LL37-SH (c) **BL+AMP** for the last 100 ns of simulation. (d) *zz* coordinate for the LL37-SH peptides (each color curve is one peptide) during the simulation. The coordinate scales are concordant with the simulation box dimension.

layer. The analysis output is summarized in Fig. 4.12. Comparing the order parameter (Fig. 4.12(a)) between systems, it is clear that only the **BL+NP** system presents a substantial difference from the baseline. This difference is characterized by a decreasing in S_{CD}

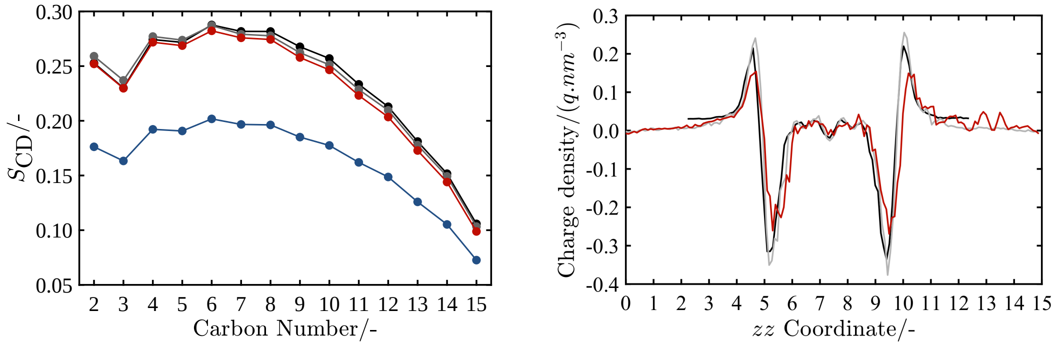

(a) (b)

Figure 4.12: (a) S_{CD} per atom for SN1 carbon tail. (b) System, water not included, charge density. Metrics computed for the last 5 ns of simulation. (— **BL**, — **BL+AMP**, — **BL+NP**, — **BL+AMP/NP**)

for all the carbons in SN1 tail, indicating that the bilayer is less structured. This outcome is a consequence of the deformation caused by the AuNP in the bilayer. The remaining systems exhibit nothing but a slight decrease in the S_{CD}, which can be clearly identified for the **BL+AMP/NP** system. Again, this less pronounced reduction can be ascribed to the LL37-SH corona which prevents direct contact between the gold and the bilayer. As far the charge density is concerned (Fig. 4.12(b)), distinct behaviors for **BL+AMP** and **BL+AMP/NP** system can be identified when using the **BL+NP** system profile as baseline. The profile is characterized by a positive peak, at around 4.5 nm and 10 nm, induced by the N^+ atom in the choline group and a negative peak, at ca. 5 nm and 9.5 nm, promoted by the O^- atom in the phosphate group. These peaks become more pronounced with the addition of free LL37-SH to the system (**BL+AMP**). This suggests that, by remaining in the bilayer-water interface, the AMPs are affecting the structure of the bilayer head region. The opposite effect is verified for the **BL+AMP/NP** system, with the peaks being less pronounced. This lead us to believe that, despite the LL37-SH corona, the conjugate disturbs the bilayer head region.

When comparing the computed results with data obtained experimentally, noticeable differences are found in the behavior of LL37-SH/AuNP when interacting with the keratinocytes. Comune et al.[2] have demonstrate that the conjugates are internalized by the keratinocytes, a feature not identified by the simulation approach. The discrepancy can be explained by the somehow departure of the model from the actual scenario. On the one hand, strictly speaking the bilayer does not mimic the real biomembrane (which also includes elements such as proteins and carbohydrates, among others). One the other hand, the conjugate described experimentally is said to have a lower concentration of AMPs compared to that used in the model (0.11 vs. 0.19 LL37-SH per nm^2 of AuNP surface). We speculate that the experimental conjugate might have more free gold surface exposed to a direct contact with the biomembrane, and as it was discussed above the direct contact between the bilayer and the AuNP promotes severe lipid displacement leading to its internalization. Further studies are still needed in any case.

4.3 Conclusion

The assessment of the adsorption process of the LL37-SH into a AuNP allowed to rationalize the computational approach used thereafter. By comparing the diffusion profiles it was found that the adsorption process is rather similar in both CM-SH and LL37-SH AMPs. However, since the latter has a longer chain, the simulation time required to the peptide adopt a fully stabilized state is higher. The peptide C-terminal tends to adsorb faster to the AuNP, a consequence of the presence the CYS residue. No distinct secondary structure was identified for LL37-SH at the simulated conditions, i.e. water solvent at pH 7.

The interaction of a cathelicidin-derived antimicrobial peptide with a AuNP and the activity of the subsequently formed conjugate was investigated from atomistic-scale simulations by using well-tempered metadynamics. The temporal analysis of d_{COM}, $d_{\text{End-End}}$, RMSD and R_{g} data showed that the cathelicidin with CYS (LL37-SH) tends to adsorb and stabilize onto the AuNP faster than LL37. The S_{conf} analysis showed that the AuNP has a substantial effect on the conformational entropy of both peptides, whose values decrease when adsorbed. Some differences between LL37-SH and LL37 were also found, with the CYS residue reducing the S_{conf} of the peptide both free and adsorbed. The FES in terms of d_{COM} and R_{g} as CVs evidenced a comparable landscape for both peptides, although a secondary low energy site has been identified in the case of LL37, indicating a possible occurrence of metastable LL37/AuNP. Again, the incorporation of CYS in the base peptide appeared to have a noticeable effect in the formation of the LL37-SH/AuNP conjugate, as suggested by a smoother FES.

The comparative simulation of the LL37-SH free in water helped in unveiling the effect of the AuNP on this peptide. The results showed a dramatic decreasing in R_{g} (ca. 50 %.) in the absence of the AuNP, meaning that the peptide is preferably elongated after being adsorbed to the AuNP. This was confirmed by the comparative analysis based on the solvent accessible surface area for the free LL37-SH and in the presence of the AuNP. Together, the revealed elongation and the identified readiness of antimicrobial functional groups in the LL37-SH/AuNP conjugate explain the reported enhanced activity of the LL37-SH/AuNP conjugate when compared to the LL37-SH peptide *per se*.

The assessment of the interaction of the LL37-SH/AuNP, and its components, with a keratinocyte bilayer was probed, totalizing almost $3\,\mu$s of simulation time. The bilayer modelled to match the lipid-cholesterol composition of a keratinocyte cell, **BL** system, presented typical A_{lip}, D_{HH} and density profiles. The addition of the AuNP to the system (**BL+NP**) caused major deformations in the bilayer. Almost instantly the AuNP migrates to the bilayer surface and starts displacing the lipids. This displacement leads to a decrease of A_{lip} and an increase of D_{HH}, and the AuNP eventually migrates partially to the bilayer interior. Considering this behavior, and the fact that the lipids are adsorbing to the AuNP by displacing the water in its surface, an adsorption mechanism similar to that for AMPs is anticipated.

When comparing the system with the AuNP with the system with the conjugate (**BL+AMP/NP**), a substantial less dramatic effect on the bilayer in the latter case is found. The nanoparticle corona formed by the LL37-SH shields the AuNP from the lipids. Due to this shielding effect the conjugate does not permeate the bilayer but remains in its surface. As a consequence the charge distribution in the bilayer-water interface is disturbed by the conjugate. On the other hand, the free LL37-SH (**BL+AMP**) intensifies the charge distribution peaks in the bilayer-water interface. This intensification occurs because LL37-SH remains consistently in the bilayer surface. The density profiles show that the residues with hydrophobic side-chain are oriented to the bilayer interior. Hence, when the peptide migrates to the bilayer surface, these residues act as an anchor hampering its release back to the solvent.

5. Conclusion

Despite modern medicine advances, infections are still the second leading cause of death worldwide, namely as a consequence of an extensive use of drugs, such as antibiotics, which, in turn, has led to the emergence of multidrug resistant of common pathogens. Thus, besides developing new drugs, it is also mandatory to optimize existing ones in order to yield high effectiveness with lower dosage. Among other possibilities, AMPs present a great potential in this framework. Nonetheless, AMPs lack stability and targeting capabilities, which has motivated the use of nanocarriers to improve their characteristics. In this context, AuNPs where found to be great nanocarriers for AMPs.

The computational investigation of the cysteine-terminated AMPs here reported was divided in three vectors: i) study of the adsorption process *per se*; ii) free energy investigation using advanced sampling methods; iii) interaction of AMP/AuNP conjugates with a biomembrane mimetic model. Each topic was tackled from different methodologies in order to address the systems specificities. The chosen metrics extracted from the selected molecular modelling and simulation scenarios allowed to unveil new details on the target systems as summarized below.

Study of the adsorption process *per se*. The adsorption process presents a similar dynamic behavior for both AMPs investigated, with the approaching distance to the gold surface resembling an exponential decay. The overall process is segmented in four regimes: i) unbiased diffusion – free diffusion of the AMP in the solvent –; ii) biased diffusion – diffusion of the AMP influenced by the gold surface attraction field –; iii) anchoring – partial attachment of the AMP to the gold surface –; and iv) lockdown – structural lockdown of the AMP in the gold surface, i.e. formation of AMP/gold conjugate –. The results show that the way the peptides approach the surface dictates the final conformation and the time required to achieve it. Nonetheless, a higher affinity between the AMPs and the gold surface was found for the protons bound to α-carbons, characterized by a higher frequency of contacts to the gold surface during the simulations.

Globally, the simulation time required to assess the adsorption process was higher for the LL37 than for the CM. This is consequence of the higher number of residues in the LL37 AMP, leading to a slower diffusion and lockdown regimes. Comparing both surface topologies tested, slab vs. NP, the dynamic behavior of the system was found to be similar. Nonetheless, some residues, such as PHE, present a higher affinity to the NP. Similarly, no changes in the dynamic behavior were identified for different NP diameters (2, 4, and 6 nm).

Ultimately, it was demonstrated that the presence of cysteine (CYS) at the C-terminus plays a stabilization role on the later stages of the adsorption process. The CYS residue promotes a faster stabilization of the CM-SH peptide, when compared to its CM counterpart, without significantly affecting the diffusion regime. Unlike the other residues, CYS was found consistently binded to the surface with negligible occurrences of detachment back to the solvent. In fact, in the multiplicity of the performed simulations the CYS residue adsorbed and locked to the gold surface at the very beginning of the simulation.

Free energy investigation using advanced sampling methods. The free energy characterization allowed to identify the local and global minima of the various studied systems, thus consolidating the results obtained using the standard approach. The selected CVs – R_g and d_COM – were crucial to understand how the FE varies with the distance between the entities (AMP and AuNP) and if the AMP is preferably folded or elongated. The obtained FES landscape showed that all the AMPs have, invariably, a lower FE for lower d_COM. This result substantiates the data obtained by standard MD, quantitatively demonstrating that the AMPs are preferably adsorbed to the surface. While the results for the d_COM were similar for all the AMPs, a different outcome was observed for the R_g.

In the present of a AuNP, it was found that the AMPs are preferably elongated instead of folded. The conjugate formed by the AMPs and AuNP exhibits a lower FE for higher R_g, than their free counterparts. We postulate that this elongation is promoted by the strong attraction of the AuNP, overriding any structural conformation previously established by the AMP. Additionally, the FES also demonstrates that the CYS terminated AMPs (CM-SH and LL37-SH) have a even higher R_g value than their counterparts (CM and LL37). This result is specially relevant when assessing the AMP bioactivity, since elongated AMPs are expected to have a higher availability of the functional groups to interact with cells.

Undoubtedly, the use of the metadynamics algorithm presents multiple advantages over the standard approach. However, possibly as a consequence of the small residue chains studied, the FE of R_g and d_COM are rather smooth and have distinct global minima. This indicates that a long enough classical MD run should be able to probe the complete energy spectrum, thus avoiding the bias potentials that characterizes the metadynamics. Therefore, one can assume that both metadynamics and standard MD approaches are both plausible frameworks to study the interaction of small peptides with gold surfaces, which is a technical detail that should not be underestimated.

Interaction of AMP/AuNP conjugates with a biomembrane. The affinity of the LL37-SH/AuNP conjugate with the bilayer was investigated by simulating the interaction of a keratinocyte bilayer with the conjugate and their components (this investigation was critically demanding due to both the system dimensions and intrinsic dynamics, and, consequently, the simulation time required to probe the phenomena). The results show that the keratinocyte model presents the typical behavior of a bilayer. The addition of the bare AuNP to the system lead to major deformations to the bilayer, most likely caused by the adsorption of the lipids to the NP surface (similar to that observed in the case of AMPs). On the other hand, the systems with AMP appear to have a much less harsh effect in the bilayer properties. The corona formed by the LL37-SH shields the lipids from the AuNP, thus preventing the bilayer deformation. As consequence, only a slight disturbance in the bilayer surface charges was identified. In contrast, the migration of the free LL37-SH to the bilayer surface leads to an intensification of the charge distribution peaks in the bilayer-water interface. This behavior indicates that the free AMP might have a stabilizing effect in bilayer.

Prospective challenges Considering the conclusions outlined above and the evolution of the simulation algorithms and hardware during the last years, one can envisage the following tasks as future work.

1. **Resort to QM/MM to assess thiol-gold interaction.** Cysteine residues are know to interact strongly with the gold, forming chemical bounds by means of the thiol functional group. The used approaches, classical MD and metadynamics, present a good solution to understand the system at an atomistic level while providing insights about overall tendencies at a higher scale. However, these approaches fall short when trying to simulate chemical reactivity. *Ab initio* MD is not, and will not be in the near future, a feasible alternative in virtue of the prohibitive computational load, which precludes the simulation of systems as large as those tackled in this thesis. In this situation, hybrid QM/MM methods[227,228] can be used to investigate strategic sections of the systems at a quantum mechanics (QM) level of theory. By combining QM with molecular mechanics (MM), these hybrid methods allow to simulate electronic effects (including bond breaking/formation) for the portion described by QM while the remaining system is described by MM. An alternative would be to build a model of the AMP/AuNP conjugate with the AMP already chemically bonded to the AuNP by means of the thiol group.

2. **Enhance conjugates FES by testing more CVs.** The selected CVs – R_g and d_{COM} – are a solid choice when investigating adsorption processes. The d_{COM} CV allows to understand the variation of the FE with distance between the entities involved in the adsorption process, while R_g provides information about the structural organization of the AMPs. However, these results might be substantially enriched with the assessment of more CVs, although at expences of more and more computational load. The description of CV such as **CONTACTMAP** (map the number of contacts between entities), **CS2BACKBONE** (AMP backbone chemical shifts), **TORSION** (torsional angles between residues) and **DHENERGY** (Debye-Huckel interaction energy between user defined groups) should wide the knowledge on the investigated systems.

Additionally, data such as AMP backbone chemical shifts could potentially help to rationalize corresponding experimental data.

3. **Leverage coarse-grain models to further explore bilayer systems.** In order to mimic the interaction of nanostructured materials, such as NPs and bilayers, it is required to: i) have a system large enough to house all the components (volume in the region of multiple dozens of nm^3); ii) produce long enough runs to capture the complete phenomena taking place (probably tens of μs). This implies the availability of a powerful computer cluster allocated for several months. In fact, this is a challenge faced when simulating bilayer systems, which requires, in some cases (as in the current study), multiple months of computational time. On way to work around this issue is to resort to coarse-grain models, with the MARTINI force-field[229,230] presenting the greatest potential. Nowadays, most common molecules (lipids, polymers, amino acids, DNA, RNA, etc.) have already a coarse-grain force-field described. By approaching molecular functional groups or sections of molecules to a single particle, coarse-grain models allow to dramatically decrease the number of particles in the system. This translates into a substantial reduction of computational load, allowing the production of large simulation runs in a fraction of computation time. However, it should be stressed that this simplification of the molecular model entails the loss of atomistic level detail.

Bibliography

[1] A. Rai, S. Pinto, T. R. Velho, A. F. Ferreira, C. Moita, U. Trivedi, M. Evangelista, M. Comune, K. P. Rumbaugh, P. N. Simões, L. Moita, and L. Ferreira, "One-step synthesis of high-density peptide-conjugated gold nanoparticles with antimicrobial efficacy in a systemic infection model," *Biomaterials*, vol. 85, pp. 99–110, apr 2016.

[2] M. Comune, A. Rai, K. K. Chereddy, S. Pinto, S. Aday, A. F. Ferreira, A. Zonari, J. Blersch, R. Cunha, R. Rodrigues, J. Lerma, P. N. Simões, V. Préat, and L. Ferreira, "Antimicrobial peptide-gold nanoscale therapeutic formulation with high skin regenerative potential," *J. Control. Release*, vol. 262, pp. 58–71, sep 2017.

[3] A. F. Ferreira, A. Rai, L. Ferreira, and P. N. Simões, "Findings on the interaction of the antimicrobial peptide cecropin-melittin with a gold surface from molecular dynamics studies," *Eur. Biophys. J.*, vol. 46, pp. 247–256, apr 2017.

[4] A. F. Ferreira, M. Comune, A. Rai, L. Ferreira, and P. N. Simões, "Atomistic-Level Investigation of a LL37 Conjugated Gold Nanoparticle by Well-Tempered Metadynamics," *J. Phys. Chem. B*, p. acs.jpcb.8b05717, aug 2018.

[5] C. T. Walsh and T. a. Wencewicz, "Prospects for new antibiotics: a molecule-centered perspective.," *J. Antibiot. (Tokyo).*, vol. 67, pp. 7–22, Jan. 2014.

[6] World Health Organization (WHO), "Deaths by cause, sex and mortality stratum in who regions, estimates for 2002 - the world health report 2004," tech. rep., WHO, 2004.

[7] B. Spellberg, J. H. Powers, E. P. Brass, L. G. Miller, and J. E. Edwards, "Trends in antimicrobial drug development: implications for the future.," *Clin. Infect. Dis.*, vol. 38, pp. 1279–86, May 2004.

[8] World Health Organization (WHO), "Global tuberculosis report 2013," tech. rep., WHO, 2013.

[9] E. Tacconelli and N. Magrini, "Global priority list of antibiotic-resistant bacteria to guide research, discovery, and development of new antibiotics," tech. rep., World Health Organization, 2017.

[10] G. Wang, X. Li, and Z. Wang, "APD3: the antimicrobial peptide database as a tool for research and education.," *Nucleic Acids Res.*, vol. 44, no. November 2015, pp. D1087–D1093, 2016.

[11] Y. Li, Q. Xiang, Q. Zhang, Y. Huang, and Z. Su, "Overview on the recent study of antimicrobial peptides: origins, functions, relative mechanisms and application.," *Peptides*, vol. 37, pp. 207–15, Oct. 2012.

[12] R. E. W. Hancock and H.-G. Sahl, "Antimicrobial and host-defense peptides as new anti-infective therapeutic strategies," *Nat. Biotech.*, vol. 24, pp. 1551–1557, Dec. 2006.

[13] T. Nakatsuji and R. L. Gallo, "Antimicrobial Peptides: Old Molecules with New Ideas," *J. Invest. Dermatol.*, vol. 132, no. 3, pp. 887–895, 2012.

[14] A. Izadpanah and R. L. Gallo, "Antimicrobial peptides," *J. Am. Acad. Dermatol.*, vol. 52, pp. 381–90; quiz 391–2, Mar. 2005.

[15] M. C. Roco, *Overview*, ch. 1, pp. 1–23. Wiley-Blackwell, 2017.

[16] J. Conde, G. Doria, and P. Baptista, "Noble metal nanoparticles applications in cancer.," *J. Drug Deliv.*, vol. 2012, p. 751075, Jan. 2012.

[17] S. T. Selvan, T. T. Y. Tan, D. K. Yi, and N. R. Jana, "Functional and multifunctional nanoparticles for bioimaging and biosensing.," *Langmuir*, vol. 26, pp. 11631–41, July 2010.

[18] P. Baptista, E. Pereira, P. Eaton, G. Doria, A. Miranda, I. Gomes, P. Quaresma, and R. Franco, "Gold nanoparticles for the development of clinical diagnosis methods.," *Anal. Bioanal. Chem.*, vol. 391, pp. 943–50, June 2008.

[19] X. Huang and M. a. El-Sayed, "Gold nanoparticles: Optical properties and implementations in cancer diagnosis and photothermal therapy," *J. Adv. Res.*, vol. 1, pp. 13–28, Jan. 2010.

[20] X. Huang, P. K. Jain, I. H. El-Sayed, and M. a. El-Sayed, "Gold nanoparticles: interesting optical properties and recent applications in cancer diagnostics and therapy.," *Nanomedicine (Lond).*, vol. 2, pp. 681–93, Oct. 2007.

[21] P. Ghosh, G. Han, M. De, C. K. Kim, and V. M. Rotello, "Gold nanoparticles in delivery applications.," *Adv. Drug Deliv. Rev.*, vol. 60, pp. 1307–15, Aug. 2008.

[22] M. S. Yavuz, Y. Cheng, J. Chen, C. M. Cobley, Q. Zhang, M. Rycenga, J. Xie, C. Kim, K. H. Song, A. G. Schwartz, L. V. Wang, and Y. Xia, "Gold nanocages covered by smart polymers for controlled release with near-infrared light.," *Nat. Mater.*, vol. 8, pp. 935–9, Dec. 2009.

[23] S. Bhattacharyya, R. a. Kudgus, R. Bhattacharya, and P. Mukherjee, "Inorganic nanoparticles in cancer therapy.," *Pharmaceut. Res.*, vol. 28, pp. 237–59, Feb. 2011.

[24] L. H. Peng, Y. F. Huang, C. Z. Zhang, J. Niu, Y. Chen, Y. Chu, Z. H. Jiang, J. Q. Gao, and Z. W. Mao, "Integration of antimicrobial peptides with gold nanoparticles as unique non-viral vectors for gene delivery to mesenchymal stem cells with antibacterial activity," *Biomaterials*, vol. 103, pp. 137–149, 2016.

[25] P. Wadhwani, N. Heidenreich, B. Podeyn, J. Bürck, and A. S. Ulrich, "Antibiotic gold: tethering of antimicrobial peptides to gold nanoparticles maintains conformational flexibility of peptides and improves trypsin susceptibility," *Biomater. Sci.*, vol. 5, pp. 817–828, 2017.

[26] B. Casciaro, M. Moros, S. Rivera-Fernández, A. Bellelli, J. M. de la Fuente, and M. L. Mangoni, "Gold-nanoparticles coated with the antimicrobial peptide esculentin-1a(1-21)NH2 as a reliable strategy for antipseudomonal drugs," *Acta Biomater.*, vol. 47, pp. 170–181, 2017.

[27] H. Gu, P. L. Ho, E. Tong, L. Wang, and B. Xu, "Presenting Vancomycin on Nanoparticles to Enhance Antimicrobial Activities," *Nano Lett.*, vol. 3, pp. 1261–1263, Sept. 2003.

[28] P. R. Hall, B. Hjelle, D. C. Brown, C. Ye, V. Bondu-Hawkins, K. A. Kilpatrick, and R. S. Larson, "Multivalent presentation of antihantavirus peptides on nanoparticles enhances infection blockade," *Antimicrob. Agents Ch.*, vol. 52, no. 6, pp. 2079–2088, 2008.

[29] L. Liu, K. Xu, H. Wang, J. T. K., W. Fan, S. S. Venkatraman, L. Li, and Y.-Y. Yang, "Self-assembled cationic peptide nanoparticles as an efficient antimicrobial agent," *Nat. Nano.*, vol. 4, pp. 457–463, July 2009.

[30] H. Heinz, B. L. Farmer, R. B. Pandey, J. M. Slocik, S. S. Patnaik, R. Pachter, and R. R. Naik, "Nature of molecular interactions of peptides with gold, palladium, and Pd-Au bimetal surfaces in aqueous solution.," *J. Am. Chem. Soc.*, vol. 131, pp. 9704–14, July 2009.

[31] J. Yu, M. L. Becker, and G. a. Carri, "A molecular dynamics simulation of the stability-limited growth mechanism of peptide-mediated gold-nanoparticle synthesis.," *Small*, vol. 6, pp. 2242–5, Oct. 2010.

[32] J. Yu, M. L. Becker, and G. A. Carri, "The influence of amino acid sequence and functionality on the binding process of peptides onto gold surfaces.," *Langmuir*, vol. 28, pp. 1408–17, Jan. 2012.

[33] L. Bellucci, G. Brancolini, A. Calzolari, O. C. Parramon, S. Corni, and R. D. Felice, "Proteins and Peptides at Gold Surfaces: Insights from Atomistic Simulations," in *Proteins Interfaces III State Art*, ch. 11, pp. 229–250, 2012.

[34] L. Bellucci and S. Corni, "Interaction with a Gold Surface Reshapes the Free Energy Landscape of Alanine Dipeptide," *J. Phys. Chem. C*, vol. 118, pp. 11357–11364, may 2014.

[35] R. O. Dror, R. M. Dirks, J. Grossman, H. Xu, and D. E. Shaw, "Biomolecular Simulation: A Computational Microscope for Molecular Biology," *Annu. Rev. Biophys.*, vol. 41, no. 1, pp. 429–452, 2012.

[36] A. F. Ferreira, R. J. Lopes, and P. N. Simões, "In silico research in drug delivery systems," in *Drug Delivery Systems: Advanced Technologies Potentially Applicable in Personalised Treatment* (J. Coelho, ed.), vol. 4 of *Advances in Predictive, Preventive and Personalised Medicine*, pp. 271–313, Springer Netherlands, 2013. (And references therein.).

[37] E. J. Maginn and J. R. Elliott, "Historical Perspective and Current Outlook for Molecular Dynamics As a Chemical Engineering Tool," *Ind. Eng. Chem. Res.*, vol. 49, pp. 3059–3078, Apr. 2010.

[38] W. a. de Jong, E. Bylaska, N. Govind, C. L. Janssen, K. Kowalski, T. Müller, I. M. B. Nielsen, H. J. J. van Dam, V. Veryazov, and R. Lindh, "Utilizing high performance computing for chemistry: parallel computational chemistry.," *Phys. Chem. Chem. Phys.*, vol. 12, pp. 6896–920, July 2010.

[39] M. J. Penna, M. Mijajlovic, and M. J. Biggs, "Molecular-level understanding of protein adsorption at the interface between water and a strongly interacting uncharged solid surface," *J. Am. Chem. Soc.*, vol. 136, pp. 5323–5331, 2014.

[40] J. N. Onuchic, Z. Luthey-Schulten, and P. G. Wolynes, "THEORY OF PROTEIN FOLDING: The Energy Landscape Perspective," *Annu. Rev. Phys. Chem.*, vol. 48, pp. 545–600, oct 1997.

[41] R. C. Bernardi, M. C. R. Melo, and K. Schulten, "Enhanced sampling techniques in molecular dynamics simulations of biological systems," *BBA - Gen. Subj.*, vol. 1850, no. 5, pp. 872–877, 2014.

[42] V. Spiwok, Z. Sucur, and P. Hosek, "Enhanced sampling techniques in biomolecular simulations.," *Biotechnol. Adv.*, vol. 33, pp. 1130–40, nov 2015.

[43] R. Galvelis and Y. Sugita, "Replica state exchange metadynamics for improving the convergence of free energy estimates," *J. Comput. Chem.*, vol. 36, no. 19, pp. 1446–1455, 2015.

[44] F. Pietrucci, "Strategies for the exploration of free energy landscapes: Unity in diversity and challenges ahead," *Rev. Phys.*, vol. 2, pp. 32–45, 2017.

[45] European Technology Platform on NanoMedicine, Nanotechnology for Health, "Vision paper and basis for a strategic research agenda for nanomedicine," tech. rep., European Technology Platform on Nanomedicine, 2005.

[46] P. Boisseau and B. Loubaton, "Nanomedicine, nanotechnology in medicine," *Comptes Rendus Phys.*, vol. 12, pp. 620–636, Sept. 2011.

[47] W. H. De Jong and P. J. a. Borm, "Drug delivery and nanoparticles:applications and hazards.," *Int. J. Nanomedicine*, vol. 3, no. 2, pp. 133–149, 2008.

[48] P. Alves, A. A. Hugo, E. E. Tymczyszyn, A. F. Ferreira, R. Fausto, P. F. Pérez, J. F. J. Coelho, P. N. Simões, and A. Gómez-Zavaglia, "Effect of cholesterol-poly(N,N-dimethylaminoethyl methacrylate) on the properties of stimuli-responsive polymer liposome complexes.," *Colloids Surf. B. Biointerfaces*, vol. 104, pp. 254–61, Apr. 2013.

[49] A. Ferreira, P. Alves, J. Coelho, M. Gil, and P. Simões, "Molecular dynamics study of oligomer-membrane complexes with biomedical relevance," in *Characterization and Development of Biosystems and Biomaterials* (A. Öchsner, L. F. M. da Silva, and H. Altenbach, eds.), vol. 29 of *Advanced Structured Materials*, pp. 55–67, Springer Berlin Heidelberg, 2013.

[50] G. Wang, X. Li, and Z. Wang, "APD2: The updated antimicrobial peptide database and its application in peptide design," *Nucleic Acids Res.*, vol. 37, no. October 2008, pp. 933–937, 2009.

[51] X. Zhao, H. Wu, H. Lu, G. Li, and Q. Huang, "LAMP: A Database Linking Antimicrobial Peptides.," *Plos One*, vol. 8, p. e66557, Jan. 2013.

[52] F. H. Waghu, L. Gopi, R. S. Barai, P. Ramteke, B. Nizami, and S. Idicula-Thomas, "CAMP: Collection of sequences and structures of antimicrobial peptides.," *Nucleic Acids Res.*, vol. 42, pp. D1154–8, Jan. 2014.

[53] K. V. R. Reddy, R. D. Yedery, and C. Aranha, "Antimicrobial peptides: premises and promises.," *Int. J. Antimicrob. Ag.*, vol. 24, pp. 536–47, Dec. 2004.

[54] G. Yu, D. Y. Baeder, R. R. Regoes, and J. Rolff, "Combination Effects of Antimicrobial Peptides," *Antimicrob. Agents Chemother.*, vol. 60, pp. 1717–1724, mar 2016.

[55] H. Steiner, D. Hultmark, A. Engström, H. Bennich, and H. G. Boman, "Sequence and specificity of two antibacterial proteins involved in insect immunity," *Nature*, vol. 292, pp. 246–248, July 1981.

[56] D. Field, M. Begley, P. M. O'Connor, K. M. Daly, F. Hugenholtz, P. D. Cotter, C. Hill, and R. P. Ross, "Bioengineered nisin A derivatives with enhanced activity against

both Gram positive and Gram negative pathogens.," *Plos One*, vol. 7, p. e46884, Jan. 2012.

[57] I. M. Torcato, Y. H. Huang, H. G. Franquelim, D. Gaspar, D. J. Craik, M. a. R. B. Castanho, and S. Troeira Henriques, "Design and characterization of novel antimicrobial peptides, R-BP100 and RW-BP100, with activity against Gram-negative and Gram-positive bacteria," *Biochim. Biophys. Acta - Biomembr.*, vol. 1828, no. 3, pp. 944–955, 2013.

[58] Z. Jiang, A. I. Vasil, L. Gera, M. L. Vasil, and R. S. Hodges, "Rational design of α-helical antimicrobial peptides to target Gram-negative pathogens, Acinetobacter baumannii and Pseudomonas aeruginosa: utilization of charge, 'specificity determinants,' total hydrophobicity, hydrophobe type and location as design para," *Chem. Biol. Drug Des.*, vol. 77, pp. 225–40, Apr. 2011.

[59] Z. Jiang, A. I. Vasil, M. L. Vasil, and R. S. Hodges, """Specificity Determinants" Improve Therapeutic Indices of Two Antimicrobial Peptides Piscidin 1 and Dermaseptin S4 Against the Gram-negative Pathogens Acinetobacter baumannii and Pseudomonas aeruginosa.," *Pharmaceuticals (Basel).*, vol. 7, pp. 366–91, Jan. 2014.

[60] C. Falciani, L. Lozzi, S. Pollini, V. Luca, V. Carnicelli, J. Brunetti, B. Lelli, S. Bindi, S. Scali, A. Di Giulio, G. M. Rossolini, M. L. Mangoni, L. Bracci, and A. Pini, "Isomerization of an Antimicrobial Peptide Broadens Antimicrobial Spectrum to Gram-Positive Bacterial Pathogens," *Plos One*, vol. 7, no. 10, pp. 1–8, 2012.

[61] R. Gupta and S. Srivastava, "Antifungal effect of antimicrobial peptides (AMPs LR14) derived from Lactobacillus plantarum strain LR/14 and their applications in prevention of grain spoilage," *Food Microbiol.*, vol. 42, pp. 1–7, 2014.

[62] V. Carter, A. Underhill, I. Baber, L. Sylla, M. Baby, I. Larget-Thiery, A. Zettor, C. Bourgouin, U. L. Langel, I. Faye, L. Otvos, J. D. Wade, M. B. Coulibaly, S. F. Traore, F. Tripet, P. Eggleston, and H. Hurd, "Killer Bee Molecules: Antimicrobial Peptides as Effector Molecules to Target Sporogonic Stages of Plasmodium," *Plos Pathog.*, vol. 9, no. 11, pp. 1–13, 2013.

[63] M. Wachinger, A. Kleinschmidt, D. Winder, N. von Pechmann, A. Ludvigsen, M. Neumann, R. Holle, B. Salmons, V. Erfle, and R. Brack-Werner, "Antimicrobial peptides melittin and cecropin inhibit replication of human immunodeficiency virus 1 by suppressing viral gene expression.," *J. Gen. Virol.*, vol. 79 (Pt 4), pp. 731–40, Apr. 1998.

[64] G. Wang, K. M. Watson, and R. W. Buckheit, "Anti-human immunodeficiency virus type 1 activities of antimicrobial peptides derived from human and bovine cathelicidins.," *Antimicrob. Agents Ch.*, vol. 52, pp. 3438–3440, 2008.

[65] S. Al-Benna, Y. Shai, F. Jacobsen, and L. Steinstraesser, "Oncolytic activities of host defense peptides.," *Int. J. Mol. Sci.*, vol. 12, pp. 8027–51, Jan. 2011.

[66] W.-t. Chang, C.-y. Pan, V. Rajanbabu, C.-w. Cheng, and J.-y. Chen, "Tilapia (Oreochromis mossambicus) antimicrobial peptide, hepcidin 1-5, shows antitumor activity in cancer cells.," *Peptides*, vol. 32, pp. 342–52, Feb. 2011.

[67] D. Ausbacher, G. Svineng, T. Hansen, and M. B. Strøm, "Anticancer mechanisms of action of two small amphipathic β(2,2)-amino acid derivatives derived from antimicrobial peptides.," *Biochim. Biophys. Acta*, vol. 1818, pp. 2917–25, Nov. 2012.

[68] S. Ji, W. Li, L. Zhang, Y. Zhang, and B. Cao, "Cecropin A-melittin mutant with improved proteolytic stability and enhanced antimicrobial activity against bacteria and fungi associated with gastroenteritis in vitro," *Biochem. Biophys. Res. Commun.*, vol. 451, no. 4, pp. 650–655, 2014.

[69] B. Christensen, J. Fink, R. B. Merrifield, and D. Mauzerall, "Channel-forming properties of cecropins and related model compounds incorporated into planar lipid membranes.," *Proc. Natl. Acad. Sci.*, vol. 85, no. 14, pp. 5072–5076, 1988.

[70] L. Silvestro, K. Gupta, J. N. Weiser, and P. H. Axelsen, "The concentration-dependent membrane activity of cecropin A," *Biochemistry*, vol. 36, no. 38, pp. 11452–11460, 1997.

[71] H. Raghuraman and A. Chattopadhyay, "Melittin: A membrane-active peptide with diverse functions," *Biosci. Rep.*, vol. 27, no. 4-5, pp. 189–223, 2007.

[72] S. A. Klotz, N. K. Gaur, J. Rauceo, F. Douglas, Y. Park, K. S. Hahm, P. N. Lipke, and D. F. Lake, "Inhibition of Adherence and Killing of Candida albicans with a 23-Mer Peptide (Fn / 23) with Dual Antifungal Properties Inhibition of Adherence and Killing of Candida albicans with a 23-Mer Peptide (Fn / 23) with Dual Antifungal Properties," *Society*, vol. 48, no. 11, pp. 4337–4341, 2004.

[73] V. Lazarev, T. Parfenova, S. Gularyan, O. Misyurina, T. Akopian, and V. Govorun, "Induced expression of melittin, an antimicrobial peptide, inhibits infection by Chlamydia trachomatis and Mycoplasma hominis in a HeLa cell line," *Int. J. Antimicrob. Agents*, vol. 19, pp. 133–137, feb 2002.

[74] J. H. Choi, A. Y. Jang, S. Lin, S. Lim, D. Kim, K. Park, S. M. Han, J. H. Yeo, and H. S. Seo, "Melittin, a honeybee venom-derived antimicrobial peptide, may target methicillin-resistant Staphylococcus aureus," *Mol. Med. Rep.*, vol. 12, no. 5, pp. 6483–6490, 2015.

[75] G. Gajski and V. Garaj-Vrhovac, "Melittin: A lytic peptide with anticancer properties," *Environ. Toxicol. Pharmacol.*, vol. 36, no. 2, pp. 697–705, 2013.

[76] H. Boman, D. Wade, I. Boman, B. Wåhlin, and R. Merrifield, "Antibacterial and antimalarial properties of peptides that are cecropin-melittin hybrids," *Febs Lett.*, vol. 259, pp. 103–106, Dec. 1989.

[77] J. M. Saugar, M. J. Rodriguez-Hernandez, B. G. de la Torre, M. E. Pachon-Ibanez, M. Fernandez-Reyes, D. Andreu, J. Pachon, and L. Rivas, "Activity of Cecropin A-Melittin Hybrid Peptides against Colistin-Resistant Clinical Strains of Acinetobacter baumannii: Molecular Basis for the Differential Mechanisms of Action," *Antimicrob. Agents Chemother.*, vol. 50, pp. 1251–1256, apr 2006.

[78] S. Ji, W. Li, A. R. Baloch, M. Wang, H. Li, B. Cao, and H. Zhang, "Efficient biosynthesis of a Cecropin A-melittin mutant in Bacillus subtilis WB700," *Sci. Rep.*, vol. 7, no. January, p. 40587, 2017.

[79] U. H. Dürr, U. Sudheendra, and A. Ramamoorthy, "LL-37, the only human member of the cathelicidin family of antimicrobial peptides," *Biochim. Biophys. Acta - Biomembr.*, vol. 1758, no. 9, pp. 1408–1425, 2006.

[80] J. Wiesner and A. Vilcinskas, "Antimicrobial peptides: The ancient arm of the human immune system," *Virulence*, vol. 1, pp. 440–464, sep 2010.

[81] D. Vandamme, B. Landuyt, W. Luyten, and L. Schoofs, "A comprehensive summary of LL-37, the factotum human cathelicidin peptide," *Cell. Immunol.*, vol. 280, no. 1, pp. 22–35, 2012.

[82] J. Turner, Y. Cho, N.-n. Dinh, J. Alan, R. I. Lehrer, and A. J. Waring, "Activities of LL-37 , a Cathelin-Associated Antimicrobial Peptide of Human Neutrophils Activities of LL-37 , a Cathelin-Associated Antimicrobial Peptide of Human Neutrophils," vol. 42, no. 9, pp. 2206–2214, 1998.

[83] K. Hase, M. Murakami, M. Iimura, S. P. Cole, Y. Horibe, T. Ohtake, M. Obonyo, R. L. Gallo, L. Eckmann, and M. F. Kagnoff, "Expression of LL-37 by Human Gastric Epithelial Cells as a Potential Host Defense Mechanism Against Helicobacter pylori," *Gastroenterology*, vol. 125, no. 6, pp. 1613–1625, 2003.

[84] M. D. Howell, J. F. Jones, K. O. Kisich, J. E. Streib, R. L. Gallo, and D. Y. M. Leung, "Selective killing of vaccinia virus by LL-37: implications for eczema vaccinatum.," *J. Immunol.*, vol. 172, no. 3, pp. 1763–1767, 2004.

[85] R. Koczulla, G. V. Degenfeld, C. Kupatt, F. Krötz, S. Zahler, T. Gloe, K. Issbrücker, P. Unterberger, M. Zaiou, C. Lebherz, A. Karl, P. Raake, A. Pfosser, P. Boekstegers, U. Welsch, P. S. Hiemstra, C. Vogelmeier, R. L. Gallo, M. Clauss, and R. Bals, "An angiogenic role for the human peptide antibiotic LL-37 / hCAP-18," *J. Clin. Investig.*, vol. 111, no. 11, pp. 1665–1672, 2003.

[86] R. Ramos, J. P. Silva, A. C. Rodrigues, R. Costa, L. Guardão, F. Schmitt, R. Soares, M. Vilanova, L. Domingues, and M. Gama, "Wound healing activity of the human antimicrobial peptide LL37," *Peptides*, vol. 32, pp. 1469–1476, jul 2011.

[87] A. Grönberg, M. Mahlapuu, M. Ståhle, C. Whately-Smith, and O. Rollman, "Treatment with LL-37 is safe and effective in enhancing healing of hard-to-heal venous leg ulcers: a randomized, placebo-controlled clinical trial," *Wound Repair Regen.*, vol. 22, no. 5, pp. 613–621, 2014.

[88] T. Sreeprasad and T. Pradeep, "Noble Metal Nanoparticles," in *Springer Handbook of Nanomaterials* (R. Vajtai, ed.), pp. 303–388, Springer Berlin Heidelberg, 2013.

[89] P. K. Jain, X. Huang, I. H. El-Sayed, and M. a. El-Sayed, "Noble metals on the nanoscale: optical and photothermal properties and some applications in imaging, sensing, biology, and medicine.," *Accounts Chem. Res.*, vol. 41, pp. 1578–86, Dec. 2008.

[90] K. K. Sandhu, C. M. McIntosh, J. M. Simard, S. W. Smith, and V. M. Rotello, "Gold nanoparticle-mediated transfection of mammalian cells.," *Bioconjugate Chem.*, vol. 13, no. 1, pp. 3–6, 2002.

[91] P. K. Jain, I. H. El-Sayed, and M. A. El-Sayed, "Au nanoparticles target cancer," *Nano Today*, vol. 2, pp. 18–29, Feb. 2007.

[92] H. H. Lara, E. N. Garza-Treviño, L. Ixtepan-Turrent, and D. K. Singh, "Silver nanoparticles are broad-spectrum bactericidal and virucidal compounds.," *J. Nanobiotechnology*, vol. 9, no. 1, p. 30, 2011.

[93] H. H. Lara, N. V. Ayala-Nuñez, L. Ixtepan-Turrent, and C. Rodriguez-Padilla, "Mode of antiviral action of silver nanoparticles against HIV-1.," *J. Nanobiotechnology*, vol. 8, p. 1, Jan. 2010.

[94] K. F. Soto, A. Carrasco, T. G. Powell, K. M. Garza, and L. E. Murr, "Comparative in vitro cytotoxicity assessment of some manufacturednanoparticulate materials characterized by transmissionelectron microscopy," *J. Nanoparticle Res.*, vol. 7, pp. 145–169, June 2005.

[95] S. M. Hussain, K. L. Hess, J. M. Gearhart, K. T. Geiss, and J. J. Schlager, "In vitro toxicity of nanoparticles in BRL 3A rat liver cells.," *Toxicol. In. Vitro*, vol. 19, pp. 975–83, Oct. 2005.

[96] R. Foldbjerg, D. A. Dang, and H. Autrup, "Cytotoxicity and genotoxicity of silver nanoparticles in the human lung cancer cell line, A549.," *Arch. Toxicol.*, vol. 85, pp. 743–50, July 2011.

[97] Z.-m. Xiu, Q.-b. Zhang, H. L. Puppala, V. L. Colvin, and P. J. J. Alvarez, "Negligible particle-specific antibacterial activity of silver nanoparticles.," *Nano Lett.*, vol. 12, pp. 4271–5, Aug. 2012.

[98] E. Boisselier and D. Astruc, "Gold nanoparticles in nanomedicine: preparations, imaging, diagnostics, therapies and toxicity.," *Chem. Soc. Rev.*, vol. 38, no. 6, pp. 1759–1782, 2009.

[99] M. M. Hussain, T. M. Samir, and H. M. E. Azzazy, "Unmodified gold nanoparticles for direct and rapid detection of Mycobacterium tuberculosis complex.," *Clin. Biochem.*, vol. 46, pp. 633–7, May 2013.

[100] Y. Pan, S. Neuss, A. Leifert, M. Fischler, F. Wen, U. Simon, G. Schmid, W. Brandau, and W. Jahnen-Dechent, "Size-dependent cytotoxicity of gold nanoparticles," *Small*, vol. 3, pp. 1941–1949, 2007.

[101] C. A. Simpson, K. J. Salleng, D. E. Cliffel, and D. L. Feldheim, "In vivo toxicity, biodistribution, and clearance of glutathione-coated gold nanoparticles.," *Nanomedicine-uk.*, vol. 9, pp. 257–63, Mar. 2013.

[102] C. a. Simpson, B. J. Huffman, A. E. Gerdon, and D. E. Cliffel, "Unexpected toxicity of monolayer protected gold clusters eliminated by PEG-thiol place exchange reactions.," *Chem. Res. Toxicol.*, vol. 23, pp. 1608–16, Oct. 2010.

[103] J. S. Bozich, S. E. Lohse, M. D. Torelli, C. J. Murphy, R. J. Hamers, and R. D. Klaper, "Surface chemistry, charge and ligand type impact the toxicity of gold nanoparticles to Daphnia magna," *Environ. Sci. Nano*, vol. 1, no. 3, p. 260, 2014.

[104] C. M. Goodman, C. D. McCusker, T. Yilmaz, and V. M. Rotello, "Toxicity of gold nanoparticles functionalized with cationic and anionic side chains.," *Bioconjugate Chem.*, vol. 15, no. 4, pp. 897–900, 2004.

[105] N. Lewinski, V. Colvin, and R. Drezek, "Cytotoxicity of nanoparticles.," *Small*, vol. 4, pp. 26–49, Jan. 2008.

[106] A. M. El Badawy, R. G. Silva, B. Morris, K. G. Scheckel, M. T. Suidan, and T. M. Tolaymat, "Surface charge-dependent toxicity of silver nanoparticles.," *Environ. Sci. Technol.*, vol. 45, pp. 283–7, Jan. 2011.

[107] O. Bar-Ilan, R. M. Albrecht, V. E. Fako, and D. Y. Furgeson, "Toxicity assessments of multisized gold and silver nanoparticles in zebrafish embryos.," *Small*, vol. 5, pp. 1897–910, Aug. 2009.

[108] Y.-S. Chen, Y.-C. Hung, I. Liau, and G. S. Huang, "Assessment of the In Vivo Toxicity of Gold Nanoparticles.," *Nanoscale Res. Lett.*, vol. 4, pp. 858–864, Jan. 2009.

[109] A. E. Nel, L. Mädler, D. Velegol, T. Xia, E. M. V. Hoek, P. Somasundaran, F. Klaessig, V. Castranova, and M. Thompson, "Understanding biophysicochemical interactions at the nano-bio interface.," *Nat. Mater.*, vol. 8, pp. 543–57, July 2009.

[110] A. Albanese, P. S. Tang, and W. C. Chan, "The Effect of Nanoparticle Size, Shape, and Surface Chemistry on Biological Systems," *Annu. Rev. Biomed. Eng.*, vol. 14, pp. 1–16, 2012.

[111] S. B. Lovern and R. Klaper, "Daphnia magna mortality when exposed to titanium dioxide and fullerene (C60) nanoparticles.," *Environ. Toxicol. Chem.*, vol. 25, no. 4, pp. 1132–1137, 2006.

[112] A. Albanese and W. C. W. Chan, "Effect of gold nanoparticle aggregation on cell uptake and toxicity.," *Acs Nano*, vol. 5, pp. 5478–89, July 2011.

[113] R. M. Crist, J. H. Grossman, A. K. Patri, S. T. Stern, M. a. Dobrovolskaia, P. P. Adiseshaiah, J. D. Clogston, and S. E. McNeil, "Common pitfalls in nanotechnology: lessons learned from NCI's Nanotechnology Characterization Laboratory.," *Integr. Biol. (Camb).*, vol. 5, pp. 66–73, Jan. 2013.

[114] E. E. Connor, J. Mwamuka, A. Gole, C. J. Murphy, and M. D. Wyatt, "Gold nanoparticles are taken up by human cells but do not cause acute cytotoxicity," *Small*, vol. 1, pp. 325–327, 2005.

[115] C. J. Murphy, A. M. Gole, J. W. Stone, P. N. Sisco, A. M. Alkilany, E. C. Goldsmith, and S. C. Baxter, "Gold nanoparticles in biology: Beyond toxicity to cellular imaging," *Accounts Chem. Res.*, vol. 41, no. 12, pp. 1721–1730, 2008.

[116] J. D. Gibson, B. P. Khanal, and E. R. Zubarev, "Paclitaxel-functionalized gold nanoparticles.," *J. Am. Chem. Soc.*, vol. 129, pp. 11653–61, Sept. 2007.

[117] B. Saha, J. Bhattacharya, A. Mukherjee, A. K. Ghosh, C. R. Santra, A. K. Dasgupta, and P. Karmakar, "In Vitro Structural and Functional Evaluation of Gold Nanoparticles Conjugated Antibiotics," *Nanoscale Res. Lett.*, vol. 2, pp. 614–622, Nov. 2007.

[118] A. Nirmala Grace and K. Pandian, "Antibacterial efficacy of aminoglycosidic antibiotics protected gold nanoparticles-A brief study," *Colloids Surfaces A Physicochem. Eng. Asp.*, vol. 297, pp. 63–70, Apr. 2007.

[119] T. Serizawa, Y. Hirai, and M. Aizawa, "Novel Synthetic Route to Peptide-Capped Gold Nanoparticles," *Langmuir*, vol. 25, pp. 12229–12234, oct 2009.

[120] A. Rai, A. Prabhune, and C. C. Perry, "Antibiotic mediated synthesis of gold nanoparticles with potent antimicrobial activity and their application in antimicrobial coatings," *J. Mater. Chem.*, vol. 20, no. 32, p. 6789, 2010.

[121] A. Kumar, H. Ma, X. Zhang, K. Huang, S. Jin, J. Liu, T. Wei, W. Cao, G. Zou, and X. J. Liang, "Gold nanoparticles functionalized with therapeutic and targeted peptides for cancer treatment," *Biomaterials*, vol. 33, no. 4, pp. 1180–1189, 2012.

[122] J. Zong, S. L. Cobb, and N. R. Cameron, "Peptide-functionalized gold nanoparticles: versatile biomaterials for diagnostic and therapeutic applications," *Biomater. Sci.*, vol. 5, no. 5, pp. 872–886, 2017.

[123] C. Contini, M. Schneemilch, S. Gaisford, and N. Quirke, "Nanoparticle–membrane interactions," *J. Exp. Nanosci.*, vol. 13, pp. 62–81, jan 2018.

[124] D. E. Owens and N. A. Peppas, "Opsonization, biodistribution, and pharmacokinetics of polymeric nanoparticles," *Int. J. Pharm.*, vol. 307, no. 1, pp. 93–102, 2006.

[125] M. M. van Schooneveld, E. Vucic, R. Koole, Y. Zhou, J. Stocks, D. P. Cormode, C. Y. Tang, R. E. Gordon, K. Nicolay, A. Meijerink, Z. A. Fayad, and W. J. M. Mulder, "Improved Biocompatibility and Pharmacokinetics of Silica Nanoparticles by Means of a Lipid Coating: A Multimodality Investigation," *Nano Lett.*, vol. 8, pp. 2517–2525, aug 2008.

[126] Z. Poon, D. Chang, X. Zhao, and P. T. Hammond, "Layer-by-Layer Nanoparticles with a pH-Sheddable Layer for in Vivo Targeting of Tumor Hypoxia," *ACS Nano*, vol. 5, pp. 4284–4292, jun 2011.

[127] S. R. Abulateefeh, S. G. Spain, K. J. Thurecht, J. W. Aylott, W. C. Chan, M. C. Garnett, and C. Alexander, "Enhanced uptake of nanoparticle drug carriers via a thermoresponsive shell enhances cytotoxicity in a cancer cell line," *Biomater. Sci.*, vol. 1, no. 4, pp. 434–442, 2013.

[128] L. Shang, K. Nienhaus, and G. Nienhaus, "Engineered nanoparticles interacting with cells: size matters," *J. Nanobiotechnology*, vol. 12, no. 1, p. 5, 2014.

[129] F. Moser, G. Hildenbrand, P. Müller, A. Al Saroori, A. Biswas, M. Bach, F. Wenz, C. Cremer, N. Burger, M. R. Veldwijk, and M. Hausmann, "Cellular Uptake of Gold Nanoparticles and Their Behavior as Labels for Localization Microscopy," *Biophys. J.*, vol. 110, no. 4, pp. 947–953, 2016.

[130] S. Behzadi, V. Serpooshan, W. Tao, M. A. Hamaly, M. Y. Alkawareek, E. C. Dreaden, D. Brown, A. M. Alkilany, O. C. Farokhzad, and M. Mahmoudi, "Cellular uptake of nanoparticles: journey inside the cell," *Chem. Soc. Rev.*, vol. 46, no. 14, pp. 4218–4244, 2017.

[131] I. Fratoddi, I. Venditti, C. Cametti, and M. V. Russo, "How toxic are gold nanoparticles? The state-of-the-art," *Nano Res.*, vol. 8, no. 6, pp. 1771–1799, 2015.

[132] A. S. Poulos, D. Constantin, P. Davidson, M. Impéror-Clerc, B. Pansu, and S. Rouzière, "The interaction of charged nanoparticles at interfaces," *EPL (Europhysics Lett.*, vol. 100, p. 18002, oct 2012.

[133] T. Cedervall, I. Lynch, M. Foy, T. Berggård, S. C. Donnelly, G. Cagney, S. Linse, and K. A. Dawson, "Detailed Identification of Plasma Proteins Adsorbed on Copolymer Nanoparticles," *Angew. Chemie Int. Ed.*, vol. 46, pp. 5754–5756, jul 2007.

[134] I. Lynch and K. A. Dawson, "Protein-nanoparticle interactions," *Nano Today*, vol. 3, pp. 40–47, feb 2008.

[135] B. D. Chithrani, A. A. Ghazani, and W. C. W. Chan, "Determining the Size and Shape Dependence of Gold Nanoparticle Uptake into Mammalian Cells," *Nano Lett.*, vol. 6, pp. 662–668, apr 2006.

[136] D. Krüger, H. Fuchs, R. Rousseau, D. Marx, and M. Parrinello, "Interaction of short-chain alkane thiols and thiolates with small gold clusters: Adsorption structures and energetics," *J. Chem. Phys.*, vol. 115, no. 2001, pp. 4776–4786, 2001.

[137] S. Monti, G. Barcaro, L. Sementa, V. Carravetta, and H. Ågren, "Dynamics and self-assembly of bio-functionalized gold nanoparticles in solution: Reactive molecular dynamics simulations," *Nano Res.*, vol. 11, no. 4, pp. 1757–1767, 2018.

[138] M. Hoefling, S. Monti, S. Corni, and K. E. Gottschalk, "Interaction of β-sheet folds with a gold surface.," *Plos One*, vol. 6, p. e20925, Jan. 2011.

[139] Q. Shao and C. K. Hall, "Binding Preferences of Amino Acids for Gold Nanoparticles: A Molecular Simulation Study," *Langmuir*, vol. 32, pp. 7888–7896, aug 2016.

[140] H. Heinz, R. A. Vaia, B. L. Farmer, and R. R. Naik, "Accurate Simulation of Surfaces and Interfaces of Face-Centered Cubic Metals Using 12-6 and 9-6 Lennard-Jones Potentials," *J. Phys. Chem. C*, vol. 112, pp. 17281–17290, Nov. 2008.

[141] H. Heinz, T. J. Lin, R. Kishore Mishra, and F. S. Emami, "Thermodynamically consistent force fields for the assembly of inorganic, organic, and biological nanostructures: The INTERFACE force field," *Langmuir*, vol. 29, pp. 1754–1765, 2013.

[142] H. Heinz, "Computational screening of biomolecular adsorption and self-assembly on nanoscale surfaces.," *J. Comput. Chem.*, vol. 31, pp. 1564–8, may 2010.

[143] J. Feng, R. B. Pandey, R. J. Berry, B. L. Farmer, R. R. Naik, and H. Heinz, "Adsorption mechanism of single amino acid and surfactant molecules to Au {111} surfaces in aqueous solution: design rules for metal-binding molecules," *Soft Matter*, vol. 7, no. 5, p. 2113, 2011.

[144] H. Grönbeck, A. Curioni, and W. Andreoni, “Thiols and Disulfides on the Au(111) Surface: The Headgroup-Gold Interaction,” *J. Am. Chem. Soc.*, vol. 122, pp. 3839–3842, Apr. 2000.

[145] W. Andreoni, A. Curioni, and H. Grönbeck, “Density functional theory approach to thiols and disulfides on gold: Au(111) surface and clusters,” *Int. J. Quantum Chem.*, vol. 80, no. 4-5, pp. 598–608, 2000.

[146] S. Piana and A. Bilic, “The nature of the adsorption of nucleobases on the gold [111] surface.,” *J. Phys. Chem. B*, vol. 110, pp. 23467–71, Nov. 2006.

[147] J. Lin, H. Zhang, Z. Chen, and Y. Zheng, “Penetration of lipid membranes by gold nanoparticles: insights into cellular uptake, cytotoxicity, and their relationship.,” *Acs Nano*, vol. 4, pp. 5421–9, Sept. 2010.

[148] V. Hornak, R. Abel, A. Okur, B. Strockbine, A. Roitberg, and C. Simmerling, “Comparison of multiple Amber force fields and development of improved protein backbone parameters.,” *Proteins*, vol. 65, pp. 712–25, Nov. 2006.

[149] P. Gkeka, L. Sarkisov, and P. Angelikopoulos, “Homogeneous Hydrophobic-Hydrophilic Surface Patterns Enhance Permeation of Nanoparticles through Lipid Membranes,” *J. Phys. Chem. Lett.*, vol. 4, pp. 1907–1912, jun 2013.

[150] M. Praprotnik, L. D. Site, and K. Kremer, “Multiscale simulation of soft matter: from scale bridging to adaptive resolution.,” *Annu. Rev. Phys. Chem.*, vol. 59, pp. 545–71, Jan. 2008.

[151] J. E. Stone, D. J. Hardy, I. S. Ufimtsev, and K. Schulten, “GPU-Accelerated Molecular Modeling Coming Of Age,” *J. Mol. Graph. Model.*, vol. 29, pp. 116–125, July 2010.

[152] A. W. Götz, M. J. Williamson, D. Xu, D. Poole, S. Le Grand, and R. C. Walker, “Routine Microsecond Molecular Dynamics Simulations with AMBER on GPUs. 1. Generalized Born.,” *J. Chem. Theory Comput.*, vol. 8, pp. 1542–1555, May 2012.

[153] J. Owens, M. Houston, D. Luebke, S. Green, J. Stone, and J. Phillips, “GPU Computing,” *Proc. IEEE*, vol. 96, pp. 879–899, may 2008.

[154] J. Nickolls and W. J. Dally, “The GPU Computing Era,” *IEEE Micro*, vol. 30, pp. 56–69, mar 2010.

[155] “Nvidia computational chemistry.” `http://www.nvidia.com/object/computational_chemistry.html`. Accessed: 2018-01-07.

[156] C. Kutzner, S. Páll, M. Fechner, A. Esztermann, B. L. De Groot, and H. Grubmüller, “Best bang for your buck: GPU nodes for GROMACS biomolecular simulations,” *J. Comput. Chem.*, vol. 36, no. 26, pp. 1990–2008, 2015.

[157] S. Páll, M. J. Abraham, C. Kutzner, B. Hess, and E. Lindahl, "Tackling Exascale Software Challenges in Molecular Dynamics Simulations with GROMACS," pp. 3–27, 2015.

[158] R. Zhou, "Replica exchange molecular dynamics method for protein folding simulation.," *Methods Mol. Biol.*, vol. 350, no. November, pp. 205–223, 2007.

[159] A. Barducci, M. Bonomi, and M. Parrinello, "Metadynamics," *Wiley Interdiscip. Rev. Comput. Mol. Sci.*, vol. 1, no. 5, pp. 826–843, 2011.

[160] C. Oostenbrink, A. Villa, A. E. Mark, and W. F. van Gunsteren, "A biomolecular force field based on the free enthalpy of hydration and solvation: the GROMOS force-field parameter sets 53A5 and 53A6.," *J. Comput. Chem.*, vol. 25, pp. 1656–76, Oct. 2004.

[161] T. J. Barth, M. Griebel, D. E. Keyes, R. M. Nieminen, D. Roose, and T. Schlick, *Numerical Simulation in Molecular Dynamics*. Berlin: Springer-Verlag, 2007.

[162] A. Leach, *Molecular modelling: principles and applications*. Addison-Wesley Longman Ltd, 2001.

[163] M. P. Allen, *Introduction to Molecular Dynamics Simulation*, vol. 23. Julich: NIC Series, 2004.

[164] PumMa, "Pumma molecular dynamics." [Online] http://cbio.bmt.tue.nl/ pumma/index.php/Theory/Potentials#Dihedral. 04/02/2014.

[165] T. a. Soares, X. Daura, C. Oostenbrink, L. J. Smith, and W. F. van Gunsteren, "Validation of the GROMOS force-field parameter set 45A3 against nuclear magnetic resonance data of hen egg lysozyme.," *J. Biomol. Nmr*, vol. 30, pp. 407–22, Dec. 2004.

[166] R. D. Lins and P. H. Hünenberger, "A new GROMOS force field for hexopyranose-based carbohydrates.," *J. Comput. Chem.*, vol. 26, pp. 1400–12, Oct. 2005.

[167] C. Oostenbrink, T. A. Soares, N. F. A. van Der Vegt, and W. F. van Gunsteren, "Validation of the 53A6 GROMOS force field.," *European biophysics journal : EBJ*, vol. 34, pp. 273–84, June 2005.

[168] T. a. Soares, P. H. Hünenberger, M. a. Kastenholz, V. Kräutler, T. Lenz, R. D. Lins, C. Oostenbrink, and W. F. van Gunsteren, "An improved nucleic acid parameter set for the GROMOS force field.," *J. Comput. Chem.*, vol. 26, pp. 725–37, May 2005.

[169] B. Jayaram, D. Sprous, and D. L. Beveridge, "Solvation Free Energy of Biomacromolecules: Parameters for a Modified Generalized Born Model Consistent with the AMBER Force Field," *J. Phys. Chem. B*, vol. 102, pp. 9571–9576, Nov. 1998.

[170] J. Wang, R. M. Wolf, J. W. Caldwell, P. a. Kollman, and D. a. Case, "Development and testing of a general amber force field.," *J. Comput. Chem.*, vol. 25, pp. 1157–74, July 2004.

[171] S. Patel and C. L. Brooks, "CHARMM fluctuating charge force field for proteins: I parameterization and application to bulk organic liquid simulations.," *J. Comput. Chem.*, vol. 25, pp. 1–15, Jan. 2004.

[172] S. Patel, A. D. Mackerell, and C. L. Brooks, "CHARMM fluctuating charge force field for proteins: II protein/solvent properties from molecular dynamics simulations using a nonadditive electrostatic model.," *J. Comput. Chem.*, vol. 25, pp. 1504–14, Sept. 2004.

[173] W. L. Jorgensen and J. Tirado-Rives, "The OPLS [optimized potentials for liquid simulations] potential functions for proteins, energy minimizations for crystals of cyclic peptides and crambin," *J. Am. Chem. Soc.*, vol. 110, pp. 1657–1666, Mar. 1988.

[174] W. L. Jorgensen, D. S. Maxwell, and J. Tirado-Rives, "Development and Testing of the OPLS All-Atom Force Field on Conformational Energetics and Properties of Organic Liquids," *J. Am. Chem. Soc.*, vol. 118, pp. 11225–11236, Jan. 1996.

[175] A. K. Malde, L. Zuo, M. Breeze, M. Stroet, D. Poger, P. C. Nair, C. Oostenbrink, and A. E. Mark, "An Automated force field Topology Builder (ATB) and repository: version 1.0," *J. Chem. Theory Comput.*, p. 111027125018002, Oct. 2011.

[176] A. W. Schüttelkopf and D. M. F. van Aalten, "PRODRG : a tool for high-throughput crystallography of protein-ligand complexes," *Acta Crystallogr. Sect. D Biol. Crystallogr.*, vol. 60, pp. 1355–1363, aug 2004.

[177] V. Zoete, M. A. Cuendet, A. Grosdidier, and O. Michielin, "SwissParam: a fast force field generation tool for small organic molecules.," *J. Comput. Chem.*, vol. 32, pp. 2359–68, Aug. 2011.

[178] M. Carrion-Vazquez, A. F. Oberhauser, S. B. Fowler, P. E. Marszalek, S. E. Broedel, J. Clarke, and J. M. Fernandez, "Mechanical and chemical unfolding of a single protein: A comparison," *Proc. Natl. Acad. Sci.*, vol. 96, pp. 3694–3699, mar 1999.

[179] R. H. Swendsen and J.-S. Wang, "Replica Monte Carlo simulation of spin glasses," 1986.

[180] Y. Sugita and Y. Okamoto, "Replica-exchange molecular dynamics method for protein folding," *Chem. Phys. Lett.*, vol. 314, no. 1-2, pp. 141–151, 1999.

[181] T. Mori, N. Miyashita, W. Im, M. Feig, and Y. Sugita, “Molecular dynamics simulations of biological membranes and membrane proteins using enhanced conformational sampling algorithms,” *Biochim. Biophys. Acta - Biomembr.*, vol. 1858, pp. 1635–1651, jul 2016.

[182] A. Laio and M. Parrinello, “Escaping Free-Energy Minima,” *Proc. Natl. Acad. Sci. U. S. A.*, vol. 99, p. 12562, 2002.

[183] A. Barducci, G. Bussi, and M. Parrinello, “Well-tempered metadynamics: A smoothly converging and tunable free-energy method,” *Phys. Rev. Lett.*, vol. 100, no. 2, pp. 1–4, 2008.

[184] P. Tiwary and M. Parrinello, “A Time-Independent Free Energy Estimator for Metadynamics,” *J. Phys. Chem. B*, vol. 119, pp. 736–742, jan 2015.

[185] H. Berendsen, “GROMACS: A message-passing parallel molecular dynamics implementation,” *Comput. Phys. Commun.*, vol. 91, pp. 43–56, Sept. 1995.

[186] E. Lindahl, B. Hess, and D. van der Spoel, “GROMACS 3.0: a package for molecular simulation and trajectory analysis,” *J. Mol. Model.*, pp. 306–317, 2001.

[187] D. Van Der Spoel, E. Lindahl, B. Hess, G. Groenhof, A. E. Mark, and H. J. C. Berendsen, “GROMACS: fast, flexible, and free.,” *J. Comput. Chem.*, vol. 26, pp. 1701–18, Dec. 2005.

[188] B. Hess, C. Kutzner, D. van der Spoel, and E. Lindahl, “GROMACS 4: Algorithms for Highly Efficient, Load-Balanced, and Scalable Molecular Simulation,” *J. Chem. Theory Comput.*, vol. 4, pp. 435–447, Mar. 2008.

[189] M. J. Abraham, T. Murtola, R. Schulz, S. Páll, J. C. Smith, B. Hess, and E. Lindahl, “GROMACS: High performance molecular simulations through multi-level parallelism from laptops to supercomputers,” *SoftwareX*, vol. 1-2, pp. 19–25, sep 2015.

[190] G. A. Tribello, M. Bonomi, D. Branduardi, C. Camilloni, and G. Bussi, “PLUMED 2: New feathers for an old bird,” *Comput. Phys. Commun.*, vol. 185, no. 2, pp. 604–613, 2014.

[191] “Plumed.org.” `http://www.plumed.org/`. Accessed: 2018-01-07.

[192] G. Lukat, J. Krüger, and B. Sommer, “APL@Voro: A Voronoi-Based Membrane Analysis Tool for GROMACS Trajectories,” *J. Chem. Inf. Model.*, vol. 53, no. 11, pp. 2908–2925, 2013.

[193] W. Humphrey, a. Dalke, and K. Schulten, “VMD: visual molecular dynamics.,” *J. Mol. Graphics*, vol. 14, pp. 33–8, 27–8, Feb. 1996.

[194] MATLAB, *version 8.5.0 (R2015a)*. Natick, Massachusetts: The MathWorks Inc., 2015.

[195] W. L. Jorgensen, J. Chandrasekhar, J. D. Madura, R. W. Impey, and M. L. Klein, "Comparison of simple potential functions for simulating liquid water," *J. Chem. Phys.*, vol. 79, no. 2, p. 926, 1983.

[196] J. P. M. Jämbeck and A. P. Lyubartsev, "An Extension and Further Validation of an All-Atomistic Force Field for Biological Membranes," *J. Chem. Theory Comput.*, vol. 8, pp. 2938–2948, aug 2012.

[197] J. P. M. Jämbeck and A. P. Lyubartsev, "Another piece of the membrane puzzle: Extending slipids further," *J. Chem. Theory Comput.*, vol. 9, no. 1, pp. 774–784, 2013.

[198] M. Ponec, A. Weerheim, J. Kempenaar, A. M. Mommaas, and D. H. Nugteren, "Lipid composition of cultured human keratinocytes in relation to their differentiation.," *J. Lipid Res.*, vol. 29, pp. 949–61, jul 1988.

[199] D. J. Evans and B. L. Holian, "The Nose-Hoover thermostat," *J. Chem. Phys.*, vol. 83, no. 8, p. 4069, 1985.

[200] U. Essmann, L. Perera, M. L. Berkowitz, T. Darden, H. Lee, and L. G. Pedersen, "A smooth particle mesh Ewald method," *J. Chem. Phys.*, vol. 103, no. 19, p. 8577, 1995.

[201] T. Darden, D. York, and L. Pedersen, "Particle mesh Ewald: An N.log(N) method for Ewald sums in large systems," *J. Chem. Phys.*, vol. 98, no. 12, p. 10089, 1993.

[202] B. Hess, H. Bekker, H. J. C. Berendsen, and J. G. E. M. Fraaije, "LINCS: A linear constraint solver for molecular simulations," *J. Comput. Chem.*, vol. 18, pp. 1463–1472, Sept. 1997.

[203] B. Hess, "P-LINCS: A Parallel Linear Constraint Solver for Molecular Simulation," *J. Chem. Theory Comput.*, vol. 4, pp. 116–122, Jan. 2008.

[204] D. Wade, a. Boman, B. Wåhlin, C. M. Drain, D. Andreu, H. G. Boman, and R. B. Merrifield, "All-D amino acid-containing channel-forming antibiotic peptides.," *P. Natl. Acad. Sci. Usa.*, vol. 87, no. 12, pp. 4761–4765, 1990.

[205] M. Y. Lobanov, N. S. Bogatyreva, and O. V. Galzitskaya, "Radius of gyration as an indicator of protein structure compactness," *Mol. Biol*+.+, vol. 42, no. 4, pp. 623–628, 2008.

[206] R. Galindo-Murillo, D. R. Roe, and T. E. Cheatham, "Convergence and reproducibility in molecular dynamics simulations of the DNA duplex d(GCACGAACGAACGAACGC)," *Biochim. Biophys. Acta - Gen. Subj.*, vol. 1850, pp. 1041–1058, may 2015.

[207] E. Lyman and D. M. Zuckerman, "Ensemble-Based Convergence Analysis of Biomolecular Trajectories," *Biophys. J.*, vol. 91, pp. 164–172, jul 2006.

[208] L. J. Smith, X. Daura, and W. F. van Gunsteren, "Assessing equilibration and convergence in biomolecular simulations," *Proteins Struct. Funct. Genet.*, vol. 48, pp. 487–496, aug 2002.

[209] P. I. Koukos and N. M. Glykos, "On the application of good-turing statistics to quantify convergence of biomolecular simulations," *J. Chem. Inf. Model.*, vol. 54, no. 1, pp. 209–217, 2014.

[210] K. K. Chereddy, C. H. Her, M. Comune, C. Moia, A. Lopes, P. E. Porporato, J. Vanacker, M. C. Lam, L. Steinstraesser, P. Sonveaux, H. Zhu, L. S. Ferreira, G. Vandermeulen, and V. Préat, "PLGA nanoparticles loaded with host defense peptide LL37 promote wound healing," *J. Control. Release*, vol. 194, pp. 138–147, 2014.

[211] J. Klug, C. Triguero, M. G. Del Pópolo, and G. A. Tribello, "Using Intrinsic Surfaces To Calculate the Free-Energy Change When Nanoparticles Adsorb on Membranes," *J. Phys. Chem. B*, vol. 122, pp. 6417–6422, jun 2018.

[212] A. J. Doig and M. J. E. Sternberg, "Side-chain conformational entropy in protein folding," *Protein Sci.*, vol. 4, pp. 2247–2251, nov 1995.

[213] J. Schlitter, "Estimation of absolute and relative entropies of macromolecules using the covariance matrix," *Chem. Phys. Lett.*, vol. 215, pp. 617–621, dec 1993.

[214] S. Hikiri, T. Yoshidome, and M. Ikeguchi, "Computational Methods for Configurational Entropy Using Internal and Cartesian Coordinates," *J. Chem. Theory Comput.*, vol. 12, no. 12, pp. 5990–6000, 2016.

[215] H. Schäfer, A. E. Mark, and W. F. van Gunsteren, "Absolute entropies from molecular dynamics simulation trajectories," *J. Chem. Phys.*, vol. 113, pp. 7809–7817, nov 2000.

[216] H. Schäfer, X. Daura, A. E. Mark, and W. F. van Gunsteren, "Entropy calculations on a reversibly folding peptide: Changes in solute free energy cannot explain folding behavior," *Proteins Struct. Funct. Genet.*, vol. 43, pp. 45–56, apr 2001.

[217] J. R. Allison, M. Müller, and W. F. van Gunsteren, "A comparison of the different helices adopted by α- and β-peptides suggests different reasons for their stability," *Protein Sci.*, vol. 19, pp. 2186–2195, nov 2010.

[218] D. Narzi, C. M. Becker, M. T. Fiorillo, B. Uchanska-Ziegler, A. Ziegler, and R. A. Böckmann, "Dynamical Characterization of Two Differentially Disease Associated

MHC Class I Proteins in Complex with Viral and Self-Peptides," *J. Mol. Biol.*, vol. 415, pp. 429–442, jan 2012.

[219] D. Nayar and C. Chakravarty, "Sensitivity of local hydration behaviour and conformational preferences of peptides to choice of water model," *Phys. Chem. Chem. Phys.*, vol. 16, no. 21, pp. 10199–10213, 2014.

[220] F. Eisenhaber, P. Lijnzaad, P. Argos, C. Sander, and M. Scharf, "The double cubic lattice method: Efficient approaches to numerical integration of surface area and volume and to dot surface contouring of molecular assemblies," *J. Comput. Chem.*, vol. 16, no. 3, pp. 273–284, 1995.

[221] M. Agashe, V. Raut, S. J. Stuart, and R. A. Latour, "Molecular Simulation To Characterize the Adsorption Behavior of a Fibrinogen γ-Chain Fragment," *Langmuir*, vol. 21, pp. 1103–1117, feb 2005.

[222] Z. Jiang, A. I. Vasil, J. D. Hale, R. E. W. Hancock, M. L. Vasil, and R. S. Hodges, "Effects of net charge and the number of positively charged residues on the biological activity of amphipathic α-helical cationic antimicrobial peptides," *Biopolymers*, vol. 90, no. 3, pp. 369–383, 2008.

[223] Z. Jiang, C. T. Mant, M. Vasil, and R. S. Hodges, "Role of positively charged residues on the polar and non-polar faces of amphipathic α-helical antimicrobial peptides on specificity and selectivity for Gram-negative pathogens," *Chem. Biol. Drug Des.*, vol. 91, pp. 75–92, jan 2018.

[224] H. I. Petrache, S. W. Dodd, and M. F. Brown, "Area per Lipid and Acyl Length Distributions in Fluid Phosphatidylcholines Determined by 2H NMR Spectroscopy," *Biophys. J.*, vol. 79, pp. 3172–3192, dec 2000.

[225] P. Chen, Z. Huang, J. Liang, T. Cui, X. Zhang, B. Miao, and L. T. Yan, "Diffusion and Directionality of Charged Nanoparticles on Lipid Bilayer Membrane," *ACS Nano*, vol. 10, no. 12, pp. 11541–11547, 2016.

[226] A. R. Mhashal and S. Roy, "Effect of Gold Nanoparticle on Structure and Fluidity of Lipid Membrane," *PLoS One*, vol. 9, no. 12, p. e114152, 2014.

[227] M. W. van der Kamp and A. J. Mulholland, "Combined Quantum Mechanics/-Molecular Mechanics (QM/MM) Methods in Computational Enzymology," *Biochemistry*, vol. 52, pp. 2708–2728, apr 2013.

[228] A. Omer, V. Suryanarayanan, C. Selvaraj, S. K. Singh, and P. Singh, "Explicit Drug Re-positioning," pp. 89–112, 2015.

[229] S. J. Marrink, H. J. Risselada, S. Yefimov, D. P. Tieleman, and A. H. de Vries, “The MARTINI Force Field: Coarse Grained Model for Biomolecular Simulations,” *J. Phys. Chem. B*, vol. 111, pp. 7812–7824, jul 2007.

[230] L. Monticelli, S. K. Kandasamy, X. Periole, R. G. Larson, D. P. Tieleman, and S.-J. Marrink, “The MARTINI Coarse-Grained Force Field: Extension to Proteins,” *J. Chem. Theory Comput.*, vol. 4, pp. 819–834, may 2008.

Appendix

A. MD generic worfklow

A deeper overview of the modelling and simulation processed will be presented in this section. Although GROMACS code was the selected code for the demonstration, the overall process comparable to other MD codes. The worfklow presented in figure 2.10 should be used as support for the following description.

Usually the modelling process starts with the *pdb2gmx* command. With this script GROMACS reads an external *.pdb* file (extracted for databases such as *Protein DataBank*), which contains the information about the molecule (atoms types and their coordinates), and generates a *.gro* and *.top* file. The *.gro* is just a structural rearrangement of the information in the *.pdb* file in order to GROMACS to be able to read them. Taking arginine as an example, a section of the *.pdb* and *.gro* files are presented in the listings A.1 and A.2 respectively. Despite the structural modifications, both files contain the molecule name, atom types and their coordinates (the coordinates do not match because GROMACS uses the pre-optimized structure from its database).

Listing A.1: *.pdb* file of arginine.

```
ATOM  1  N   ARG  1  14.090  20.800  11.010
ATOM  2  H1  ARG  1  14.760  20.060  11.030
ATOM  3  H2  ARG  1  14.520  21.650  11.300
ATOM  4  CA  ARG  1  13.590  20.950   9.680
...
```

Listing A.2: *.gro* file of arginine.

```
1ARG    N  1  0.214  -0.074  0.111
1ARG   H1  2  0.313  -0.070  0.104
1ARG   H2  3  0.184  -0.034  0.197
1ARG   CA  4  0.154   0.000  0.000
...
```

The *.gro* file contains information regarding the atomic coordinates, whereas the topology file (*.top*) contains all the structural and electronic information of the molecule (arginine example on listing A.3). This file is generated based on the selected force-field and includes information such as atomic mass and charge, bond length, angles, dihedrals and positional restrains if needed. In the case of investigating a system formed by more than two molecule types, solvent not included, it can be also generated a *.itp* file. This file contains the same type of information available on the *.top* file. However, since there are more that one type of molecule, it is generated a *.itp* file for each type of molecule which are then called in a main *.top* file. This simplifies a lot the process since the user can tune molecule-by- molecule instead of editing a much longer file with all the molecules.

Listing A.3: Topology file (*.top*) file of arginine.

```
[ atoms ]
;   nr       type  resnr  residue  atom   cgnr     charge       mass
     1         NL      1      ARG     N      1      −0.66    14.0067
     2          H      1      ARG    H1      1       0.44      1.008
...
[ bonds ]
;  ai    aj  funct    c0       c1
    1     2     2    0.1000   1.8700e+07
    1     3     2    0.1000   1.8700e+07
...
[ angles ]
;  ai    aj    ak  funct    c0         c1
    2     1     3     2    109.50     380.00
    2     1     4     2    109.50     425.00
...
[ dihedrals ]
;  ai    aj    ak    an  funct    c0         c1          c2
    2     1     4    17     1    0.000      3.77         3
    1     4     5     6     1    0.000      5.92         3
...
[ dihedrals ]
;  ai    aj    ak    an  funct    c0         c1
    4     1    17     5     2    35.26439   334.84617
    8     7    10     9     2    0.000000   167.42309
     ...
```

The *editconf* script only modifies the coordinate file. With this script it is possible to modify the simulation box type (cubic, rhombic dodecahedron and truncated octahedron) as well its dimension. This process should be taken very carefully since oversized boxes will lead to heavy computational load. On the other hand, small boxes can lead to artifacts created by the interaction of molecules with their mirror image. Next, there is the *genbox* command. It can be used to add solvent or to insert a number of extra molecules at random positions. Since it changes the amount and the type of molecules in the system, it needs to update both the *.top* and *.gro* files with the new data.

Before starting the simulation itself a file preprocessing is still required, and to do so the *grompp* command is used. It reads the topology (*.top*) and coordinates (*.gro*) files and check if they are consistent (i.e. check if the number and atom type match). Since the next step is the simulation, a file with the simulation options (*.mdp*) is also added as input. The *.mdp* file gathers information such as the type of calculation, energy minimization or molecular dynamics, the cut-off radius and the temperature and pressure and the algorithms used for coupling. A section of a *.mdp* file is presented in listing A.4. As output *grompp* generates a *.tpr* file which is a binary file that compiles all the information from the *.gro*, *.top* and *.mdp*.

Listing A.4: GROMACS settings file of the simulation.

```
; ELECTROSTACTIC AND VDW
coulombtype              = pme
rcoulomb                 = 1.0
```

```
vdwtype                = cut−off
rvdw                   = 1.2

; TEMPERATURE COUPLING
tcoupl                 = berendsen
tc_grps                = System
tau_t                  = 0.1
ref_t                  = 314

; PRESSURE COUPLING
pcoupl                 = berendsen
pcoupltype             = semiisotropic
tau_p                  = 2
compressibility        = 4.5e−5   4.5e−5
ref_p                  = 1.0      1.0

; BONDS
constraints            = h−bonds
constraint_algorithm   = lincs
```

In some specific cases the *.tpr* can also be used as an input to *genion* command which replaces a molecule from the created system with an ion specified by the user. If ions are added to the system, the files should be updated and *grompp* should be run again. Nonetheless, *.tpr* file is used mostly as an input for the *mdrun*.

The *mdrun* program is the main computational chemistry engine within GROMACS. It is mainly used to perform molecular dynamics simulations, but it can also perform stochastic dynamics and energy minimization. Again, the *.tpr* file with the information of the system and calculation options is provided as input and at least five output files are generated. The first one is a log file (*.log*) where information such as the current time step, the calculation time and performance is provided. A large binary file (*.trr*) with the coordinates and velocities of all the particles at each time step is also generated. If the simulated system is formed by hundreds of thousands of particles, this *.trr* file can easily grow to the order hundreds of Gb of memory per simulation. This is also one of the most relevant result from the calculation since most of the information is extracted from this file. Other important file is the *.edr* file which contains all the energy terms. The listing A.5 presents some of the data that can be extracted from the *.edr* file with the *g_energy* command (note that the options may change depending on the type of calculation). Finally, a *.gro* file with the state of the system at the end of the simulation and a checkpoint file (*.cpt*) is also generated. The checkpoint file is updated in regular intervals and can be used to resume the simulation in case of a power outage or full hard drives.

Listing A.5: Generic data that can be extracted from the *.edr* file.

```
Select the terms you want from the following list by
selecting either (part of) the name or the number or a combination.
End your selection with an empty line or a zero.
```

```
  1  G96Bond          2  G96Angle         3  Proper-Dih.      4  Improper-Dih.
  5  LJ-14            6  Coulomb-14       7  LJ-(SR)          8  LJ-(LR)
  9  Coulomb-(SR)    10  Coul.-recip.    11  Potential       12  Kinetic-En.
 13  Total-Energy    14  Temperature     15  Pressure        16  Constr.-rmsd
 17  Box-X           18  Box-Y           19  Box-Z           20  Volume
 21  Density         22  pV              23  Enthalpy        24  Vir-XX
 25  Vir-XY          26  Vir-XZ          27  Vir-YX          28  Vir-YY
 29  Vir-YZ          30  Vir-ZX          31  Vir-ZY          32  Vir-ZZ
 33  Pres-XX         34  Pres-XY         35  Pres-XZ         36  Pres-YX
 37  Pres-YY         38  Pres-YZ         39  Pres-ZX         40  Pres-ZY
 41  Pres-ZZ         42  #Surf*SurfTen   43  Mu-X            44  Mu-Y
 45  Mu-Z            46  T-System        47  Lamb-System
```

B. Cecropin melittin hybrid AMP

In this appendix is added additional information regarding the interaction of CM and CM-SH with the gold slab and AuNP.

Interaction with the Au Slab

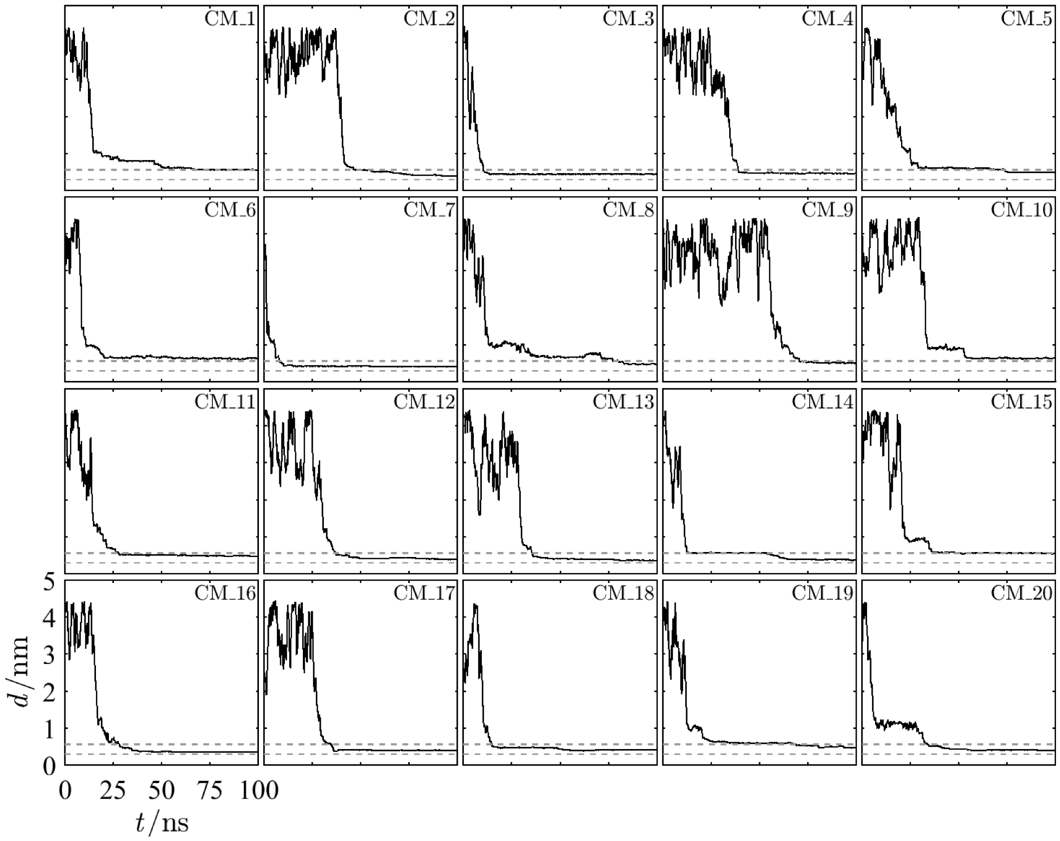

Figure B.1: Distance of the center of mass of the CM peptide to the surface. Each plot represents one simulation and its unique identifier is located on the top right. Gray dashed lines indicate the location of the water layer.

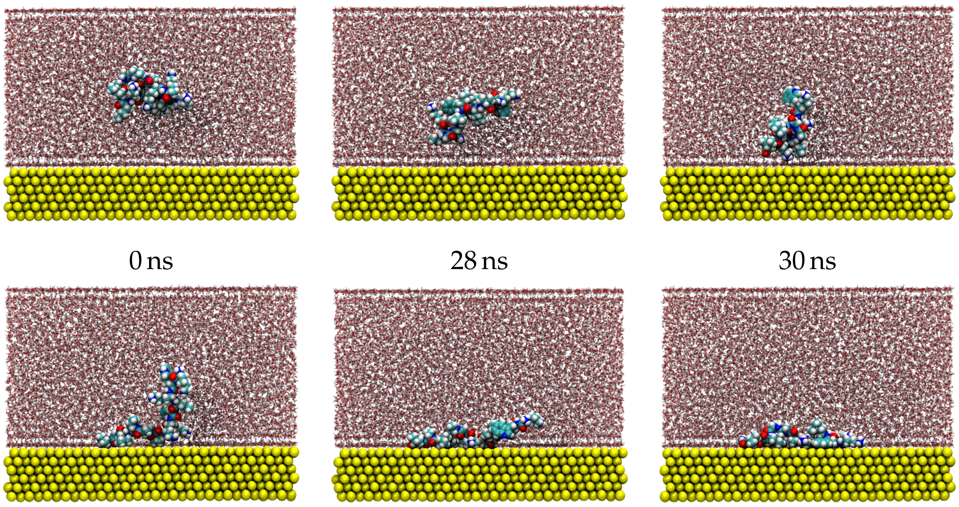

0 ns 28 ns 30 ns

33 ns 36 ns 80 ns

Figure B.2: Typical snapshots of MD trajectories for the interaction of CM with the the Au surface (system CM_13).

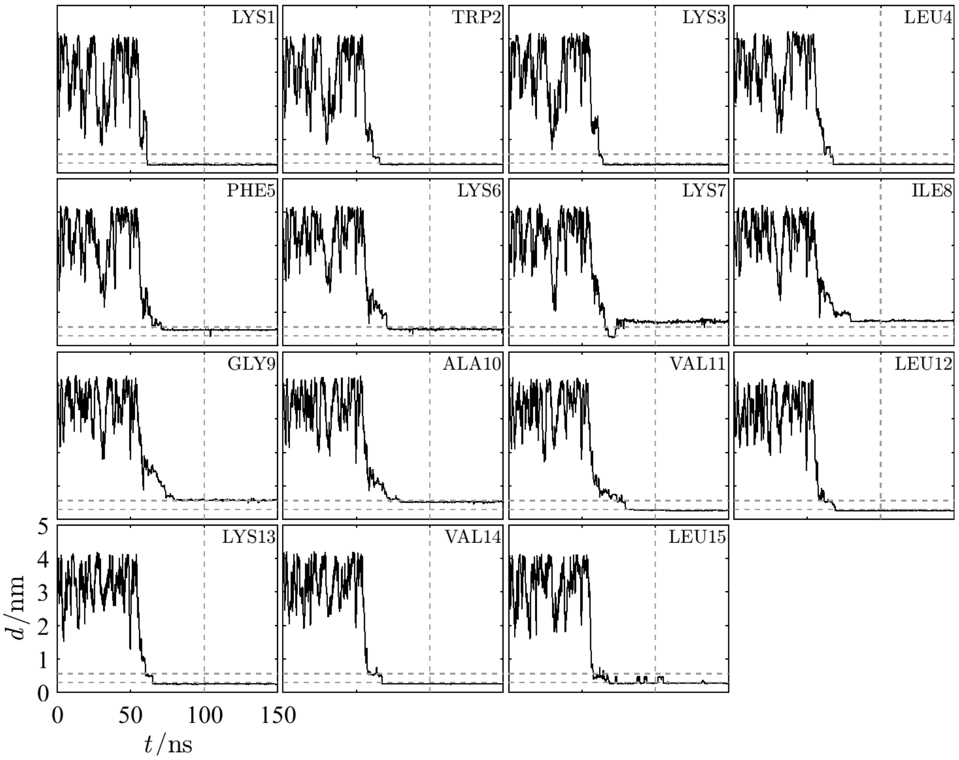

(a) CM peptide.

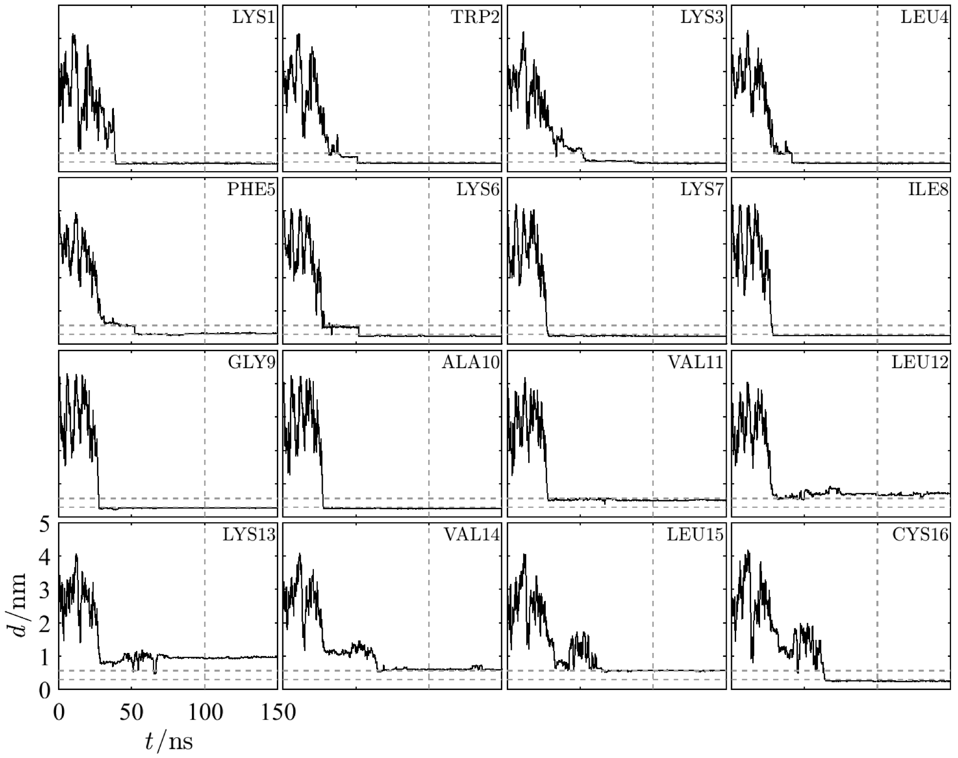

(b) CM-SH peptide.

Figure B.3: Example of two simulations extended by 50 ns (150 ns total).

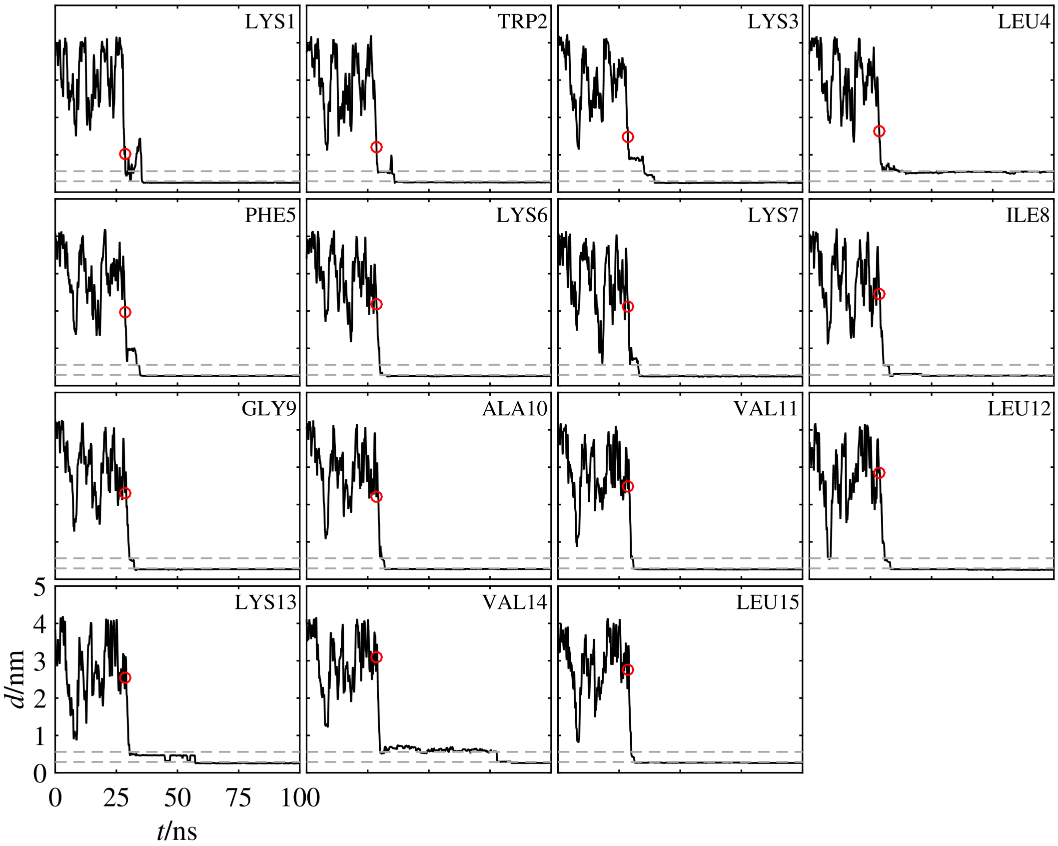

Figure B.4: Normal distance between the closest atom of each residue to the surface for the system CM_13. The red circle represents the time at which the biased diffusion regime stars. Gray dashed lines indicate the location of the water layers.

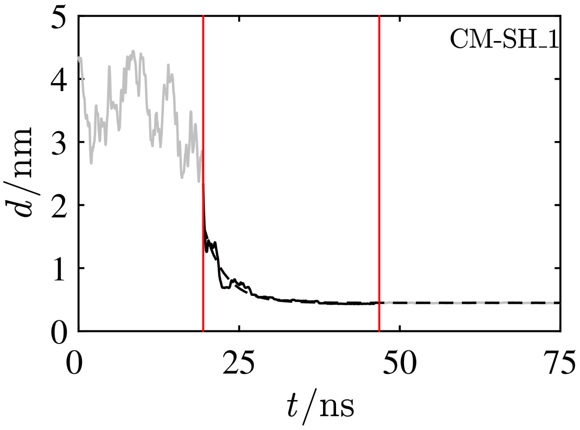

Figure B.5: Typical fitted data (normal distance between the closest atom of each residue to the surface) to the exponential decay model. Black dashed line are the fitted values, the first red line indicates the beginning of the biased diffusion and last one concerns the end of lockdown regime.

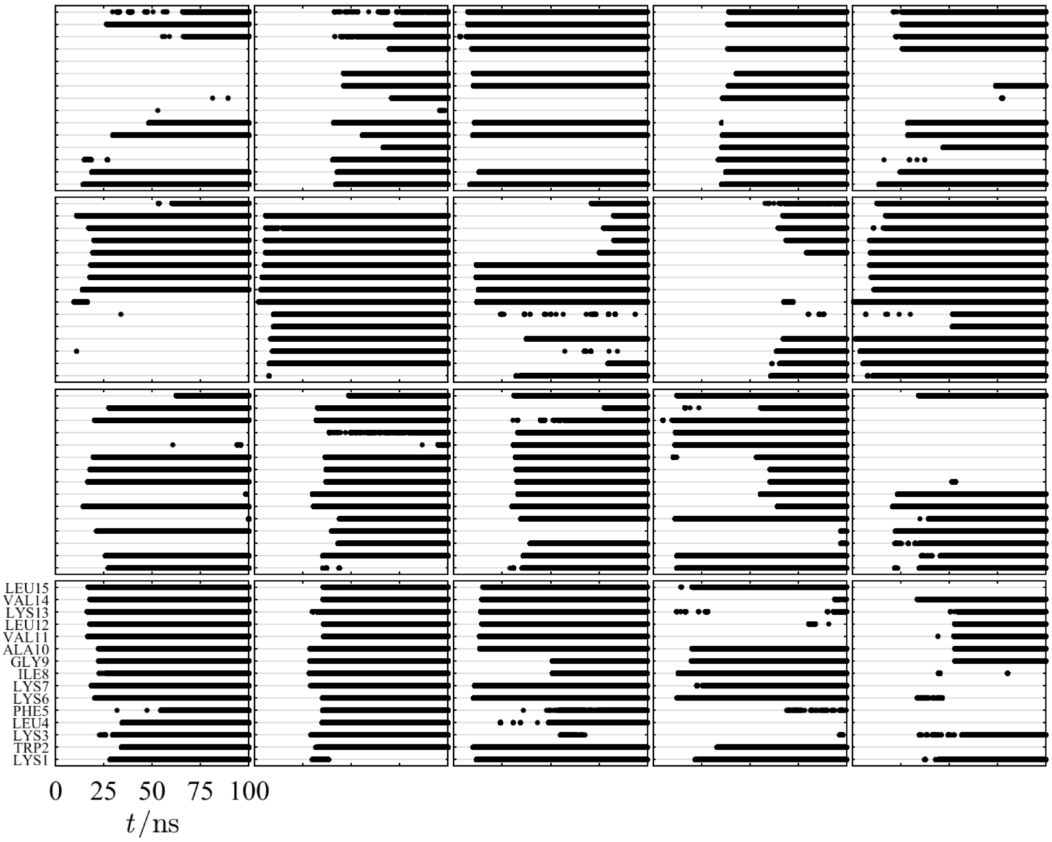

Figure B.6: Residue adsorption map for the 20 simulations on CM/Au interaction. Thick black line indicates that the residue is adsorbed. (Each plot corresponds to one simulation.)

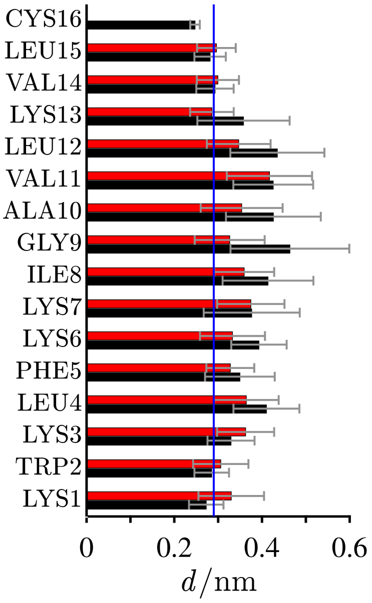

Figure B.7: Averaged distances, at the end of the simulation, of the residues to surface (CM-SH in black and CM in red).

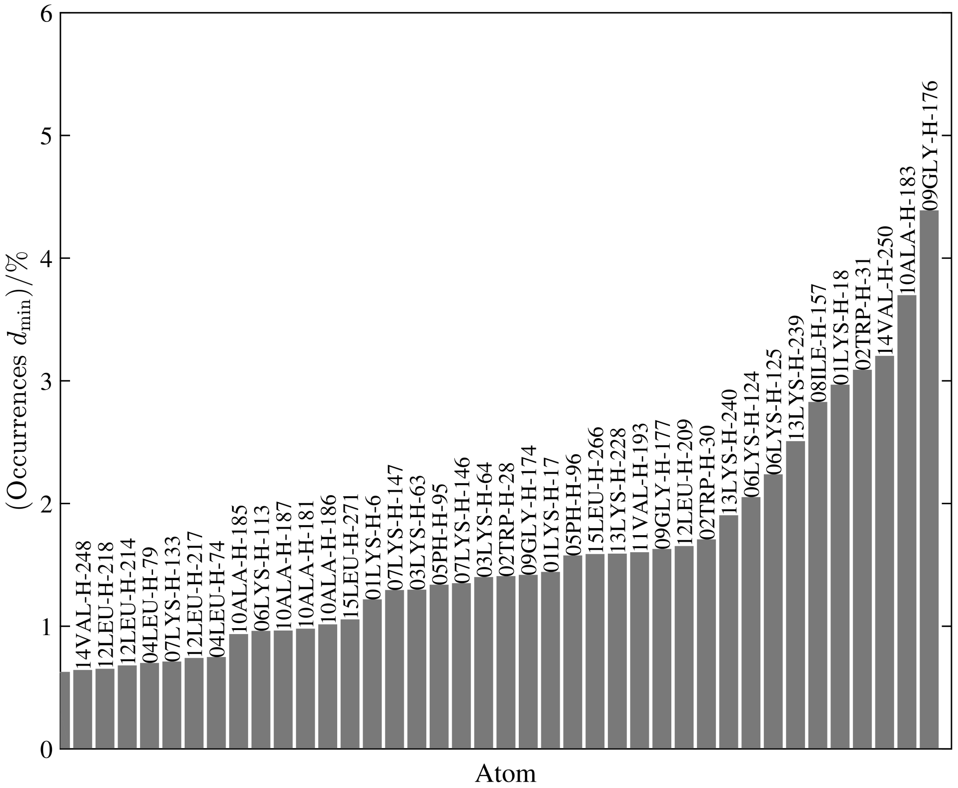

Figure B.8: Percentage of occurrences of atom at a adsorption distance ($\leq$ 0.29 nm) to the surface during all the simulation for the CM peptide. (The less populated cases are omitted for simplicity. Atom numbering can be found in the list B.2 in Appendix B.)

Listing B.1: CM-SH AMP *.pdb* file.

```
REMARK    GENERATED BY TRJCONV
TITLE     CM-SH & Gold in Water t=   0.00000
REMARK    THIS IS A SIMULATION BOX
CRYST1   77.885   89.990  103.448  90.00  90.00  90.00 P 1           1
MODEL        1
ATOM      1  N   LYS     2       4.180  33.780 100.590  1.00  0.00            N
ATOM      2  H1  LYS     2       3.740  33.630  99.690  1.00  0.00            H
ATOM      3  H2  LYS     2       4.440  34.750 100.710  1.00  0.00            H
ATOM      4  H3  LYS     2       5.060  33.290 100.560  1.00  0.00            H
ATOM      5  CA  LYS     2       3.300  33.240 101.700  1.00  0.00            C
ATOM      6  HA  LYS     2       3.910  33.300 102.600  1.00  0.00            H
ATOM      7  CB  LYS     2       2.020  34.090 101.950  1.00  0.00            C
ATOM      8  HB1 LYS     2       1.500  33.810 102.870  1.00  0.00            H
ATOM      9  HB2 LYS     2       1.330  33.810 101.150  1.00  0.00            H
ATOM     10  CG  LYS     2       2.160  35.590 102.060  1.00  0.00            C
ATOM     11  HG1 LYS     2       2.690  35.820 101.140  1.00  0.00            H
ATOM     12  HG2 LYS     2       2.810  35.840 102.900  1.00  0.00            H
ATOM     13  CD  LYS     2       0.800  36.240 102.130  1.00  0.00            C
ATOM     14  HD1 LYS     2       0.240  35.900 102.990  1.00  0.00            H
ATOM     15  HD2 LYS     2       0.180  35.880 101.300  1.00  0.00            H
ATOM     16  CE  LYS     2       0.820  37.760 102.070  1.00  0.00            C
ATOM     17  HE1 LYS     2       1.280  38.260 102.920  1.00  0.00            H
ATOM     18  HE2 LYS     2      −0.210  38.110 102.190  1.00  0.00            H
ATOM     19  NZ  LYS     2       1.340  38.360 100.800  1.00  0.00            N
```

```
ATOM   20  HZ1 LYS   2      0.720  38.150 100.040  1.00  0.00      H
ATOM   21  HZ2 LYS   2      1.450  39.370 100.850  1.00  0.00      H
ATOM   22  HZ3 LYS   2      2.250  38.000 100.570  1.00  0.00      H
ATOM   23  C   LYS   2      3.060  31.740 101.520  1.00  0.00      C
ATOM   24  O   LYS   2      3.870  30.970 101.930  1.00  0.00      O
ATOM   25  N   TRP   3      1.870  31.410 101.010  1.00  0.00      N
ATOM   26  H   TRP   3      1.310  32.090 100.520  1.00  0.00      H
ATOM   27  CA  TRP   3      1.380  30.020 100.760  1.00  0.00      C
ATOM   28  HA  TRP   3      2.240  29.390 100.520  1.00  0.00      H
ATOM   29  CB  TRP   3      0.910  29.430 102.080  1.00  0.00      C
ATOM   30  HB1 TRP   3     −0.070  29.780 102.430  1.00  0.00      H
ATOM   31  HB2 TRP   3      1.640  29.700 102.850  1.00  0.00      H
ATOM   32  CG  TRP   3      0.970  27.950 102.060  1.00  0.00      C
ATOM   33  CD1 TRP   3     −0.050  27.080 102.240  1.00  0.00      C
ATOM   34  HD1 TRP   3     −1.100  27.310 102.310  1.00  0.00      H
ATOM   35  NE1 TRP   3      0.420  25.770 102.260  1.00  0.00      N
ATOM   36  HE1 TRP   3     −0.260  25.020 102.340  1.00  0.00      H
ATOM   37  CE2 TRP   3      1.770  25.730 102.090  1.00  0.00      C
ATOM   38  CZ2 TRP   3      2.730  24.690 102.060  1.00  0.00      C
ATOM   39  HZ2 TRP   3      2.400  23.670 102.170  1.00  0.00      H
ATOM   40  CH2 TRP   3      4.110  25.020 102.040  1.00  0.00      C
ATOM   41  HH2 TRP   3      4.900  24.280 102.120  1.00  0.00      H
ATOM   42  CZ3 TRP   3      4.440  26.370 101.890  1.00  0.00      C
ATOM   43  HZ3 TRP   3      5.460  26.730 101.800  1.00  0.00      H
ATOM   44  CE3 TRP   3      3.480  27.360 101.730  1.00  0.00      C
ATOM   45  HE3 TRP   3      3.820  28.390 101.690  1.00  0.00      H
ATOM   46  CD2 TRP   3      2.100  27.100 101.850  1.00  0.00      C
ATOM   47  C   TRP   3      0.380  29.940  99.630  1.00  0.00      C
ATOM   48  O   TRP   3     −0.040  30.920  99.040  1.00  0.00      O
ATOM   49  N   LYS   4     −0.170  28.710  99.420  1.00  0.00      N
ATOM   50  H   LYS   4      0.140  28.000 100.070  1.00  0.00      H
ATOM   51  CA  LYS   4     −1.040  28.270  98.380  1.00  0.00      C
ATOM   52  HA  LYS   4     −0.780  28.870  97.500  1.00  0.00      H
ATOM   53  CB  LYS   4     −0.620  26.840  97.970  1.00  0.00      C
ATOM   54  HB1 LYS   4     −0.560  26.320  98.920  1.00  0.00      H
ATOM   55  HB2 LYS   4      0.350  26.900  97.480  1.00  0.00      H
ATOM   56  CG  LYS   4     −1.530  26.120  97.000  1.00  0.00      C
ATOM   57  HG1 LYS   4     −2.450  25.760  97.460  1.00  0.00      H
ATOM   58  HG2 LYS   4     −1.050  25.220  96.610  1.00  0.00      H
ATOM   59  CD  LYS   4     −1.930  27.000  95.810  1.00  0.00      C
ATOM   60  HD1 LYS   4     −1.070  27.630  95.580  1.00  0.00      H
ATOM   61  HD2 LYS   4     −2.780  27.630  96.100  1.00  0.00      H
ATOM   62  CE  LYS   4     −2.430  26.240  94.600  1.00  0.00      C
ATOM   63  HE1 LYS   4     −3.400  25.830  94.860  1.00  0.00      H
ATOM   64  HE2 LYS   4     −1.680  25.510  94.300  1.00  0.00      H
ATOM   65  NZ  LYS   4     −2.480  27.100  93.450  1.00  0.00      N
ATOM   66  HZ1 LYS   4     −1.570  27.210  93.020  1.00  0.00      H
ATOM   67  HZ2 LYS   4     −2.970  26.710  92.660  1.00  0.00      H
ATOM   68  HZ3 LYS   4     −2.880  28.020  93.580  1.00  0.00      H
ATOM   69  C   LYS   4     −2.520  28.530  98.720  1.00  0.00      C
ATOM   70  O   LYS   4     −3.330  27.590  98.790  1.00  0.00      O
ATOM   71  N   LEU   5     −2.870  29.770  99.010  1.00  0.00      N
ATOM   72  H   LEU   5     −2.180  30.490  98.880  1.00  0.00      H
ATOM   73  CA  LEU   5     −4.140  30.340  99.580  1.00  0.00      C
ATOM   74  HA  LEU   5     −4.650  29.560 100.160  1.00  0.00      H
ATOM   75  CB  LEU   5     −3.710  31.420 100.570  1.00  0.00      C
ATOM   76  HB1 LEU   5     −3.310  32.260 100.020  1.00  0.00      H
```

```
ATOM    77  HB2 LEU    5      −2.950  31.020 101.240  1.00  0.00           H
ATOM    78  CG  LEU    5      −4.910  31.950 101.350  1.00  0.00           C
ATOM    79  HG  LEU    5      −5.550  32.390 100.590  1.00  0.00           H
ATOM    80  CD1 LEU    5      −5.590  30.820 102.180  1.00  0.00           C
ATOM    81 1HD1 LEU    5      −6.390  31.100 102.870  1.00  0.00           H
ATOM    82 2HD1 LEU    5      −6.120  30.150 101.500  1.00  0.00           H
ATOM    83 3HD1 LEU    5      −4.840  30.220 102.690  1.00  0.00           H
ATOM    84  CD2 LEU    5      −4.480  33.000 102.360  1.00  0.00           C
ATOM    85 1HD2 LEU    5      −3.660  32.560 102.920  1.00  0.00           H
ATOM    86 2HD2 LEU    5      −4.170  33.820 101.720  1.00  0.00           H
ATOM    87 3HD2 LEU    5      −5.290  33.350 103.010  1.00  0.00           H
ATOM    88  C   LEU    5      −5.170  30.780  98.490  1.00  0.00           C
ATOM    89  O   LEU    5      −4.890  31.800  97.940  1.00  0.00           O
ATOM    90  N   PHE    6      −6.370  30.250  98.440  1.00  0.00           N
ATOM    91  H   PHE    6      −6.550  29.420  98.990  1.00  0.00           H
ATOM    92  CA  PHE    6      −7.550  30.690  97.640  1.00  0.00           C
ATOM    93  HA  PHE    6      −7.520  31.740  97.340  1.00  0.00           H
ATOM    94  CB  PHE    6      −7.570  30.020  96.210  1.00  0.00           C
ATOM    95  HB1 PHE    6      −6.730  30.400  95.640  1.00  0.00           H
ATOM    96  HB2 PHE    6      −8.420  30.440  95.670  1.00  0.00           H
ATOM    97  CG  PHE    6      −7.700  28.510  96.270  1.00  0.00           C
ATOM    98  CD1 PHE    6      −8.970  27.950  96.090  1.00  0.00           C
ATOM    99  HD1 PHE    6      −9.810  28.630  96.020  1.00  0.00           H
ATOM   100  CE1 PHE    6      −9.100  26.520  95.970  1.00  0.00           C
ATOM   101  HE1 PHE    6      −9.990  26.000  95.660  1.00  0.00           H
ATOM   102  CZ  PHE    6      −8.060  25.680  96.210  1.00  0.00           C
ATOM   103  HZ  PHE    6      −8.130  24.610  96.130  1.00  0.00           H
ATOM   104  CE2 PHE    6      −6.790  26.280  96.350  1.00  0.00           C
ATOM   105  HE2 PHE    6      −5.870  25.710  96.360  1.00  0.00           H
ATOM   106  CD2 PHE    6      −6.550  27.690  96.390  1.00  0.00           C
ATOM   107  HD2 PHE    6      −5.570  28.130  96.410  1.00  0.00           H
ATOM   108  C   PHE    6      −8.890  30.470  98.390  1.00  0.00           C
ATOM   109  O   PHE    6      −9.060  29.450  99.090  1.00  0.00           O
ATOM   110  N   LYS    7      −9.920  31.260  98.160  1.00  0.00           N
ATOM   111  H   LYS    7      −9.900  31.910  97.390  1.00  0.00           H
ATOM   112  CA  LYS    7     −11.200  30.950  98.830  1.00  0.00           C
ATOM   113  HA  LYS    7     −11.030  30.920  99.900  1.00  0.00           H
ATOM   114  CB  LYS    7     −12.140  32.170  98.490  1.00  0.00           C
ATOM   115  HB1 LYS    7     −12.360  32.120  97.420  1.00  0.00           H
ATOM   116  HB2 LYS    7     −11.630  33.130  98.580  1.00  0.00           H
ATOM   117  CG  LYS    7     −13.430  32.330  99.280  1.00  0.00           C
ATOM   118  HG1 LYS    7     −13.270  32.520 100.340  1.00  0.00           H
ATOM   119  HG2 LYS    7     −14.060  31.440  99.290  1.00  0.00           H
ATOM   120  CD  LYS    7     −14.280  33.450  98.700  1.00  0.00           C
ATOM   121  HD1 LYS    7     −14.380  33.270  97.630  1.00  0.00           H
ATOM   122  HD2 LYS    7     −13.780  34.410  98.830  1.00  0.00           H
ATOM   123  CE  LYS    7     −15.640  33.520  99.450  1.00  0.00           C
ATOM   124  HE1 LYS    7     −15.430  33.580 100.520  1.00  0.00           H
ATOM   125  HE2 LYS    7     −16.180  32.580  99.330  1.00  0.00           H
ATOM   126  NZ  LYS    7     −16.450  34.680  99.000  1.00  0.00           N
ATOM   127  HZ1 LYS    7     −15.830  35.470  99.020  1.00  0.00           H
ATOM   128  HZ2 LYS    7     −16.840  34.490  98.090  1.00  0.00           H
ATOM   129  HZ3 LYS    7     −17.160  35.000  99.650  1.00  0.00           H
ATOM   130  C   LYS    7     −11.860  29.610  98.370  1.00  0.00           C
ATOM   131  O   LYS    7     −11.970  29.400  97.120  1.00  0.00           O
ATOM   132  N   LYS    8     −12.190  28.710  99.340  1.00  0.00           N
ATOM   133  H   LYS    8     −11.750  28.940 100.220  1.00  0.00           H
```

```
ATOM   134  CA   LYS   8   -12.730  27.330   99.190  1.00  0.00   C
ATOM   135  HA   LYS   8   -11.890  26.740   98.830  1.00  0.00   H
ATOM   136  CB   LYS   8   -13.130  26.720  100.530  1.00  0.00   C
ATOM   137  HB1  LYS   8   -13.620  25.750  100.420  1.00  0.00   H
ATOM   138  HB2  LYS   8   -13.920  27.330  100.960  1.00  0.00   H
ATOM   139  CG   LYS   8   -12.120  26.600  101.650  1.00  0.00   C
ATOM   140  HG1  LYS   8   -12.730  26.400  102.530  1.00  0.00   H
ATOM   141  HG2  LYS   8   -11.500  27.490  101.770  1.00  0.00   H
ATOM   142  CD   LYS   8   -11.240  25.350  101.390  1.00  0.00   C
ATOM   143  HD1  LYS   8   -11.140  25.290  100.300  1.00  0.00   H
ATOM   144  HD2  LYS   8   -11.770  24.480  101.790  1.00  0.00   H
ATOM   145  CE   LYS   8    -9.900  25.590  102.110  1.00  0.00   C
ATOM   146  HE1  LYS   8    -9.990  25.210  103.120  1.00  0.00   H
ATOM   147  HE2  LYS   8    -9.650  26.640  102.190  1.00  0.00   H
ATOM   148  NZ   LYS   8    -8.900  24.910  101.300  1.00  0.00   N
ATOM   149  HZ1  LYS   8    -8.910  25.280  100.360  1.00  0.00   H
ATOM   150  HZ2  LYS   8    -7.960  24.940  101.670  1.00  0.00   H
ATOM   151  HZ3  LYS   8    -9.250  23.970  101.250  1.00  0.00   H
ATOM   152  C    LYS   8   -13.920  27.200   98.220  1.00  0.00   C
ATOM   153  O    LYS   8   -14.740  28.090   98.070  1.00  0.00   O
ATOM   154  N    ILE   9   -13.870  26.080   97.520  1.00  0.00   N
ATOM   155  H    ILE   9   -13.120  25.410   97.600  1.00  0.00   H
ATOM   156  CA   ILE   9   -14.830  25.760   96.380  1.00  0.00   C
ATOM   157  HA   ILE   9   -15.770  26.260   96.620  1.00  0.00   H
ATOM   158  CB   ILE   9   -14.260  26.380   95.070  1.00  0.00   C
ATOM   159  HB   ILE   9   -14.900  25.980   94.280  1.00  0.00   H
ATOM   160  CG2  ILE   9   -14.470  27.900   94.920  1.00  0.00   C
ATOM   161  1HG2 ILE   9   -14.140  28.230   93.930  1.00  0.00   H
ATOM   162  2HG2 ILE   9   -15.500  28.170   95.150  1.00  0.00   H
ATOM   163  3HG2 ILE   9   -13.740  28.310   95.620  1.00  0.00   H
ATOM   164  CG1  ILE   9   -12.770  26.090   94.860  1.00  0.00   C
ATOM   165  1HG1 ILE   9   -12.670  25.010   94.910  1.00  0.00   H
ATOM   166  2HG1 ILE   9   -12.120  26.520   95.620  1.00  0.00   H
ATOM   167  CD   ILE   9   -12.260  26.500   93.470  1.00  0.00   C
ATOM   168  HD1  ILE   9   -12.230  27.580   93.410  1.00  0.00   H
ATOM   169  HD2  ILE   9   -11.260  26.090   93.420  1.00  0.00   H
ATOM   170  HD3  ILE   9   -12.940  26.040   92.740  1.00  0.00   H
ATOM   171  C    ILE   9   -15.200  24.300   96.190  1.00  0.00   C
ATOM   172  O    ILE   9   -16.190  23.960   95.550  1.00  0.00   O
ATOM   173  N    GLY  10   -14.470  23.450   96.880  1.00  0.00   N
ATOM   174  H    GLY  10   -13.630  23.770   97.330  1.00  0.00   H
ATOM   175  CA   GLY  10   -14.710  21.970   96.890  1.00  0.00   C
ATOM   176  HA1  GLY  10   -15.010  21.600   95.910  1.00  0.00   H
ATOM   177  HA2  GLY  10   -15.510  21.820   97.620  1.00  0.00   H
ATOM   178  C    GLY  10   -13.400  21.280   97.360  1.00  0.00   C
ATOM   179  O    GLY  10   -12.400  21.940   97.570  1.00  0.00   O
ATOM   180  N    ALA  11   -13.450  19.970   97.550  1.00  0.00   N
ATOM   181  H    ALA  11   -14.330  19.570   97.260  1.00  0.00   H
ATOM   182  CA   ALA  11   -12.440  19.110   98.200  1.00  0.00   C
ATOM   183  HA   ALA  11   -12.150  19.650   99.100  1.00  0.00   H
ATOM   184  CB   ALA  11   -13.120  17.740   98.480  1.00  0.00   C
ATOM   185  HB1  ALA  11   -12.460  17.230   99.190  1.00  0.00   H
ATOM   186  HB2  ALA  11   -14.110  17.860   98.920  1.00  0.00   H
ATOM   187  HB3  ALA  11   -13.190  17.090   97.610  1.00  0.00   H
ATOM   188  C    ALA  11   -11.160  19.010   97.400  1.00  0.00   C
ATOM   189  O    ALA  11   -10.470  18.030   97.590  1.00  0.00   O
ATOM   190  N    VAL  12   -10.770  20.010   96.530  1.00  0.00   N
```

```
ATOM   191  H    VAL   12   −11.200  20.920   96.590  1.00  0.00       H
ATOM   192  CA   VAL   12    −9.580  20.030   95.620  1.00  0.00       C
ATOM   193  HA   VAL   12    −9.370  18.990   95.370  1.00  0.00       H
ATOM   194  CB   VAL   12    −9.750  20.910   94.340  1.00  0.00       C
ATOM   195  HB   VAL   12   −10.560  20.460   93.760  1.00  0.00       H
ATOM   196  CG1  VAL   12   −10.120  22.300   94.720  1.00  0.00       C
ATOM   197  1HG1 VAL   12    −9.330  22.870   95.200  1.00  0.00       H
ATOM   198  2HG1 VAL   12   −10.570  22.870   93.900  1.00  0.00       H
ATOM   199  3HG1 VAL   12   −10.930  22.310   95.440  1.00  0.00       H
ATOM   200  CG2  VAL   12    −8.530  21.100   93.410  1.00  0.00       C
ATOM   201  1HG2 VAL   12    −8.190  20.110   93.110  1.00  0.00       H
ATOM   202  2HG2 VAL   12    −8.830  21.830   92.650  1.00  0.00       H
ATOM   203  3HG2 VAL   12    −7.690  21.550   93.940  1.00  0.00       H
ATOM   204  C    VAL   12    −8.390  20.550   96.410  1.00  0.00       C
ATOM   205  O    VAL   12    −8.450  21.480   97.240  1.00  0.00       O
ATOM   206  N    LEU   13    −7.260  19.890   96.230  1.00  0.00       N
ATOM   207  H    LEU   13    −7.300  19.140   95.560  1.00  0.00       H
ATOM   208  CA   LEU   13    −5.970  20.150   96.950  1.00  0.00       C
ATOM   209  HA   LEU   13    −5.330  19.280   96.820  1.00  0.00       H
ATOM   210  CB   LEU   13    −5.180  21.320   96.250  1.00  0.00       C
ATOM   211  HB1  LEU   13    −5.650  22.290   96.410  1.00  0.00       H
ATOM   212  HB2  LEU   13    −5.210  21.160   95.170  1.00  0.00       H
ATOM   213  CG   LEU   13    −3.700  21.490   96.710  1.00  0.00       C
ATOM   214  HG   LEU   13    −3.720  21.910   97.720  1.00  0.00       H
ATOM   215  CD1  LEU   13    −2.830  20.200   96.670  1.00  0.00       C
ATOM   216  1HD1 LEU   13    −1.860  20.490   97.080  1.00  0.00       H
ATOM   217  2HD1 LEU   13    −3.280  19.390   97.240  1.00  0.00       H
ATOM   218  3HD1 LEU   13    −2.770  20.010   95.600  1.00  0.00       H
ATOM   219  CD2  LEU   13    −2.870  22.500   95.920  1.00  0.00       C
ATOM   220  1HD2 LEU   13    −1.920  22.670   96.430  1.00  0.00       H
ATOM   221  2HD2 LEU   13    −2.780  22.200   94.880  1.00  0.00       H
ATOM   222  3HD2 LEU   13    −3.400  23.450   96.010  1.00  0.00       H
ATOM   223  C    LEU   13    −6.090  20.270   98.490  1.00  0.00       C
ATOM   224  O    LEU   13    −5.380  21.010   99.140  1.00  0.00       O
ATOM   225  N    LYS   14    −7.080  19.530   99.110  1.00  0.00       N
ATOM   226  H    LYS   14    −7.700  19.010   98.510  1.00  0.00       H
ATOM   227  CA   LYS   14    −7.520  19.780  100.470  1.00  0.00       C
ATOM   228  HA   LYS   14    −7.820  20.830  100.480  1.00  0.00       H
ATOM   229  CB   LYS   14    −8.770  19.010  100.800  1.00  0.00       C
ATOM   230  HB1  LYS   14    −9.370  19.130   99.900  1.00  0.00       H
ATOM   231  HB2  LYS   14    −9.230  19.560  101.620  1.00  0.00       H
ATOM   232  CG   LYS   14    −8.650  17.550  101.280  1.00  0.00       C
ATOM   233  HG1  LYS   14    −8.160  17.480  102.250  1.00  0.00       H
ATOM   234  HG2  LYS   14    −8.030  17.000  100.570  1.00  0.00       H
ATOM   235  CD   LYS   14   −10.090  16.940  101.240  1.00  0.00       C
ATOM   236  HD1  LYS   14   −10.350  16.870  100.180  1.00  0.00       H
ATOM   237  HD2  LYS   14   −10.750  17.610  101.780  1.00  0.00       H
ATOM   238  CE   LYS   14   −10.120  15.570  101.930  1.00  0.00       C
ATOM   239  HE1  LYS   14   −10.050  15.670  103.010  1.00  0.00       H
ATOM   240  HE2  LYS   14    −9.280  14.930  101.650  1.00  0.00       H
ATOM   241  NZ   LYS   14   −11.280  14.740  101.560  1.00  0.00       N
ATOM   242  HZ1  LYS   14   −11.200  13.880  102.070  1.00  0.00       H
ATOM   243  HZ2  LYS   14   −12.130  15.270  101.670  1.00  0.00       H
ATOM   244  HZ3  LYS   14   −11.260  14.460  100.590  1.00  0.00       H
ATOM   245  C    LYS   14    −6.400  19.480  101.450  1.00  0.00       C
ATOM   246  O    LYS   14    −6.580  19.890  102.570  1.00  0.00       O
ATOM   247  N    VAL   15    −5.370  18.800  100.990  1.00  0.00       N
```

```
ATOM    248  H    VAL    15      -5.380  18.530 100.020  1.00  0.00           H
ATOM    249  CA   VAL    15      -4.210  18.310 101.820  1.00  0.00           C
ATOM    250  HA   VAL    15      -4.590  18.320 102.840  1.00  0.00           H
ATOM    251  CB   VAL    15      -3.890  16.850 101.580  1.00  0.00           C
ATOM    252  HB   VAL    15      -3.230  16.520 102.380  1.00  0.00           H
ATOM    253  CG1  VAL    15      -5.110  15.980 101.650  1.00  0.00           C
ATOM    254 1HG1  VAL    15      -5.770  16.230 102.480  1.00  0.00           H
ATOM    255 2HG1  VAL    15      -5.820  16.010 100.820  1.00  0.00           H
ATOM    256 3HG1  VAL    15      -4.890  14.910 101.680  1.00  0.00           H
ATOM    257  CG2  VAL    15      -3.040  16.590 100.300  1.00  0.00           C
ATOM    258 1HG2  VAL    15      -3.010  15.510 100.210  1.00  0.00           H
ATOM    259 2HG2  VAL    15      -3.520  17.160  99.510  1.00  0.00           H
ATOM    260 3HG2  VAL    15      -2.040  16.950 100.570  1.00  0.00           H
ATOM    261  C    VAL    15      -2.950  19.150 101.910  1.00  0.00           C
ATOM    262  O    VAL    15      -1.920  18.710 102.320  1.00  0.00           O
ATOM    263  N    LEU    16      -2.970  20.350 101.410  1.00  0.00           N
ATOM    264  H    LEU    16      -3.830  20.670 100.980  1.00  0.00           H
ATOM    265  CA   LEU    16      -1.850  21.300 101.450  1.00  0.00           C
ATOM    266  HA   LEU    16      -1.050  21.050 102.150  1.00  0.00           H
ATOM    267  CB   LEU    16      -1.210  21.160 100.050  1.00  0.00           C
ATOM    268  HB1  LEU    16      -1.950  21.350  99.270  1.00  0.00           H
ATOM    269  HB2  LEU    16      -0.900  20.110 100.060  1.00  0.00           H
ATOM    270  CG   LEU    16      -0.020  22.000  99.740  1.00  0.00           C
ATOM    271  HG   LEU    16      -0.180  23.070  99.800  1.00  0.00           H
ATOM    272  CD1  LEU    16       1.140  21.580 100.710  1.00  0.00           C
ATOM    273 1HD1  LEU    16       1.400  20.530 100.630  1.00  0.00           H
ATOM    274 2HD1  LEU    16       2.020  22.180 100.470  1.00  0.00           H
ATOM    275 3HD1  LEU    16       0.910  21.840 101.740  1.00  0.00           H
ATOM    276  CD2  LEU    16       0.500  21.730  98.390  1.00  0.00           C
ATOM    277 1HD2  LEU    16       1.300  22.420  98.130  1.00  0.00           H
ATOM    278 2HD2  LEU    16       0.800  20.680  98.470  1.00  0.00           H
ATOM    279 3HD2  LEU    16      -0.320  21.830  97.680  1.00  0.00           H
ATOM    280  C    LEU    16      -2.220  22.750 101.790  1.00  0.00           C
ATOM    281  O    LEU    16      -1.400  23.570 102.310  1.00  0.00           O
ATOM    282  N    CYS    17      -3.540  23.130 101.550  1.00  0.00           N
ATOM    283  H    CYS    17      -4.230  22.480 101.180  1.00  0.00           H
ATOM    284  CA   CYS    17      -4.090  24.450 101.980  1.00  0.00           C
ATOM    285  HA   CYS    17      -3.750  24.620 103.000  1.00  0.00           H
ATOM    286  CB   CYS    17      -3.470  25.560 101.150  1.00  0.00           C
ATOM    287  HB1  CYS    17      -3.910  25.570 100.140  1.00  0.00           H
ATOM    288  HB2  CYS    17      -2.420  25.350 100.980  1.00  0.00           H
ATOM    289  SG   CYS    17      -3.640  27.130 102.090  1.00  0.00           S
ATOM    290  HG   CYS    17      -4.920  27.240 102.460  1.00  0.00           H
ATOM    291  C    CYS    17      -5.600  24.350 101.840  1.00  0.00           C
ATOM    292  OC1  CYS    17      -6.120  23.410 101.180  1.00  0.00           O
ATOM    293  OC2  CYS    17      -6.340  25.270 102.260  1.00  0.00           O
TER
ENDMDL
```

Listing B.2: CM AMP *.pdb* file.

```
REMARK    GENERATED BY TRJCONV
TITLE     CM & Gold in Water t=   0.00000
REMARK    THIS IS A SIMULATION BOX
CRYST1   77.885   89.990  103.538  90.00  90.00  90.00 P 1           1
MODEL        1
ATOM      1  N    LYS     2      73.810  53.770  18.630  1.00  0.00           N
```

```
ATOM      2  H1  LYS     2      74.200  54.000  19.540  1.00  0.00           H
ATOM      3  H2  LYS     2      73.350  54.610  18.300  1.00  0.00           H
ATOM      4  H3  LYS     2      73.110  53.060  18.770  1.00  0.00           H
ATOM      5  CA  LYS     2      74.770  53.370  17.580  1.00  0.00           C
ATOM      6  HA  LYS     2      74.410  53.750  16.620  1.00  0.00           H
ATOM      7  CB  LYS     2      76.130  54.040  17.750  1.00  0.00           C
ATOM      8  HB1 LYS     2      76.770  53.810  16.900  1.00  0.00           H
ATOM      9  HB2 LYS     2      76.650  53.760  18.660  1.00  0.00           H
ATOM     10  CG  LYS     2      76.190  55.570  17.650  1.00  0.00           C
ATOM     11  HG1 LYS     2      75.540  56.030  18.390  1.00  0.00           H
ATOM     12  HG2 LYS     2      75.960  55.870  16.620  1.00  0.00           H
ATOM     13  CD  LYS     2      77.630  56.070  17.980  1.00  0.00           C
ATOM     14  HD1 LYS     2      78.390  55.610  17.340  1.00  0.00           H
ATOM     15  HD2 LYS     2      77.760  55.710  19.000  1.00  0.00           H
ATOM     16  CE  LYS     2      77.650  57.560  17.830  1.00  0.00           C
ATOM     17  HE1 LYS     2      76.800  58.110  18.240  1.00  0.00           H
ATOM     18  HE2 LYS     2      77.800  57.740  16.760  1.00  0.00           H
ATOM     19  NZ  LYS     2      78.920  58.130  18.380  1.00  0.00           N
ATOM     20  HZ1 LYS     2      79.730  57.550  18.220  1.00  0.00           H
ATOM     21  HZ2 LYS     2      79.060  59.060  18.010  1.00  0.00           H
ATOM     22  HZ3 LYS     2      78.920  58.250  19.390  1.00  0.00           H
ATOM     23  C   LYS     2      74.900  51.810  17.620  1.00  0.00           C
ATOM     24  O   LYS     2      73.900  51.140  17.250  1.00  0.00           O
ATOM     25  N   TRP     3      76.080  51.240  17.860  1.00  0.00           N
ATOM     26  H   TRP     3      76.900  51.790  18.070  1.00  0.00           H
ATOM     27  CA  TRP     3      76.300  49.800  17.850  1.00  0.00           C
ATOM     28  HA  TRP     3      76.090  49.460  16.840  1.00  0.00           H
ATOM     29  CB  TRP     3      77.790  49.520  18.140  1.00  0.00           C
ATOM     30  HB1 TRP     3      77.950  49.800  19.180  1.00  0.00           H
ATOM     31  HB2 TRP     3      78.240  50.110  17.340  1.00  0.00           H
ATOM     32  CG  TRP     3      78.370  48.160  17.910  1.00  0.00           C
ATOM     33  CD1 TRP     3      77.690  46.990  17.870  1.00  0.00           C
ATOM     34  HD1 TRP     3      76.620  46.880  17.990  1.00  0.00           H
ATOM     35  NE1 TRP     3      78.460  45.980  17.580  1.00  0.00           N
ATOM     36  HE1 TRP     3      78.170  45.020  17.460  1.00  0.00           H
ATOM     37  CE2 TRP     3      79.780  46.380  17.590  1.00  0.00           C
ATOM     38  CZ2 TRP     3      81.000  45.630  17.490  1.00  0.00           C
ATOM     39  HZ2 TRP     3      80.920  44.560  17.390  1.00  0.00           H
ATOM     40  CH2 TRP     3      82.210  46.270  17.650  1.00  0.00           C
ATOM     41  HH2 TRP     3      83.160  45.790  17.510  1.00  0.00           H
ATOM     42  CZ3 TRP     3      82.190  47.670  17.690  1.00  0.00           C
ATOM     43  HZ3 TRP     3      83.130  48.180  17.600  1.00  0.00           H
ATOM     44  CE3 TRP     3      81.040  48.410  17.840  1.00  0.00           C
ATOM     45  HE3 TRP     3      81.060  49.470  18.040  1.00  0.00           H
ATOM     46  CD2 TRP     3      79.760  47.790  17.810  1.00  0.00           C
ATOM     47  C   TRP     3      75.260  48.990  18.810  1.00  0.00           C
ATOM     48  O   TRP     3      75.120  49.360  20.030  1.00  0.00           O
ATOM     49  N   LYS     4      74.520  48.030  18.290  1.00  0.00           N
ATOM     50  H   LYS     4      74.550  47.950  17.290  1.00  0.00           H
ATOM     51  CA  LYS     4      73.630  47.170  19.070  1.00  0.00           C
ATOM     52  HA  LYS     4      74.020  47.060  20.080  1.00  0.00           H
ATOM     53  CB  LYS     4      72.180  47.730  19.040  1.00  0.00           C
ATOM     54  HB1 LYS     4      72.040  48.600  19.690  1.00  0.00           H
ATOM     55  HB2 LYS     4      71.470  47.010  19.450  1.00  0.00           H
ATOM     56  CG  LYS     4      71.500  48.090  17.710  1.00  0.00           C
ATOM     57  HG1 LYS     4      71.170  47.170  17.220  1.00  0.00           H
ATOM     58  HG2 LYS     4      72.280  48.580  17.120  1.00  0.00           H
```

```
ATOM    59  CD   LYS   4    70.270  48.950  17.850  1.00  0.00    C
ATOM    60  HD1  LYS   4    69.670  48.710  18.720  1.00  0.00    H
ATOM    61  HD2  LYS   4    69.700  48.850  16.920  1.00  0.00    H
ATOM    62  CE   LYS   4    70.670  50.400  17.910  1.00  0.00    C
ATOM    63  HE1  LYS   4    70.780  50.800  16.900  1.00  0.00    H
ATOM    64  HE2  LYS   4    71.580  50.510  18.480  1.00  0.00    H
ATOM    65  NZ   LYS   4    69.600  51.240  18.500  1.00  0.00    N
ATOM    66  HZ1  LYS   4    68.660  50.950  18.280  1.00  0.00    H
ATOM    67  HZ2  LYS   4    69.610  51.170  19.510  1.00  0.00    H
ATOM    68  HZ3  LYS   4    69.730  52.150  18.080  1.00  0.00    H
ATOM    69  C    LYS   4    73.590  45.730  18.460  1.00  0.00    C
ATOM    70  O    LYS   4    74.370  45.450  17.500  1.00  0.00    O
ATOM    71  N    LEU   5    72.720  44.800  18.910  1.00  0.00    N
ATOM    72  H    LEU   5    72.210  45.030  19.750  1.00  0.00    H
ATOM    73  CA   LEU   5    72.740  43.390  18.440  1.00  0.00    C
ATOM    74  HA   LEU   5    73.110  43.400  17.420  1.00  0.00    H
ATOM    75  CB   LEU   5    73.490  42.510  19.470  1.00  0.00    C
ATOM    76  HB1  LEU   5    72.910  42.510  20.400  1.00  0.00    H
ATOM    77  HB2  LEU   5    74.510  42.890  19.530  1.00  0.00    H
ATOM    78  CG   LEU   5    73.670  41.060  18.980  1.00  0.00    C
ATOM    79  HG   LEU   5    72.790  40.590  18.540  1.00  0.00    H
ATOM    80  CD1  LEU   5    74.850  40.940  17.930  1.00  0.00    C
ATOM    81 1HD1  LEU   5    74.840  39.880  17.640  1.00  0.00    H
ATOM    82 2HD1  LEU   5    74.730  41.590  17.060  1.00  0.00    H
ATOM    83 3HD1  LEU   5    75.820  41.230  18.340  1.00  0.00    H
ATOM    84  CD2  LEU   5    74.420  40.170  20.090  1.00  0.00    C
ATOM    85 1HD2  LEU   5    73.930  40.290  21.060  1.00  0.00    H
ATOM    86 2HD2  LEU   5    74.340  39.110  19.850  1.00  0.00    H
ATOM    87 3HD2  LEU   5    75.490  40.410  20.140  1.00  0.00    H
ATOM    88  C    LEU   5    71.270  42.880  18.200  1.00  0.00    C
ATOM    89  O    LEU   5    71.040  42.000  17.340  1.00  0.00    O
ATOM    90  N    PHE   6    70.300  43.440  18.970  1.00  0.00    N
ATOM    91  H    PHE   6    70.680  44.030  19.680  1.00  0.00    H
ATOM    92  CA   PHE   6    68.860  43.600  18.750  1.00  0.00    C
ATOM    93  HA   PHE   6    68.460  43.790  19.750  1.00  0.00    H
ATOM    94  CB   PHE   6    68.610  44.970  17.970  1.00  0.00    C
ATOM    95  HB1  PHE   6    68.830  44.770  16.920  1.00  0.00    H
ATOM    96  HB2  PHE   6    69.280  45.720  18.410  1.00  0.00    H
ATOM    97  CG   PHE   6    67.350  45.620  18.230  1.00  0.00    C
ATOM    98  CD1  PHE   6    67.270  46.440  19.380  1.00  0.00    C
ATOM    99  HD1  PHE   6    68.120  46.660  20.010  1.00  0.00    H
ATOM   100  CE1  PHE   6    66.070  47.010  19.780  1.00  0.00    C
ATOM   101  HE1  PHE   6    66.130  47.680  20.630  1.00  0.00    H
ATOM   102  CZ   PHE   6    64.890  46.960  18.980  1.00  0.00    C
ATOM   103  HZ   PHE   6    64.130  47.680  19.210  1.00  0.00    H
ATOM   104  CE2  PHE   6    65.020  46.180  17.760  1.00  0.00    C
ATOM   105  HE2  PHE   6    64.160  46.150  17.110  1.00  0.00    H
ATOM   106  CD2  PHE   6    66.230  45.490  17.460  1.00  0.00    C
ATOM   107  HD2  PHE   6    66.280  44.810  16.620  1.00  0.00    H
ATOM   108  C    PHE   6    68.090  42.480  18.030  1.00  0.00    C
ATOM   109  O    PHE   6    67.150  42.680  17.270  1.00  0.00    O
ATOM   110  N    LYS   7    68.550  41.290  18.270  1.00  0.00    N
ATOM   111  H    LYS   7    69.400  41.250  18.820  1.00  0.00    H
ATOM   112  CA   LYS   7    68.040  40.010  17.860  1.00  0.00    C
ATOM   113  HA   LYS   7    67.900  40.030  16.780  1.00  0.00    H
ATOM   114  CB   LYS   7    68.890  38.880  18.390  1.00  0.00    C
ATOM   115  HB1  LYS   7    68.370  37.950  18.190  1.00  0.00    H
```

```
ATOM   116  HB2 LYS     7      68.910  38.930  19.480  1.00  0.00           H
ATOM   117  CG  LYS     7      70.310  38.870  17.830  1.00  0.00           C
ATOM   118  HG1 LYS     7      70.980  39.640  18.240  1.00  0.00           H
ATOM   119  HG2 LYS     7      70.190  39.010  16.750  1.00  0.00           H
ATOM   120  CD  LYS     7      71.100  37.600  18.120  1.00  0.00           C
ATOM   121  HD1 LYS     7      70.440  36.800  17.790  1.00  0.00           H
ATOM   122  HD2 LYS     7      71.290  37.470  19.180  1.00  0.00           H
ATOM   123  CE  LYS     7      72.440  37.520  17.420  1.00  0.00           C
ATOM   124  HE1 LYS     7      72.800  38.550  17.450  1.00  0.00           H
ATOM   125  HE2 LYS     7      72.310  37.190  16.390  1.00  0.00           H
ATOM   126  NZ  LYS     7      73.370  36.570  18.060  1.00  0.00           N
ATOM   127  HZ1 LYS     7      73.000  35.660  17.810  1.00  0.00           H
ATOM   128  HZ2 LYS     7      74.310  36.530  17.690  1.00  0.00           H
ATOM   129  HZ3 LYS     7      73.390  36.680  19.060  1.00  0.00           H
ATOM   130  C   LYS     7      66.620  39.740  18.390  1.00  0.00           C
ATOM   131  O   LYS     7      66.270  40.340  19.440  1.00  0.00           O
ATOM   132  N   LYS     8      65.890  38.910  17.680  1.00  0.00           N
ATOM   133  H   LYS     8      66.270  38.460  16.870  1.00  0.00           H
ATOM   134  CA  LYS     8      64.460  38.620  18.090  1.00  0.00           C
ATOM   135  HA  LYS     8      64.390  38.590  19.180  1.00  0.00           H
ATOM   136  CB  LYS     8      63.380  39.640  17.670  1.00  0.00           C
ATOM   137  HB1 LYS     8      62.490  39.370  18.250  1.00  0.00           H
ATOM   138  HB2 LYS     8      63.030  39.530  16.640  1.00  0.00           H
ATOM   139  CG  LYS     8      63.780  41.090  17.960  1.00  0.00           C
ATOM   140  HG1 LYS     8      64.580  41.290  17.250  1.00  0.00           H
ATOM   141  HG2 LYS     8      64.140  41.220  18.990  1.00  0.00           H
ATOM   142  CD  LYS     8      62.520  42.090  17.820  1.00  0.00           C
ATOM   143  HD1 LYS     8      61.980  41.890  18.750  1.00  0.00           H
ATOM   144  HD2 LYS     8      61.900  41.730  17.000  1.00  0.00           H
ATOM   145  CE  LYS     8      62.860  43.490  17.730  1.00  0.00           C
ATOM   146  HE1 LYS     8      63.250  43.600  16.710  1.00  0.00           H
ATOM   147  HE2 LYS     8      63.750  43.600  18.350  1.00  0.00           H
ATOM   148  NZ  LYS     8      61.770  44.400  18.180  1.00  0.00           N
ATOM   149  HZ1 LYS     8      61.660  44.310  19.180  1.00  0.00           H
ATOM   150  HZ2 LYS     8      61.870  45.350  17.840  1.00  0.00           H
ATOM   151  HZ3 LYS     8      60.830  44.090  17.970  1.00  0.00           H
ATOM   152  C   LYS     8      64.030  37.210  17.690  1.00  0.00           C
ATOM   153  O   LYS     8      64.820  36.440  17.140  1.00  0.00           O
ATOM   154  N   ILE     9      62.830  36.760  18.070  1.00  0.00           N
ATOM   155  H   ILE     9      62.200  37.400  18.540  1.00  0.00           H
ATOM   156  CA  ILE     9      62.410  35.360  18.020  1.00  0.00           C
ATOM   157  HA  ILE     9      62.840  34.880  17.130  1.00  0.00           H
ATOM   158  CB  ILE     9      62.900  34.690  19.340  1.00  0.00           C
ATOM   159  HB  ILE     9      63.960  34.960  19.400  1.00  0.00           H
ATOM   160  CG2 ILE     9      62.220  35.210  20.620  1.00  0.00           C
ATOM   161 1HG2 ILE     9      62.690  34.700  21.460  1.00  0.00           H
ATOM   162 2HG2 ILE     9      62.370  36.280  20.800  1.00  0.00           H
ATOM   163 3HG2 ILE     9      61.150  35.050  20.560  1.00  0.00           H
ATOM   164  CG1 ILE     9      62.820  33.140  19.390  1.00  0.00           C
ATOM   165 1HG1 ILE     9      61.780  32.870  19.580  1.00  0.00           H
ATOM   166 2HG1 ILE     9      63.340  32.800  20.280  1.00  0.00           H
ATOM   167  CD  ILE     9      63.360  32.430  18.110  1.00  0.00           C
ATOM   168  HD1 ILE     9      64.240  32.940  17.720  1.00  0.00           H
ATOM   169  HD2 ILE     9      63.480  31.350  18.220  1.00  0.00           H
ATOM   170  HD3 ILE     9      62.720  32.500  17.230  1.00  0.00           H
ATOM   171  C   ILE     9      60.870  35.180  17.780  1.00  0.00           C
ATOM   172  O   ILE     9      60.210  36.230  17.620  1.00  0.00           O
```

```
ATOM   173  N    GLY  10     60.400  33.900  17.730  1.00  0.00        N
ATOM   174  H    GLY  10     61.090  33.180  17.890  1.00  0.00        H
ATOM   175  CA   GLY  10     59.020  33.470  17.800  1.00  0.00        C
ATOM   176  HA1  GLY  10     58.470  33.980  17.010  1.00  0.00        H
ATOM   177  HA2  GLY  10     58.740  33.740  18.820  1.00  0.00        H
ATOM   178  C    GLY  10     58.810  31.950  17.560  1.00  0.00        C
ATOM   179  O    GLY  10     59.760  31.280  17.250  1.00  0.00        O
ATOM   180  N    ALA  11     57.590  31.480  17.900  1.00  0.00        N
ATOM   181  H    ALA  11     56.950  32.170  18.270  1.00  0.00        H
ATOM   182  CA   ALA  11     57.230  30.020  17.900  1.00  0.00        C
ATOM   183  HA   ALA  11     57.850  29.500  17.180  1.00  0.00        H
ATOM   184  CB   ALA  11     57.610  29.540  19.290  1.00  0.00        C
ATOM   185  HB1  ALA  11     58.620  29.850  19.550  1.00  0.00        H
ATOM   186  HB2  ALA  11     56.960  30.020  20.020  1.00  0.00        H
ATOM   187  HB3  ALA  11     57.340  28.500  19.510  1.00  0.00        H
ATOM   188  C    ALA  11     55.730  29.790  17.570  1.00  0.00        C
ATOM   189  O    ALA  11     55.270  28.650  17.430  1.00  0.00        O
ATOM   190  N    VAL  12     54.880  30.870  17.610  1.00  0.00        N
ATOM   191  H    VAL  12     55.210  31.820  17.670  1.00  0.00        H
ATOM   192  CA   VAL  12     53.420  30.750  18.090  1.00  0.00        C
ATOM   193  HA   VAL  12     52.980  29.870  17.620  1.00  0.00        H
ATOM   194  CB   VAL  12     53.310  30.520  19.630  1.00  0.00        C
ATOM   195  HB   VAL  12     52.260  30.580  19.930  1.00  0.00        H
ATOM   196  CG1  VAL  12     53.810  29.240  20.230  1.00  0.00        C
ATOM   197 1HG1  VAL  12     54.890  29.210  20.150  1.00  0.00        H
ATOM   198 2HG1  VAL  12     53.470  29.100  21.260  1.00  0.00        H
ATOM   199 3HG1  VAL  12     53.390  28.440  19.610  1.00  0.00        H
ATOM   200  CG2  VAL  12     53.920  31.690  20.380  1.00  0.00        C
ATOM   201 1HG2  VAL  12     53.870  31.700  21.470  1.00  0.00        H
ATOM   202 2HG2  VAL  12     54.960  31.820  20.080  1.00  0.00        H
ATOM   203 3HG2  VAL  12     53.470  32.610  19.990  1.00  0.00        H
ATOM   204  C    VAL  12     52.540  31.920  17.760  1.00  0.00        C
ATOM   205  O    VAL  12     53.100  32.990  17.550  1.00  0.00        O
ATOM   206  N    LEU  13     51.210  31.770  17.680  1.00  0.00        N
ATOM   207  H    LEU  13     50.790  30.850  17.750  1.00  0.00        H
ATOM   208  CA   LEU  13     50.330  32.930  17.730  1.00  0.00        C
ATOM   209  HA   LEU  13     50.300  33.440  16.760  1.00  0.00        H
ATOM   210  CB   LEU  13     48.930  32.430  17.950  1.00  0.00        C
ATOM   211  HB1  LEU  13     48.910  31.960  18.940  1.00  0.00        H
ATOM   212  HB2  LEU  13     48.790  31.550  17.320  1.00  0.00        H
ATOM   213  CG   LEU  13     47.780  33.420  17.790  1.00  0.00        C
ATOM   214  HG   LEU  13     47.720  34.050  16.900  1.00  0.00        H
ATOM   215  CD1  LEU  13     46.500  32.590  17.810  1.00  0.00        C
ATOM   216 1HD1  LEU  13     46.260  32.150  18.780  1.00  0.00        H
ATOM   217 2HD1  LEU  13     45.620  33.130  17.440  1.00  0.00        H
ATOM   218 3HD1  LEU  13     46.620  31.810  17.060  1.00  0.00        H
ATOM   219  CD2  LEU  13     47.570  34.360  18.920  1.00  0.00        C
ATOM   220 1HD2  LEU  13     46.690  34.960  18.670  1.00  0.00        H
ATOM   221 2HD2  LEU  13     47.550  33.830  19.870  1.00  0.00        H
ATOM   222 3HD2  LEU  13     48.370  35.100  19.010  1.00  0.00        H
ATOM   223  C    LEU  13     50.790  34.000  18.740  1.00  0.00        C
ATOM   224  O    LEU  13     50.980  33.710  19.910  1.00  0.00        O
ATOM   225  N    LYS  14     50.900  35.210  18.270  1.00  0.00        N
ATOM   226  H    LYS  14     50.560  35.340  17.330  1.00  0.00        H
ATOM   227  CA   LYS  14     51.170  36.470  19.020  1.00  0.00        C
ATOM   228  HA   LYS  14     50.830  36.360  20.050  1.00  0.00        H
ATOM   229  CB   LYS  14     52.690  36.720  19.080  1.00  0.00        C
```

```
ATOM   230  HB1 LYS   14     53.270  36.010  19.670  1.00  0.00      H
ATOM   231  HB2 LYS   14     52.890  37.690  19.540  1.00  0.00      H
ATOM   232  CG  LYS   14     53.270  36.870  17.650  1.00  0.00      C
ATOM   233  HG1 LYS   14     52.780  37.520  16.920  1.00  0.00      H
ATOM   234  HG2 LYS   14     53.120  35.880  17.210  1.00  0.00      H
ATOM   235  CD  LYS   14     54.800  37.110  17.660  1.00  0.00      C
ATOM   236  HD1 LYS   14     55.170  36.750  16.700  1.00  0.00      H
ATOM   237  HD2 LYS   14     55.170  36.590  18.540  1.00  0.00      H
ATOM   238  CE  LYS   14     55.140  38.610  17.710  1.00  0.00      C
ATOM   239  HE1 LYS   14     54.640  39.120  16.890  1.00  0.00      H
ATOM   240  HE2 LYS   14     56.210  38.750  17.570  1.00  0.00      H
ATOM   241  NZ  LYS   14     54.710  39.330  18.930  1.00  0.00      N
ATOM   242  HZ1 LYS   14     55.090  40.270  18.920  1.00  0.00      H
ATOM   243  HZ2 LYS   14     53.710  39.420  19.060  1.00  0.00      H
ATOM   244  HZ3 LYS   14     55.150  38.990  19.770  1.00  0.00      H
ATOM   245  C   LYS   14     50.380  37.560  18.270  1.00  0.00      C
ATOM   246  O   LYS   14     49.830  37.180  17.200  1.00  0.00      O
ATOM   247  N   VAL   15     50.500  38.800  18.640  1.00  0.00      N
ATOM   248  H   VAL   15     51.110  39.040  19.400  1.00  0.00      H
ATOM   249  CA  VAL   15     50.240  39.990  17.800  1.00  0.00      C
ATOM   250  HA  VAL   15     49.970  39.710  16.780  1.00  0.00      H
ATOM   251  CB  VAL   15     49.080  40.780  18.440  1.00  0.00      C
ATOM   252  HB  VAL   15     48.220  40.130  18.610  1.00  0.00      H
ATOM   253  CG1 VAL   15     49.430  41.240  19.890  1.00  0.00      C
ATOM   254 1HG1 VAL   15     50.260  41.960  19.920  1.00  0.00      H
ATOM   255 2HG1 VAL   15     48.600  41.720  20.400  1.00  0.00      H
ATOM   256 3HG1 VAL   15     49.700  40.380  20.490  1.00  0.00      H
ATOM   257  CG2 VAL   15     48.550  42.020  17.650  1.00  0.00      C
ATOM   258 1HG2 VAL   15     47.470  42.020  17.780  1.00  0.00      H
ATOM   259 2HG2 VAL   15     48.910  42.870  18.230  1.00  0.00      H
ATOM   260 3HG2 VAL   15     48.960  42.040  16.640  1.00  0.00      H
ATOM   261  C   VAL   15     51.570  40.810  17.430  1.00  0.00      C
ATOM   262  O   VAL   15     52.590  40.150  17.200  1.00  0.00      O
ATOM   263  N   LEU   16     51.550  42.140  17.560  1.00  0.00      N
ATOM   264  H   LEU   16     50.660  42.580  17.770  1.00  0.00      H
ATOM   265  CA  LEU   16     52.730  43.000  17.840  1.00  0.00      C
ATOM   266  HA  LEU   16     53.420  42.820  17.020  1.00  0.00      H
ATOM   267  CB  LEU   16     52.230  44.500  17.940  1.00  0.00      C
ATOM   268  HB1 LEU   16     51.780  44.700  18.910  1.00  0.00      H
ATOM   269  HB2 LEU   16     51.440  44.710  17.220  1.00  0.00      H
ATOM   270  CG  LEU   16     53.340  45.560  17.790  1.00  0.00      C
ATOM   271  HG  LEU   16     53.870  45.450  16.840  1.00  0.00      H
ATOM   272  CD1 LEU   16     52.690  46.920  17.840  1.00  0.00      C
ATOM   273 1HD1 LEU   16     53.340  47.710  17.460  1.00  0.00      H
ATOM   274 2HD1 LEU   16     51.770  46.990  17.260  1.00  0.00      H
ATOM   275 3HD1 LEU   16     52.450  47.130  18.880  1.00  0.00      H
ATOM   276  CD2 LEU   16     54.360  45.550  18.930  1.00  0.00      C
ATOM   277 1HD2 LEU   16     55.070  44.730  18.840  1.00  0.00      H
ATOM   278 2HD2 LEU   16     54.790  46.540  18.760  1.00  0.00      H
ATOM   279 3HD2 LEU   16     53.820  45.650  19.870  1.00  0.00      H
ATOM   280  C   LEU   16     53.570  42.480  18.980  1.00  0.00      C
ATOM   281  OC1 LEU   16     53.200  42.380  20.130  1.00  0.00      O
ATOM   282  OC2 LEU   16     54.720  42.060  18.720  1.00  0.00      O
TER
ENDMDL
```

Interaction with the AuNP

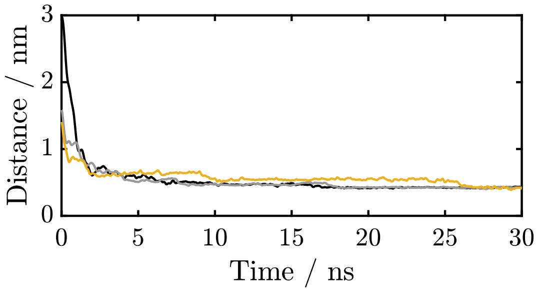

(a)

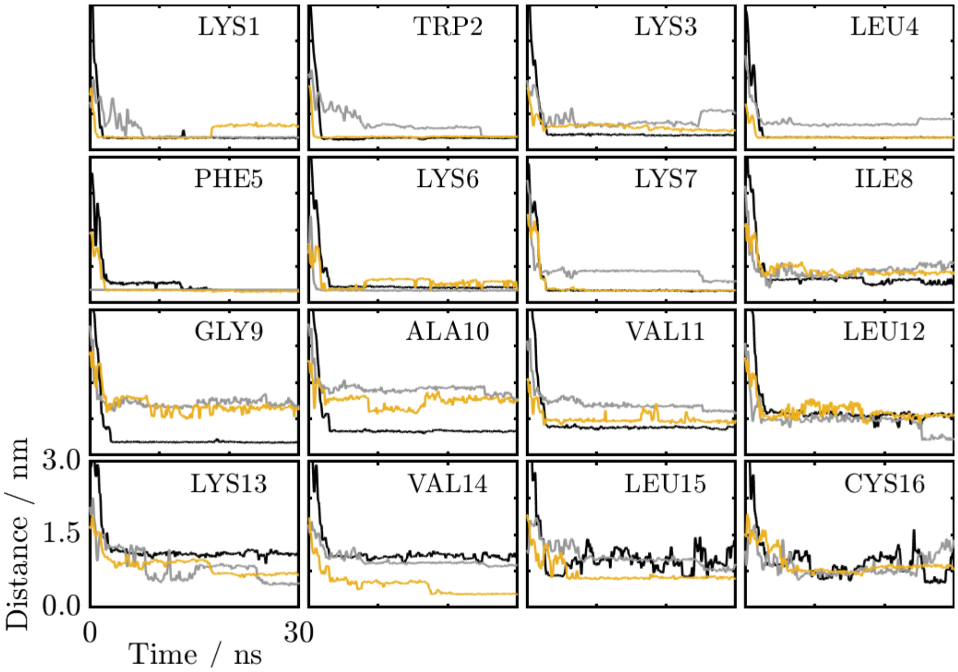

(b)

Figure B.9: Distance of the CM-SH peptide to a AuNP surface. (a) averaged for all residues; and (b) by residue. Each color corresponds to a different AuNP diameter (— 2 nm, — 4 nm and — 6 nm).

C. Cathelicidin-derived AMP

In this appendix is added additional information regarding the interaction of LL37 and LL37-SH with a AuNP.

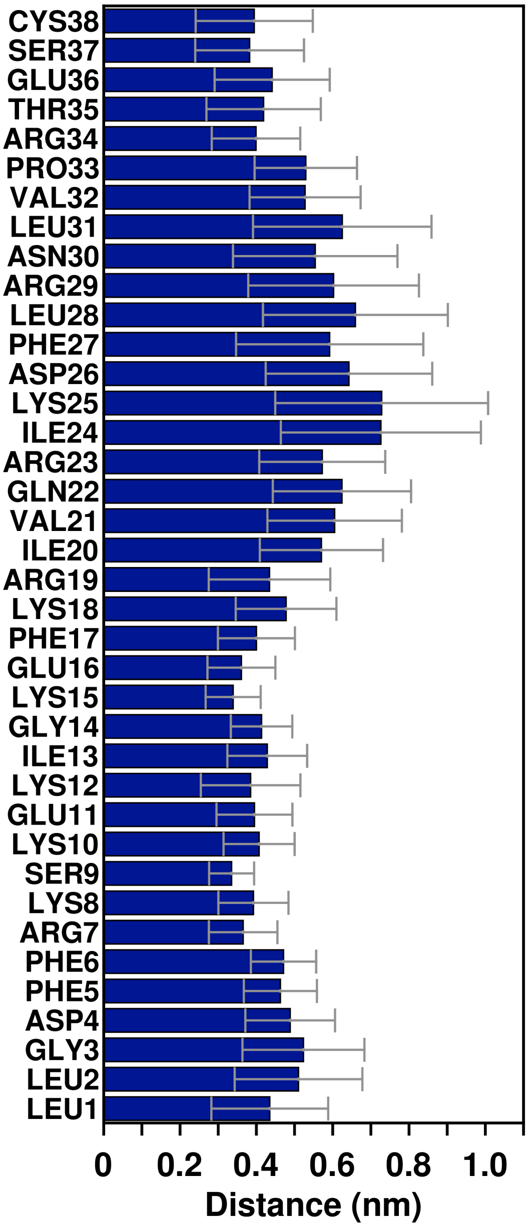

Figure C.1: Position distance of the LL37-SH residues to the AuNP surface at the end of the simulation.

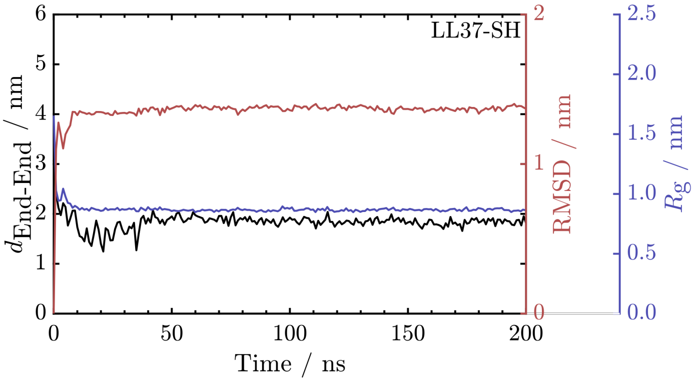

(a)

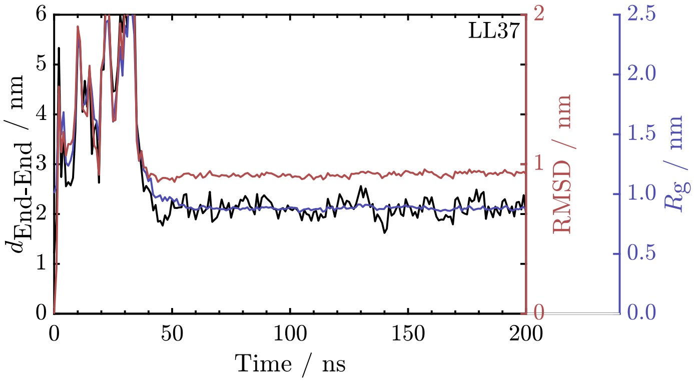

(b)

Figure C.2: Evolution of $d_{\text{End}-\text{End}}$, RMSD and R_g with the simulation time for the systems without AuNP. Plot (a) for LL37-SH and (b) for the LL37.

FE of the selected CVs was reweighted taking into account the energy penalties added by the algorithm. To achieve this, the CVs histograms were computed using the **REWEIGHT_BIAS** and **HISTOGRAM** algorithms included in PLUMED 2[190] suite. The obtained histograms were then processed with the **CONVERT_TO_FES** utility to obtain the reweighed FE for each CV. A similar approach is detailed by Klug et al.[211].

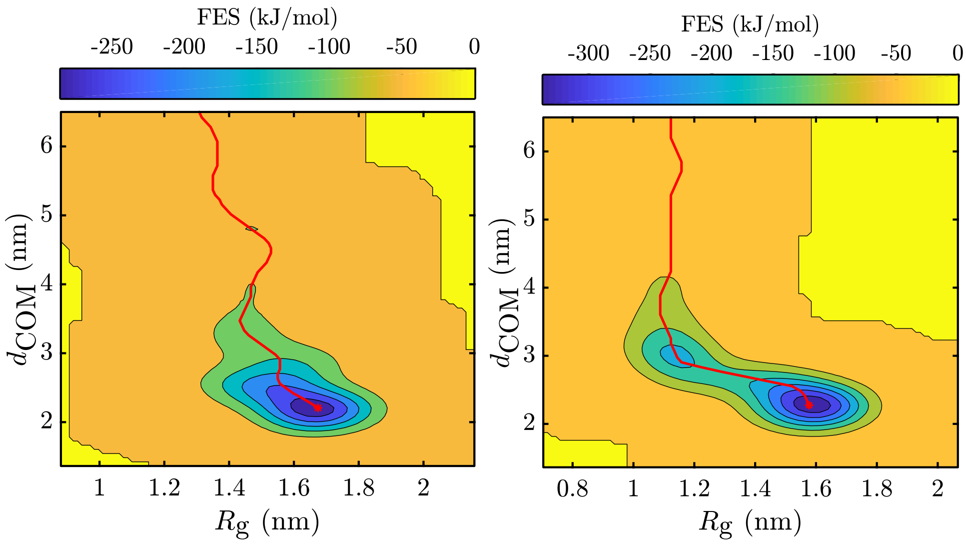

(a)

(b)

Figure C.3: Free energy surface before the bias reweight process. Plot (a) for LL37-SH and (b) for the LL37.

Table C.1: Lowest free energy value per unique d_{COMs} for the LL37-SH peptide. Lowest value highlighted in gray.

$\mathbf{R_g}$ **(nm)**	$\mathbf{d_{COMs}}$ **(nm)**	**Free Energy (kJ/mol)**
1.2866	6.8239	-5.7487
1.2866	6.8039	-6.0922
1.2866	6.784	-6.4166
1.2866	6.764	-6.7204
1.3065	6.744	-7.0053
1.3065	6.7241	-7.2718
1.3065	6.7041	-7.5196
1.3065	6.6841	-7.7484
1.3065	6.6641	-7.959
1.3065	6.6442	-8.1516
1.3065	6.6242	-8.3262
1.3065	6.6042	-8.4832

Continued on next page

Table C.1 – continued from previous page

R_g (nm)	d_{COMs} (nm)	Free Energy (kJ/mol)
1.3065	6.5842	-8.623
1.3065	6.5643	-8.7458
1.3065	6.5443	-8.8516
1.3065	6.5243	-8.9409
1.3065	6.5044	-9.0145
1.3264	6.4844	-9.0739
1.3264	6.4644	-9.1191
1.3264	6.4444	-9.1498
1.3264	6.4245	-9.167
1.3264	6.4045	-9.1713
1.3264	6.3845	-9.1637
1.3264	6.3646	-9.1453
1.3264	6.3446	-9.1174
1.3264	6.3246	-9.0815
1.3463	6.3046	-9.0414
1.3463	6.2847	-8.9983
1.3463	6.2647	-8.9532
1.3463	6.2447	-8.9077
1.3463	6.2248	-8.8638
1.3463	6.2048	-8.8239
1.3463	6.1848	-8.7898
1.3662	6.1648	-8.7659
1.3662	6.1449	-8.7508
1.3662	6.1249	-8.744
1.3662	6.1049	-8.7457
1.3662	6.0849	-8.7556
1.3662	6.065	-8.7724
1.3662	6.045	-8.7952
1.3662	6.025	-8.8227
1.3861	6.0051	-8.8537
1.3861	5.9851	-8.8859
1.3861	5.9651	-8.9175
1.3861	5.9451	-8.9469
1.3861	5.9252	-8.9734
1.3861	5.9052	-8.996

Continued on next page

Table C.1 – continued from previous page

R_g (nm)	d_{COMs} (nm)	Free Energy (kJ/mol)
1.3861	5.8852	-9.0144
1.3861	5.8653	-9.028
1.3662	5.8453	-9.0388
1.3662	5.8253	-9.0463
1.3662	5.8053	-9.0505
1.3662	5.7854	-9.0519
1.3662	5.7654	-9.0517
1.3662	5.7454	-9.0506
1.3662	5.7255	-9.0495
1.3662	5.7055	-9.0496
1.3662	5.6855	-9.0509
1.3662	5.6655	-9.0544
1.3463	5.6456	-9.0628
1.3463	5.6256	-9.0749
1.3463	5.6056	-9.0893
1.3463	5.5857	-9.1064
1.3463	5.5657	-9.1255
1.3463	5.5457	-9.1466
1.3463	5.5257	-9.1692
1.3463	5.5058	-9.1918
1.3463	5.4858	-9.2137
1.3463	5.4658	-9.2343
1.3463	5.4458	-9.2531
1.3463	5.4259	-9.2695
1.3463	5.4059	-9.2832
1.3463	5.3859	-9.2941
1.3463	5.366	-9.3024
1.3463	5.346	-9.3082
1.3662	5.326	-9.3125
1.3662	5.306	-9.3182
1.3662	5.2861	-9.3236
1.3662	5.2661	-9.3301
1.3662	5.2461	-9.3386
1.3662	5.2262	-9.3507
1.3861	5.2062	-9.3688

Continued on next page

Table C.1 – continued from previous page

R_g (nm)	d_{COMs} (nm)	Free Energy (kJ/mol)
1.3861	5.1862	-9.3966
1.3861	5.1662	-9.4316
1.3861	5.1463	-9.4739
1.4061	5.1263	-9.5266
1.4061	5.1063	-9.5908
1.4061	5.0864	-9.662
1.426	5.0664	-9.7391
1.426	5.0464	-9.8267
1.426	5.0264	-9.9168
1.426	5.0065	-10.007
1.4459	4.9865	-10.1
1.4459	4.9665	-10.191
1.4459	4.9465	-10.277
1.4459	4.9266	-10.355
1.4658	4.9066	-10.428
1.4658	4.8866	-10.493
1.4658	4.8667	-10.548
1.4658	4.8467	-10.59
1.4857	4.8267	-10.621
1.4857	4.8067	-10.643
1.4857	4.7868	-10.653
1.4857	4.7668	-10.65
1.4857	4.7468	-10.635
1.5056	4.7269	-10.608
1.5056	4.7069	-10.574
1.5056	4.6869	-10.531
1.5056	4.6669	-10.478
1.5056	4.647	-10.419
1.5056	4.627	-10.353
1.5256	4.607	-10.286
1.5256	4.5871	-10.217
1.5256	4.5671	-10.147
1.5256	4.5471	-10.079
1.5256	4.5271	-10.014
1.5256	4.5072	-9.9541

Continued on next page

Table C.1 – continued from previous page

R_g (nm)	d_{COMs} (nm)	Free Energy (kJ/mol)
1.5256	4.4872	-9.9013
1.5256	4.4672	-9.8568
1.5256	4.4472	-9.8208
1.5256	4.4273	-9.7942
1.5256	4.4073	-9.7774
1.5256	4.3873	-9.7697
1.5256	4.3674	-9.7709
1.5056	4.3474	-9.7816
1.5056	4.3274	-9.8009
1.5056	4.3074	-9.8257
1.5056	4.2875	-9.8548
1.5056	4.2675	-9.8867
1.5056	4.2475	-9.9203
1.5056	4.2276	-9.9548
1.4857	4.2076	-9.992
1.4857	4.1876	-10.029
1.4857	4.1676	-10.064
1.4857	4.1477	-10.097
1.4857	4.1277	-10.129
1.4857	4.1077	-10.158
1.4857	4.0878	-10.185
1.4857	4.0678	-10.211
1.4658	4.0478	-10.235
1.4658	4.0278	-10.26
1.4658	4.0079	-10.283
1.4658	3.9879	-10.306
1.4658	3.9679	-10.326
1.4658	3.948	-10.346
1.4658	3.928	-10.364
1.4658	3.908	-10.381
1.4658	3.888	-10.397
1.4658	3.8681	-10.413
1.4658	3.8481	-10.429
1.4658	3.8281	-10.446
1.4658	3.8081	-10.464

Continued on next page

Table C.1 – continued from previous page

R_g (nm)	d_{COMs} (nm)	Free Energy (kJ/mol)
1.4658	3.7882	-10.484
1.4658	3.7682	-10.507
1.4459	3.7482	-10.534
1.4459	3.7283	-10.568
1.4459	3.7083	-10.609
1.4459	3.6883	-10.658
1.4459	3.6683	-10.716
1.4459	3.6484	-10.782
1.4459	3.6284	-10.859
1.4459	3.6084	-10.945
1.4459	3.5885	-11.04
1.4459	3.5685	-11.143
1.4459	3.5485	-11.253
1.4459	3.5285	-11.367
1.4459	3.5086	-11.484
1.4459	3.4886	-11.604
1.4459	3.4686	-11.723
1.4459	3.4487	-11.839
1.4459	3.4287	-11.953
1.4459	3.4087	-12.062
1.4459	3.3887	-12.165
1.4459	3.3688	-12.262
1.4459	3.3488	-12.353
1.4459	3.3288	-12.438
1.4658	3.3088	-12.52
1.4658	3.2889	-12.599
1.4658	3.2689	-12.676
1.4658	3.2489	-12.752
1.4658	3.229	-12.824
1.4857	3.209	-12.9
1.4857	3.189	-12.982
1.4857	3.169	-13.073
1.5056	3.1491	-13.181
1.5056	3.1291	-13.314
1.5056	3.1091	-13.447

Continued on next page

Table C.1 – continued from previous page

R_g (nm)	d_{COMs} (nm)	Free Energy (kJ/mol)
1.5056	3.0892	-13.592
1.5256	3.0692	-13.768
1.5256	3.0492	-13.96
1.5256	3.0292	-14.167
1.5256	3.0093	-14.395
1.5256	2.9893	-14.645
1.5256	2.9693	-14.914
1.5256	2.9494	-15.2
1.5256	2.9294	-15.503
1.5256	2.9094	-15.821
1.5256	2.8894	-16.149
1.5256	2.8695	-16.489
1.5256	2.8495	-16.858
1.5455	2.8295	-17.705
1.5654	2.8096	-18.548
1.5654	2.7896	-19.095
1.5654	2.7696	-19.641
1.5853	2.7496	-20.198
1.5853	2.7297	-20.765
1.5853	2.7097	-21.335
1.5853	2.6897	-21.904
1.6052	2.6697	-22.473
1.6052	2.6498	-23.039
1.6052	2.6298	-23.596
1.6052	2.6098	-24.142
1.6052	2.5899	-24.676
1.6052	2.5699	-25.195
1.6251	2.5499	-25.7
1.6251	2.5299	-26.189
1.6251	2.51	-26.659
1.6251	2.49	-27.11
1.6251	2.47	-27.541
1.6251	2.4501	-27.951
1.6251	2.4301	-28.339
1.6251	2.4101	-28.706

Continued on next page

Table C.1 – continued from previous page

R_g (nm)	d_{COMs} (nm)	Free Energy (kJ/mol)
1.6251	2.3901	-29.05
1.6251	2.3702	-29.372
1.6251	2.3502	-29.671
1.6251	2.3302	-29.946
1.6251	2.3103	-30.198
1.6251	2.2903	-30.426
1.6251	2.2703	-30.63
1.6251	2.2503	-30.81
1.6251	2.2304	-30.966
1.6251	2.2104	-31.098
1.6251	2.1904	-31.205
1.6251	2.1704	-31.288
1.6251	2.1505	-31.347
1.6251	2.1305	-31.381
1.6251	2.1105	-31.391

Table C.2: Lowest free energy value per unique d_{COMs} for the LL37 peptide. Lowest value highlighted in gray.

R_g (nm)	d_{COMs} (nm)	Free Energy (kJ/mol)
1.1158	6.4611	-5.7546
1.1158	6.4411	-6.0943
1.1158	6.4212	-6.4153
1.1158	6.4013	-6.7178
1.1158	6.3813	-7.0023
1.1158	6.3614	-7.2703
1.1158	6.3415	-7.5199
1.1158	6.3215	-7.7526
1.1158	6.3016	-7.9689
1.1158	6.2817	-8.1694
1.1357	6.2618	-8.355
1.1357	6.2418	-8.5262
1.1357	6.2219	-8.6829
1.1357	6.202	-8.8251

Continued on next page

Table C.2 – continued from previous page

R_g (nm)	d_{COMs} (nm)	Free Energy (kJ/mol)
1.1357	6.182	-8.9533
1.1357	6.1621	-9.0678
1.1357	6.1422	-9.1687
1.1357	6.1222	-9.2563
1.1357	6.1023	-9.3308
1.1357	6.0824	-9.3927
1.1357	6.0624	-9.4421
1.1357	6.0425	-9.4791
1.1357	6.0226	-9.5041
1.1357	6.0026	-9.5174
1.1357	5.9827	-9.5194
1.1357	5.9628	-9.5105
1.1357	5.9428	-9.4911
1.1556	5.9229	-9.4621
1.1556	5.903	-9.4248
1.1556	5.883	-9.3789
1.1556	5.8631	-9.3256
1.1556	5.8432	-9.2657
1.1556	5.8233	-9.1999
1.1556	5.8033	-9.1295
1.1556	5.7834	-9.0558
1.1556	5.7635	-8.9795
1.1556	5.7435	-8.9022
1.1556	5.7236	-8.8245
1.1556	5.7037	-8.7478
1.1556	5.6837	-8.6728
1.1556	5.6638	-8.6006
1.1357	5.6439	-8.5326
1.1357	5.6239	-8.4684
1.1357	5.604	-8.4086
1.1357	5.5841	-8.3532
1.1357	5.5641	-8.3028
1.1357	5.5442	-8.2573
1.1357	5.5243	-8.2167
1.1357	5.5043	-8.1809

Continued on next page

Table C.2 – continued from previous page

R_g (nm)	d_{COMs} (nm)	Free Energy (kJ/mol)
1.1357	5.4844	-8.1499
1.1357	5.4645	-8.1244
1.1357	5.4445	-8.1037
1.1357	5.4246	-8.0873
1.1357	5.4047	-8.0751
1.1357	5.3848	-8.0669
1.1357	5.3648	-8.0621
1.1357	5.3449	-8.0601
1.1357	5.325	-8.0605
1.1357	5.305	-8.0645
1.1357	5.2851	-8.07
1.1357	5.2652	-8.0779
1.1357	5.2452	-8.0855
1.1158	5.2253	-8.0945
1.1158	5.2054	-8.1033
1.1158	5.1854	-8.1134
1.1158	5.1655	-8.1235
1.1158	5.1456	-8.1328
1.1158	5.1256	-8.1417
1.1158	5.1057	-8.1502
1.1158	5.0858	-8.1583
1.1158	5.0658	-8.1663
1.1158	5.0459	-8.1747
1.1158	5.026	-8.1836
1.1158	5.006	-8.1935
1.1158	4.9861	-8.2049
1.1158	4.9662	-8.2181
1.1158	4.9463	-8.2334
1.1158	4.9263	-8.2509
1.1158	4.9064	-8.2713
1.1158	4.8865	-8.2945
1.1158	4.8665	-8.3204
1.1158	4.8466	-8.3485
1.1158	4.8267	-8.3792
1.1158	4.8067	-8.4119

Continued on next page

Table C.2 – continued from previous page

R_g (nm)	d_{COMs} (nm)	Free Energy (kJ/mol)
1.1158	4.7868	-8.4464
1.1158	4.7669	-8.4812
1.1158	4.7469	-8.5162
1.1158	4.727	-8.5496
1.1158	4.7071	-8.5815
1.1158	4.6871	-8.6116
1.1158	4.6672	-8.6395
1.1158	4.6473	-8.6651
1.1158	4.6273	-8.6878
1.1158	4.6074	-8.7082
1.1158	4.5875	-8.7269
1.1158	4.5675	-8.7449
1.1158	4.5476	-8.7634
1.1158	4.5277	-8.7835
1.1158	4.5078	-8.8061
1.1158	4.4878	-8.8329
1.1158	4.4679	-8.8662
1.1158	4.448	-8.9067
1.1158	4.428	-8.956
1.1158	4.4081	-9.0149
1.1158	4.3882	-9.0837
1.1158	4.3682	-9.1623
1.1158	4.3483	-9.2504
1.1158	4.3284	-9.3461
1.1158	4.3084	-9.4487
1.1158	4.2885	-9.556
1.1158	4.2686	-9.666
1.1158	4.2486	-9.7767
1.1158	4.2287	-9.8862
1.1158	4.2088	-9.9933
1.1158	4.1888	-10.096
1.0959	4.1689	-10.194
1.0959	4.149	-10.286
1.0959	4.129	-10.372
1.0959	4.1091	-10.451

Continued on next page

Table C.2 – continued from previous page

R_g (nm)	d_{COMs} (nm)	Free Energy (kJ/mol)
1.0959	4.0892	-10.524
1.0959	4.0693	-10.591
1.0959	4.0493	-10.652
1.0959	4.0294	-10.709
1.0959	4.0095	-10.763
1.0959	3.9895	-10.814
1.0959	3.9696	-10.864
1.0959	3.9497	-10.914
1.0959	3.9297	-10.965
1.0959	3.9098	-11.018
1.0959	3.8899	-11.074
1.0959	3.8699	-11.135
1.0959	3.85	-11.2
1.0959	3.8301	-11.27
1.0959	3.8101	-11.345
1.0959	3.7902	-11.427
1.0959	3.7703	-11.518
1.0959	3.7503	-11.619
1.0959	3.7304	-11.727
1.0959	3.7105	-11.845
1.0959	3.6905	-11.978
1.0959	3.6706	-12.128
1.0959	3.6507	-12.282
1.0959	3.6308	-12.444
1.0959	3.6108	-12.619
1.0959	3.5909	-12.808
1.1158	3.571	-13.015
1.1158	3.551	-13.237
1.1158	3.5311	-13.475
1.1158	3.5112	-13.728
1.1158	3.4912	-13.996
1.1158	3.4713	-14.276
1.1158	3.4514	-14.567
1.1158	3.4314	-14.866
1.1158	3.4115	-15.172

Continued on next page

Table C.2 – continued from previous page

R_g (nm)	d_{COMs} (nm)	Free Energy (kJ/mol)
1.1158	3.3916	-15.481
1.1158	3.3716	-15.79
1.1357	3.3517	-16.099
1.1357	3.3318	-16.404
1.1357	3.3118	-16.702
1.1357	3.2919	-16.991
1.1357	3.272	-17.271
1.1357	3.252	-17.539
1.1357	3.2321	-17.793
1.1357	3.2122	-18.034
1.1357	3.1923	-18.26
1.1357	3.1723	-18.471
1.1357	3.1524	-18.665
1.1357	3.1325	-18.842
1.1357	3.1125	-19.003
1.1357	3.0926	-19.146
1.1357	3.0727	-19.272
1.1357	3.0527	-19.381
1.1556	3.0328	-19.475
1.1556	3.0129	-19.553
1.1556	2.9929	-19.615
1.1556	2.973	-19.662
1.1556	2.9531	-19.695
1.1556	2.9331	-19.713
1.1755	2.9132	-19.721
1.1755	2.8933	-19.728
1.1954	2.8733	-19.746
1.2153	2.8534	-19.802
1.2749	2.8335	-19.888
1.4539	2.8135	-20.189
1.5136	2.7936	-20.691
1.5335	2.7737	-21.233
1.5335	2.7538	-21.789
1.5534	2.7338	-22.348
1.5534	2.7139	-22.903

Continued on next page

Table C.2 – continued from previous page

R_g (nm)	d_{COMs} (nm)	Free Energy (kJ/mol)
1.5534	2.694	-23.449
1.5534	2.674	-23.983
1.5732	2.6541	-24.507
1.5732	2.6342	-25.017
1.5732	2.6142	-25.51
1.5732	2.5943	-25.987
1.5732	2.5744	-26.447
1.5732	2.5544	-26.888
1.5732	2.5345	-27.31
1.5732	2.5146	-27.712
1.5732	2.4946	-28.095
1.5732	2.4747	-28.457
1.5732	2.4548	-28.798
1.5732	2.4348	-29.119
1.5732	2.4149	-29.417
1.5732	2.395	-29.695
1.5732	2.375	-29.95
1.5732	2.3551	-30.183
1.5732	2.3352	-30.394
1.5732	2.3153	-30.582
1.5534	2.2953	-30.749
1.5534	2.2754	-30.892
1.5534	2.2555	-31.013
1.5534	2.2355	-31.11
1.5534	2.2156	-31.184
1.5534	2.1957	-31.235
1.5534	2.1757	-31.263
1.5534	2.1558	-31.267